# THERMOMECHANICAL BEHAVIOUR OF CELLULAR BEAMS

**Dahmane Manal**

Final thesis presented to

**SCHOOL OF TECHNOLOGY AND MANAGEMENT**

**POLYTECHNIC INSTITUTE OF BRAGANÇA**

For the fulfilment of the Master Degree in

**CONSTRUCTION ENGINEERING**

**July. 2017**

# THERMOMECHANICAL BEHAVIOUR OF CELLULAR BEAMS

**Dahmane Manal**

Final thesis submitted to the

**School of Technology and Management**

**Polytechnic Institute of Bragança**

For the fulfilment of the Master Degree in

**CONSTRUCTION ENGINEERING**

Supervisor at IPB:

**Prof Dr. Luis Mesquita**

Supervisor at UHBC:

**Prof Dr. Abdelhak Kada**

**July. 2017**

# ACKNOWLEDGMENTS:

I am very grateful to the supervisors of the thesis:

Dr. Luís Mesquita, coordinator Professor from the Department of Applied Mechanics School of Technology and Management Polytechnic Institute of Bragança, for his endless help, guidance of a great value and the tremendous effort for the achievement of the research project and thesis.

Dr Kada Abdelhak, Faculty of Civil Engineering and Architecture University Hassiba Benbouali of Chlef for his guidance, encouragement and support throughout this thesis and overall ERASMUS period.

My special thanks, to Professors Paulo Piloto, Elza Fonseca for their support and encouragement and to Professors Lamri Belkacem, Dr Benarous Abdellah and Dr Nourredine Benlakehal for their help.

Thanks to all my professors of IPB as well as of UHBC and to the School of Technology and Management of the IPB.

I am grateful to my beloved parents and all my family and friends, especially Ayyoub and Aslan for their moral support, motivation and encouragement during my studies within this master course.

Finally, I would like to deeply acknowledge:

The European Union whose Erasmus ICM plus program and funding has given me the opportunity to participate in this master degree course.

The IPB ERASMUS+ team, namely Professor Luis Pais and Joana Aguiar and their staff who made easy for us to undertake this program at IPB Bragança.

# Resumo

Esta tese apresenta um trabalho de investigação sobre o comportamento de vigas de aço a temperaturas elevadas, usando simulações de elementos finitos com o software ANSYS. São analisadas vigas sólidos e alveolares, considerando a variação transiente da temperatura ao longo do tempo, o comportamento não linear material e geométrico, bem como o efeito das imperfeições geométricas iniciais e das tensões residuais. As análises numéricas térmicas e mecânicas utilizam os modelos do comportamento do material dependente da temperatura, segundo o Eurocódigo 3 parte 1-2.

Os modelos numéricos utilizados no software Ansys, utilizam elementos finitos de casca de 4 nós, para as simulações térmicas (SHELL131) e para as simulações estruturais e termomecânicas (SHELL181). O comportamento ao fogo das vigas sólidas e alveolares é analisado numericamente comparado os resultados da evolução da temperatura com os obtidos experimentalmente por Lamri B. em vigas de aço não protegidas expostas á curva de incêndio padrão ISO834 e adicionalmente segundo o método simplificado do Eurocódigo 3 parte 1-2.

O comportamento termomecânico e os respetivos mecanismos de colapso das vigas foi analisado considerando uma distribuição de temperatura uniforme e uma carga distribuída continuamente crescente, permitindo a determinação da carga de colapso para diferentes valores de temperaturas. É determinada a resistência de várias secções transversais, com diferentes valores dos diâmetros dos furos circulares, da distância entre furos e da largura da alma entre furações (web-post).

A resistência à encurvadura lateral torsional de vigas sólidas e alveolares é igualmente analisada através de simulações numéricas, considerando a influência das imperfeições geométricas iniciais, para diferentes valores de temperatura. Os resultados são comparados com os obtidos pelos métodos simplificados do Eurocódigo 3 parte 1.2. Os resultados das simulações térmicas realizadas no software ansys seguem a tendência obtida com os resultados dos testes experimentais. Os resultados da LTB mostram que a resistência é mais influenciada pelas imperfeições geométricas do que pelas tensões residuais. Adicionalmente, foi verificado que o efeito da temperatura, da secção transversal e das imperfeições geométricas é mais significativo nas vigas alveolares do que no caso das vigas solidas.

*Palavas-chave:* Vigas Alveolares, *Temperaturas elevadas, Simulações numéricas, Encurvadura Lateral Torsional.*

# Abstract

This thesis presents a research work on the behaviour of steel beams at high temperatures, using finite element simulations with ANSYS software. Solid and cellular beams are analysed, considering the transient temperature variation over time, nonlinear material and geometric behaviour, as well as the effect of initial geometric imperfections and residual stresses. The thermal and mechanical numerical analyses consider the material properties temperature variation according to the Eurocode 3 part 1-2.

The numerical models implemented in Ansys software use shell finite elements of 4-nodes for thermal simulations (SHELL131) and for structural and thermomechanical simulations (SHELL181).

The fire behaviour of the solid and cellular beams is numerically analysed comparing the results of the temperature evolution with those obtained experimentally by Lamri B in unprotected steel beams exposed to the standard fire curve ISO834 and additionally according to the simplified method of the Eurocode 3 part 1-2.

The thermomechanical behaviour and the beams collapse mechanisms were analysed considering a uniform temperature distribution and a continuously increasing distributed load in the top flange, allowing the determination of the collapse load for different temperature values. The resistance of several cross-sections, with different values of the holes diameter, the distance between holes and the web-post width is determined.

The lateral torsional buckling resistance of solid and cellular beams is also analysed by numerical simulations, considering the influence of the initial geometric imperfections, for different temperature values. The results are compared with those obtained by the simplified methods of Eurocode 3 part 1-2.

The simulations with ANSYS thermal finite element models have produced good predictions for temperature evolution with small discrepancies acceptable for comparison with tests. The LTB resistance is more influenced by geometric imperfections than the residual stress. The effect of residual stress disappear in height temperature and also effect by the temperature and the length. For cellular beams the effect of temperature, cross section and geometry imperfection is higher than what is obtained in solid beams.

*Keywords:* Cellular Beams, Elevated Temperatures, Numerical Simulations, Lateral Torsional Buckling

# INDEX

# LISTE OF FIGURES

## LIST OF TABLES

# SIMBOLOGY

| | |
|---|---|
| $\theta a$ | steel temperature increase from time *t* to time *t*+ *t* |
| $k_{sh}$ | Correction factor for the shadow effect. see below |
| $A_m$ | surface area of the member per unit length |
| $V$ | volume of the member per unit length |
| $t$ | time |
| $V$ | volume of the member per unit length |
| $\theta_{g.t}$ | ambient gas temperature at time *t* |
| $\theta_{a.t}$ | steel temperature at time *t* |
| $d_p$ | thickness of the fire protection material |
| $c_a$ | temperature dependent specific heat of steel |
| $\rho_a$ | unit mass of steel |
| $\Delta t$ | time interval |
| $\theta_{g.t}$ | increase of ambient gas temperature during the time interval _*t* |
| $c_p$ | temperature independent specific heat of the fire protection material |
| $\rho_p$ | unit mass of the fire protection material |
| h | Height of section. |
| b | Width of section. |
| tw | Thickness of web. |
| $A_v$ | The shear area |
| $A$ | The cross sectional area |
| $\Delta l/l$ | The relative thermal elongation of steel |
| $K_{p.\theta}$. | The reduction factors for the proportional limit |
| $K_{y.\theta}$ | To the effective yield strength |
| $K_{E.\theta}$ | the slope of the linear elastic range |

| | |
|---|---|
| $\alpha_c$ | the coefficient of heat transfer by convection |
| $\dot{h}_{net}$ | design value of the net heat flux per unit area |
| $\dot{h}_{net,c}$ | the convective heat flux |
| $\theta_m$ | the member temperature |
| $h_{net,r}$ | the radiative component |
| $\phi$ | Is the configuration factor |
| $\sigma$ | the Stephan Boltzmann constant |
| $\varepsilon_m$ | the surface emissivity of the member |
| $\varepsilon_f$ | the emissivity of the fire |
| $A_p / V$ | the section factor for protected steel members |
| $\lambda_p$ | the thermal conductivity of the fire protection system |
| $d_p$ | is the thickness of the fire protection material |
| $c_p$ | the temperature independent specific heat of fire protection |
| $\rho_p$ | the unit mass of fire protection material |
| $M_{Ed}$ | The design value of the bending moment |
| $M_{pl,Rd}$ | the plastic moment resistance |
| $\chi_{LT}$ | the reduction factor for lateral-torsional buckling |
| $W_{pl_y}$ | The plastic section modulus about the y-y axis. |
| $f_y$ | the yield stress of steel |
| $\gamma_{M1}$ | the partial safety factor for a material property |
| $\overline{\lambda}_{LT}$ | the non-dimensional slenderness |
| $M_{cr}$ | the elastic critical moment |
| $\alpha_{LT}$ | the imperfection factor |
| $t_f$ | the flange thickness |
| $M_{fi,\theta,Rd}$ | the design moment resistance In fire condition |

| | |
|---|---|
| $k_c$ | Correction factors for the new proposal |
| $V_{pl,Rd}$ | the design plastic shear resistance of a cross section |
| $A_v$ | the shear area |
| tw | The web thickness of the Tee |
| $h_{w.T}$ | The overall depth of the Tee. |
| $A_{v,tT}$ | the shear areas of the Tee |
| $M_{pl,Rd}$ | The plastic bending resistance of a top or bottom Tee section in the absence of axial force |
| $z_{pl}$ | the distance between the plastic neutral axis and the extreme fibre of the steel flange |
| $A_{w,T}$ | the cross sectional area of web of the Tee |
| $A_f$ | the cross sectional area of the flange |
| a0 | Holes diameter |
| w | Web post width |
| w0.wf | Width of begin and end solid part of cellular beam |
| Hf | Final height of cellular beam |
| S | Web post width plus diameter |
| a0/h | hole diameter to the section height ratios |
| w/a0 | Web post to hole diameter ration |
| Hf/h | Final height to initial height ratio |

# CHAPTER.1 INTRODUCTION

## 1.1 Context and motivation

During more than ten years, there has been an increase in the use of cellular beams both in metal structures and in exploring new structural solutions. The use of cellular beams allows a new architectural expression. Structures are lightened and spans increased pulling spaces together. This flexibility goes together with the functionality of allowing technical installations to pass through the openings. The lightweight appearance of cellular beams combined with their high strength never ceases to inspire architects to new structural forms,[1].

**Application fields:**

- roofing

The use of cellular beams roofing elements enables large spans. In the region of 40 metres to be covered as Figure 1 shows. Whether used as independent elements or continuity elements. The competitiveness of the ACB® solution is confirmed both by the retention of the functionalities of lattice beams and by the reduction of on-site interventions for assembly, [1].

Figure 1: Curved roof beams and Sports hall, [1].

Cellular beams offer architects attractive and practical solutions in terms of use of space without screening effect. The diameter of the openings can reach 80 % of the total height of the beam and it is possible to leave only a small distance – required for fabrication between the openings. This configuration of cellular beams enables their transparency and blending into the space enclosed to be accentuated, Which has great appeal for architects, [1].

- decking

Modern constructions increasingly demand the accommodation of technical installations (heating. ventilation. air conditioning. etc.) within the available space enclosed.

The use of cellular beams now provides effective answers to the demands of project owners. This solution allows large uninterrupted spaces over a distance of up to 18 metres and allows various pipes and ducts to be passed through the openings Figure 2, [1].

Figure 2: Distribution of services in a cellular beam system.

**Concept – fabrication:**

The patented method used for the fabrication of cellular beams is based on the exclusive use of hot rolled sections, a double cut-out is made in the web by flame cutting. The two obtained T-sections are shifted and rewelded. Leading to an increase in height as is illustrated in Figure 3, [1].

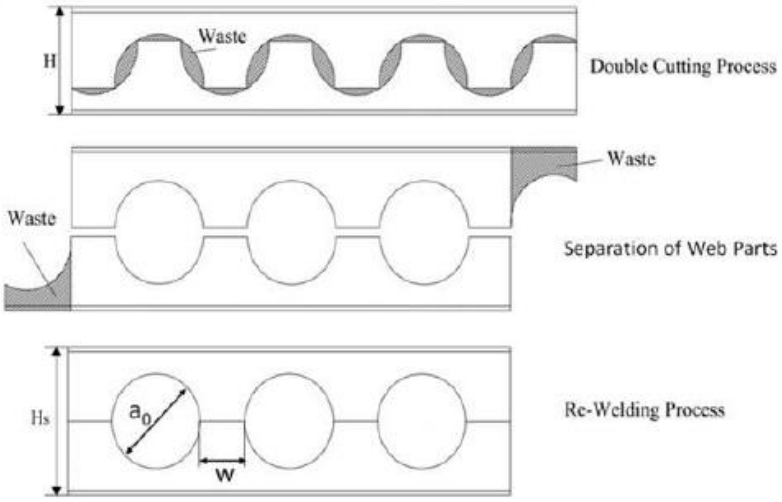


Figure 3: diagram of the fabrication of a cellular beam, [1].

The cutting process is digitally controlled in order to obtain perfect matching of the openings the parallel fabrication of beams reduces the production costs.

Effective failure modes relating to the steel cellular beams that nowadays have become widely used as a part of a building load-bearing structure are identified and discussed in detail. They are presented as those being critical both due to the structural resistance evaluation and due to the stability assessment, [2].

In the first case, the ultimate bending moment resistance of a whole beam in the presence of shear is estimated as well as the resistance of the beam tee section located at mid-length of the web opening. Regarding to the verification of beam stability not only the lateral-torsional buckling is taken into consideration but also the shear buckling of the beam web and even the local instability of a web-post. Finally, The risk of the rupture of a welded joint located in a beam web-post is assessed to check if it is so small that the building user can accept it, [2].

Figure 4: Web-post lateral-torsional buckling, [2].

## 1.2 State of the art

Beams with long span are increasingly used in metal construction to obtain a greater flexibility in the use of the surfaces. These large ranges generally require the use of high-rise sections. Which are added crossings technical equipment and ventilation systems to reduce the overall height of the floors. One of the solutions is performed to provide openings in the web of the beams to allow the passage of technical ducts while maintaining a minimum floor thickness. As represented in Figure 5. This method reduces the floor height and therefore the overall height of building.

Figure 5: Example floor with conduits integration through the openings of cellular beams.

The presence of these openings involves changes in the mechanical behaviour of beams, notably the appearance of local failure modes around openings. These openings in the web have influence on the bending strength of the beam. Many experimental and numerical studies have been conducted on the cellular beams.

In 2001 K.F. Chung et al, presented an investigation of the Vierendeel mechanism in steel beams with circular web openings based on analytical and numerical studies. The current design method is examined in detail with plastic hinges formed at the low moment side (LMS) and the high moment side (HMS) of the web openings separately. A finite element model is then established with both material and geometrical non-linearity so that load redistribution across the web openings may be incorporated. Both analytical and numerical investigations of the load carrying capacities of steel beams with circular web openings are presented in detail, [3].

It should be noted that the current design method is conservative in evaluating the load carrying capacities of steel beams with circular web openings based on the formation of LMS plastic hinges while consideration of the formation of HMS plastic hinges may lead to conservative results, [3].

Secondly, based on the finite element model, improvements to the assessment of load carrying capacities of steel beams with large circular web openings are obtained through incorporation of plastic hinge formation at both the LMS and the HMS of the perforated sections. As modified by load-redistribution across the web opening at large deformation and enhanced strength assessment on the moment capacities of tee sections under co-existing axial and shear forces, [3].

In 2007 Ali Nadjai et al, made an experimental and analytical study of the behaviour of composite floor cellular steel beams in fire conditions conducted at the FireSERT, a total of four specimens comprising two different steel geometries and loading conditions were tested under monotonic loading and at elevated temperatures. The study suggests the following: The two beams failed due to web post buckling and the instability resulted in sudden loss of stiffness and strength in the beams. The experimental data has compared well with the results from the Finite Element Modelling giving confidence that it can be used for further parametric studies, [4].

In 2013 B. Zhao et al, made an experimental and numerical investigation on cellular beams at elevated temperatures. The results show that the analytical design method is conservative with little discrepancy when compared to the numerical model. The results were then compared to those from an analytical design method to check its validity Full-scale fire tests on four specimens are used to analyse the behaviour of composite steel and concrete cellular beams with evenly spaced circular and elongated web holes, the behaviour of the tested beams was simulated using two FEM codes (Cast3M and ANSYS). The beams were not fire protected and they were tested with an ISO fire or a bilinear thermal curve representing the behaviour of a protected beam. The use of cellular beams endowed with aesthetical and mechanical advantages requires a good understanding of their behaviour at both ambient and elevated temperatures. Therefore four fire tests were carried out on unprotected composite cellular beams in order to enlarge the fire test output data available for such beams. Besides an existing analytical method for designing cellular beams at elevated temperatures was evaluated by comparison with the finite element model results This study can be completed by a more extensive approach to estimate the real behaviour of

cellular beams as integral parts of a floor fully or partially exposed to a fire. The tests results have put into evidence that beams with slender web-posts and a symmetrical steel cross-section were prone to fail by web-post buckling, [5].

In 2014 Peijun Wang et al, made an analytical study about buckling behaviours of web-posts in a cellular steel beam at elevated temperatures in a fire. Where studies using the Finite Element Method analysis and available analytical models and they used finite element software ABAQUS to simulate buckling behaviours of the web-post in a CSB; failure temperatures obtained by the analytical models differed greatly to those obtained from the FEM simulation. Among these analytical models. The buckling temperature obtained through the model based on BS5950-1 agreed with the FEM result. A simplified method was proposed to calculate the effective width of the web post. The accuracy of that model integrating the new effective width was validated against the FEM simulations. The obtained buckling temperature of the web-post using the modified strut model agreed well with the FEM simulation result, [6].

There is large deflection behaviour of the restrained castellated steel beam (CSB) in a fire for study that in 2014. Peijun Wang et al, made numerical study to investigate this event using the finite element software ABAQUS. Studied CSBs adopted a newly proposed fillet corner polygonal web opening shape. The capability of the finite element model was validated against verified numerical results on solid web restrained steel beams at elevated temperatures in a fire. The finite element model was verified through available simulation results on restrained steel beams in a fire. The studies parameters of the castellated steel beam included the expansion ratio, the web-opening dimension the web opening shape, the opening arrangement and the axial restraint stiffness ratio to the castellated steel beam for the axial stiffness of a castellated steel beam is smaller than that of the original solid web steel beam the compression force due to restrained thermal elongation is lower than that in the solid web beam, [7].

In 2016. Ali Nadjai et al, made an experimental and analytical study of the behaviour of composite floor with protected and unprotected cellular steel beams in fire conditions conducted at the FireSERT. Beams were protected with intumescent coating having different size and openings shape. All beams were designed for full shear connections between the steel beam and the concrete flange using headed shear studs in order to fail in by web-post

buckling and it may be concluded that: Intumescent coating is the most effective fire protection material for steel cellular beams. The experimental results from the furnace fire tests of protected cellular beams were compared to the results of tested unprotected cellular beams; have demonstrated that the recorded temperatures on the protected steel sections are smaller than the unprotected and the deformation of the protected composite cellular beams is less crucial than the unprotected. The failure mechanism in the three protected composite cellular beams failed with the same manner as the unprotected but with a longer duration time and this is due to the insulation material used. The numerical model is capable to simulate the mechanical behaviour of composite cellular beam sections protected at elevated temperature conditions with a relatively high accuracy, [8].

## 1.3 Thesis structure

The thesis is organised in five chapters. In the following paragraphs, a brief description of the contents of each is presented.

Chapter 1 is an introduction to the research work presented in this thesis, where the objective and motivation is presented; the state of the art is also included.

Chapter 2 presents safety verification of structures according to the Eurocodes, with a definition of the mechanical and thermal properties of materials. The fire curves, steel temperature evolution for unprotected and protected cross section and the safety verification for solid and cellular beams at ambient and elevated temperature.

Chapter 3 presents the steel temperature development of steel beams exposed to fire using a simple calculation method, a summary of experimental test done by Lamri.B and comparison between simple calculation method and experimental results, include thermal analysis using Ansys. The numerical model was calibrated against the experimental test, comparing numerical results with experimental test and simple calculation method from Eurocode.

Chapter 4 presents the thermomechanical numerical analysis for solid and cellular beams including cross section resistance for solid and cellular beams, numerical lateral torsional buckling analysis for solid beam and cellular beams is also included.

Chapter 5 presents the main conclusions and proposals for future work.

# CHAPTER.2 SAFETY VERIFICATION OF STRUCTURES ACCORDINGLY TO THE EUROCODES

## 2.1 Introduction

The fire design of steel and composite structures must be done in accordance with the Eurocodes. It introduces the basis of design for fire situations, which are considered as accidental situations and the criteria that need to be met. The direct action of a fire is essentially the heat flux transferred to the members. The basis of determining heat flux of a nominal temperature-time curve for a predetermined duration.

The strength and stiffness of steel is modified at elevated temperatures. Extensive research has led to standardized relationships that can be used to determine structural behaviour in fire. The variation of properties with temperature is discussed and graphical presentations are given.

## 2.2 Fire safety verification domains

According to Eurocode 3, the fire resistance of steel building structures can be assessed by means of the following three "domains"

- In terms of time, duration obtained from step by step fire resistance calculation.
- In terms of fire resistance capacity at required resistance time.
- In terms of critical temperature in comparison with the design heating of steel members at required time.

Figure 6 refer to the case of a nominal fire in which the fire temperature. $\theta_{\text{fire}}$ is continuously increasing. The temperatures in the structure. $\theta s_{\text{tructure}}$, will therefore also be a continuously increasing as a function of time and although this will not be demonstrated theoretically it will be assumed that this induces a continuously decreasing load bearing capacity, $R_{\text{fi.d.t}}$, [9].

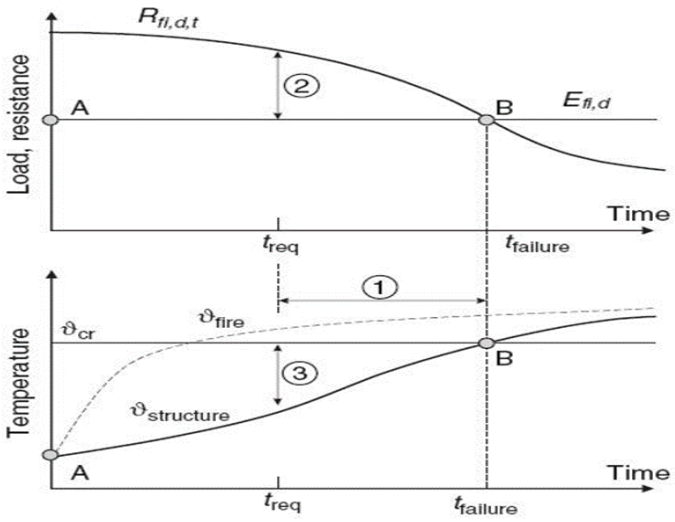


Figure 6: Load. time or temperature domain for a nominal fire, [9].

2.2.1 Safety verification in time domain

It has to be verified that the time of failure $t._{\text{failure}}$ is higher than the required fire resistance time $t$ req. This is expressed by the Equation (1)

$$t_{failure} \geq t_{req} \tag{1}$$

2.2.2 Safety verification in load domain

At the required time in the fire $t_{\text{req}}$ it is verified that the resistance of the structure $R_{fi.d.t}$ is still higher than the effect of action $E_{fi.d}$. This is expressed by the equation (2)

$$R_{,fi,d,t} \geq \mathrm{E}_{\mathrm{fi,d}} \text{ at } \mathrm{t} = \mathrm{t}_{\mathrm{rq}} \tag{2}$$

This verification is proposed as the standard method in Eurocode 3, shown that, in case of a fire with no decreasing phase. The fact that Equation (2) is satisfied guarantees that Equation (1) is also satisfied, [9].

2.2.3 Safety verification in temperature domain

At the required fire resistance time ($t_{\text{req}}$) it has to be verified that the temperature of the structure $\theta_{\text{structure}}$ is still lower than the critical temperature $\theta_{cr}$ (the temperature that leads to failure). This is expressed by equation (3), [9].

$$\theta \geq \theta_{cr} \text{ at } t = t_{rq} \quad (3)$$

This verification is a particular case of the verification in the load domain, only possible when the stability of the structure is depending on a single temperature. Which is the case in steel elements under uniform temperature distribution. It can also happen for natural fires that Equation (3) is satisfied whereas Equation (1) is not.

The verification in the load domain has indeed several advantages, which is 1- It is easy to use; because the verification is at a given time; the steel temperature and hence, the material properties are known and can be used for the evaluation of the load bearing capacity. 2- It is applicable for any type of effect of actions whereas as will be explained in Section verification in the temperature domain is possible only in a limited number of cases. 3- It produces a safety factor that is similar to the one that engineers and designers have been using for years at room temperature namely the ratio between the applied load and the failure load. On the other hand, Verification in the temperature domain yields a safety factor in degrees centigrade that does not provide much in term of practical consequences, [9].

A verification in the time domain may even be more confusing because with the tendency of standard fire curves to level off at nearly constant temperatures after a certain period of time they can yield the false impression of a very high level of safety because the calculated time of failure is significantly longer than the required fire resistance time. Simply because the temperature of the structure changes very slowly, where as a small variation in the applied load or in the heating regime would decrease the fire resistance time very dramatically close to the required resistance time, [9].

## 2.3 Steel material properties variation with temperature

All materials lose strength at elevated temperature and in order to calculate the variation of member resistance with temperature, the strength reduction of the material must be known. It important to know how quickly a structure member at which it will no longer be able to support the loads to which it is exposed in fire condition, this will require a heat transfer analysis for which the thermal and mechanical properties must be known, [10].

### 2.3.1 Thermal properties:

#### 2.3.1.1 Specific heat:

The Specific heat of steel represents the amount of energy that is necessary to raise the unit mass of steel temperature by 1 [°C]. It is also the measure of the materials ability to absorb heat. The specific heat of steel $C_a$ defined in accordance to Eurocode EN1993-1-2, [11], as the following:

- for : $20°C \le \theta_a \le 600°C$

$$C_a = 425 + 7{,}73\times10^{-1}\theta_a - 1{,}69\times10^{-3}\theta_a{}^2 + 2{,}22\times10^{-6}\theta_a{}^3 [J/kg\cdot K] \quad (4)$$

- for $600°C \le \theta_a \le 735°C$

$$C_a = 666 + \frac{13002}{738-\theta_a}[J/kg\cdot K] \quad (5)$$

- for: $735°C \le \theta_a \le 900°C$

$$C_a = 545 + \frac{17820}{\theta_a - 731}[J/kg\cdot K] \quad (6)$$

- for $735°C \le \theta_a \le 900°C$:

$$C_a = 650[J/kg\cdot K] \quad (7)$$

Where: $\theta_a$ is the steel temperature[°C ].

The variation of the specific heat with temperature is illustrated in Figure 7.

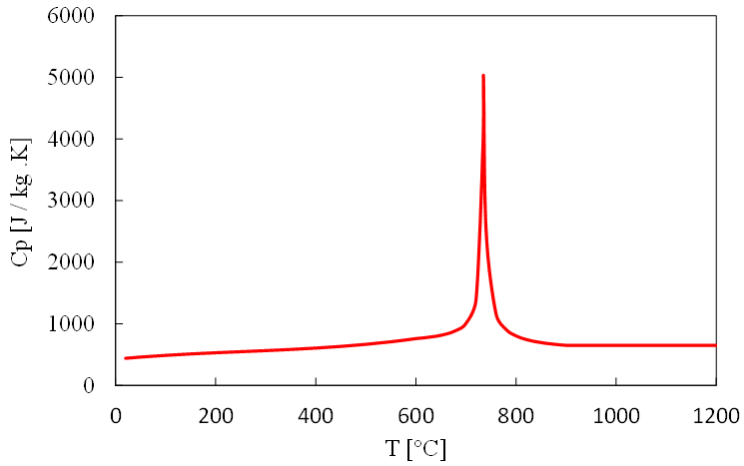


Figure 7: Specific heat of carbon steel as a function of the temperature.

2.3.1.2 Thermal conductivity:

Thermal conductivity is the coefficient with dictates the rate that heat arriving at the steel surface is conducted through the metal. According to Eurocode EN1993-1-2 [11], the variation of thermal conductivity with temperature is represented in Figure 8. The thermal conductivity of steel should be determined from the following:

- for $20[°C] \le \theta < 800[°C]$

$$\lambda_a = 54 - 3{,}33 \times 10^{-2} \theta_a [w/mk] \tag{8}$$

- For $800[°C] \le \theta < 1200[°C]$

$$\lambda_a = 27{,}3[w/mk] \tag{9}$$

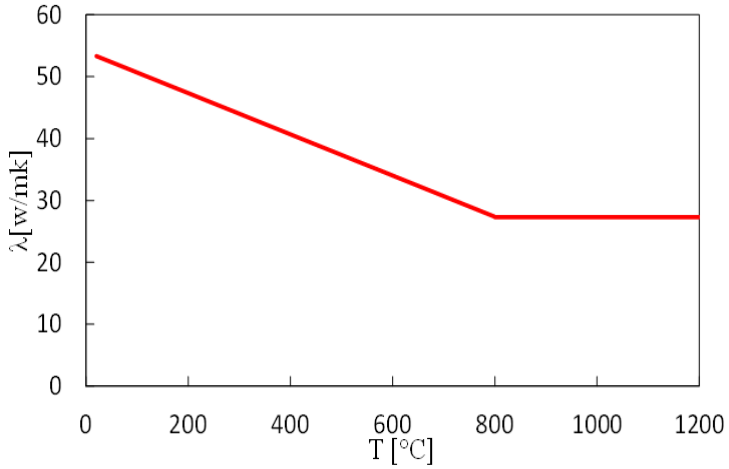


Figure 8: Thermal conductivity at elevated temperature.

2.3.1.3 The density of steel:

The density of steel is constant $\rho = 7850\,[\mathrm{kg/m^3}]$, even when the temperature is modified.

2.3.1.4 Thermal elongation:

When an object is heated or cooled, its length changes by an amount proportional to the original length and the change in temperature. The relative thermal elongation of steel *Δl/l* should be determined from the following:

- for $20°C \le \theta_a < 750°C$

$$\Delta l / l = 1{,}2\times10^{-5}\theta_a + 0{,}4\times10^{-8}\theta_a{}^2 - 2{,}416\times10^{-4} \quad (10)$$

- for $750°C \le \theta_a < 860°C$

$$\Delta l / l = 1{,}1\times10^{-2} \quad (11)$$

- for $860°C \le \theta_a < 1200°C$:

$$\Delta l / l = 2\times10^{-5}\theta_a - 6{,}2\times10^{-3} \quad (12)$$

Where $l$ is the length at 20[℃], $\Delta l$ represent the temperature-induced elongation. With $\theta_a$ being the steel temperature℃. Figure 9 presents Relative thermal elongation of carbon steel as a function of the temperature.

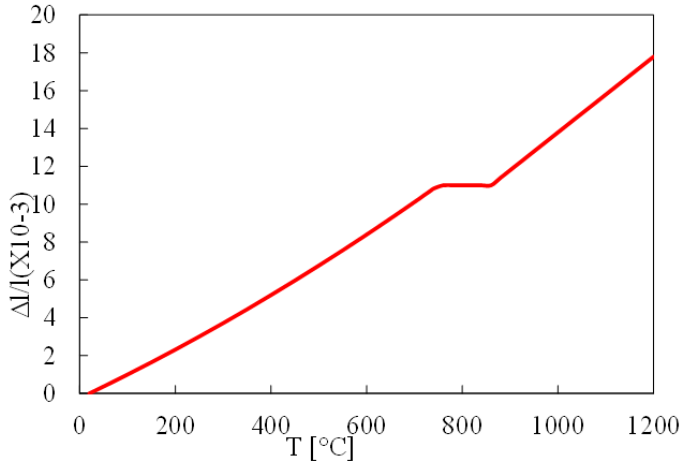


Figure 9: Relative thermal elongation of carbon steel as a function of the temperature.

2.3.2 Mechanical properties of steel under high temperatures:

To take into account the effect of high temperatures on the mechanical properties of the steel reduction factors are proposed. According to EN 1993-1-2,[11] the reduction factors for the proportional limit $K_{p.\theta}$, to the effective yield strength $K_{y.\theta}$and to the slope of the linear elastic range $K_{E.\theta}$ are provided in Table 1 and represented in Figure 10. The stress-strain relationship for steel at elevated temperatures is represented in Table 1 and illustrate in Figure 10, Figure 12 and Figure 13, present Stress-strain relationship for S235 and S355 carbon steel at elevated temperatures respectively.

Table 1: Reduction factors for the stress-strain relationship of carbon steel at elevated temperatures.

| Steel temperature $\theta_a$ | Reduction factors at temperature $\theta_a$ relative to the value of $f_y$ or $E_a$ at 20 °C | | |
|---|---|---|---|
| | Reduction factor (relative to $f_y$) for effective yield strength | Reduction factor (relative to $f_p$) for proportional limit | Reduction factor (relative to $E_a$) for the slop of the linear elastic range |
| | $K_{y.\theta} = f_{y.\theta}/f_y$ | $K_{p.\theta} = f_{p.\theta}/f_p$ | $K_{E.\theta} = E_{a.\theta}/E_a$ |
| 20 °C | 1 | 1 | 1 |
| 100 °C | 1 | 1 | 1 |
| 200 °C | 1 | 0.807 | 0.9 |
| 300 °C | 1 | 0.613 | 0.8 |
| 400 °C | 1 | 0.42 | 0.7 |
| 500 °C | 0.78 | 0.36 | 0.6 |
| 600 °C | 0.47 | 0.18 | 0.31 |
| 700 °C | 0.23 | 0.075 | 0.13 |
| 800 °C | 0.11 | 0.05 | 0.09 |
| 900 °C | 0.06 | 0.0375 | 0.0675 |
| 1000 °C | 0.04 | 0.025 | 0.045 |
| 1100 °C | 0.02 | 0.0125 | 0.0225 |
| 1200 °C | 0 | 0 | 0 |

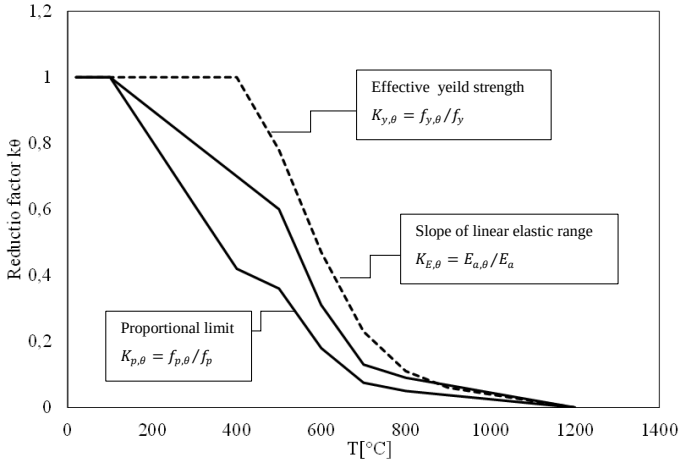


Figure 10: Reduction factors for the stress-strain relationship of carbon steel at elevated temperatures.

Table 2: Stress-strain relationship for carbon steel at elevated Temperatures.

| Strain range | stress | Tangent modulus |
|---|---|---|
| $\varepsilon \le \varepsilon_{P,\theta}$ | $\varepsilon E_{a,\theta}$ | $E_{a,\theta}$ |
| $\varepsilon_{P,\theta} < \varepsilon < \varepsilon_{y,\theta}$ | $f_{p,\theta} - c + (b/a)[a^2 - (\varepsilon_{y,\theta} - \varepsilon)^2]^{0,5}$ | $\frac{b(\varepsilon_{y,\theta} - \varepsilon)}{a[a^2 - (\varepsilon_{y,\theta} - \varepsilon)^2]^{0,5}}$ |
| $\varepsilon_{y,\theta} \le \varepsilon \le \varepsilon_{t,\theta}$ | $f_{y,\theta}$ | 0 |
| $\varepsilon_{t,\theta} < \varepsilon < \varepsilon_{u,\theta}$ | $f_{y,\theta}[1-(\varepsilon-\varepsilon_{t,\theta})/(\varepsilon_{u,\theta}-\varepsilon_{t,\theta})]$ | - |
| $\varepsilon = \varepsilon_{u,\theta}$ | 0.00 | - |
| Parameters | $\varepsilon_{p,\theta} = f_{p,\theta}/E_{a,\theta}$ $\varepsilon_{y,\theta}$ =0.02 $\varepsilon_{t,\theta} = 0{,}15$ $\varepsilon_{u,\theta} = 0{,}20$ | |
| Function | $a^2 = (\varepsilon_{y,\theta} - \varepsilon_{p,\theta})(\varepsilon_{y,\theta} - \varepsilon_{p,\theta} + c/E_{a,\theta}$ $a^2 = c(\varepsilon_{y,\theta} - \varepsilon_{p,\theta})E_{a,\theta} + c^2$ $c = \frac{(f_{y,\theta} + f_{p,\theta})}{(\varepsilon_{y,\theta} - \varepsilon_{p,\theta})E_{a,\theta} - 2(f_{y,\theta} + f_{p,\theta})}$ | |

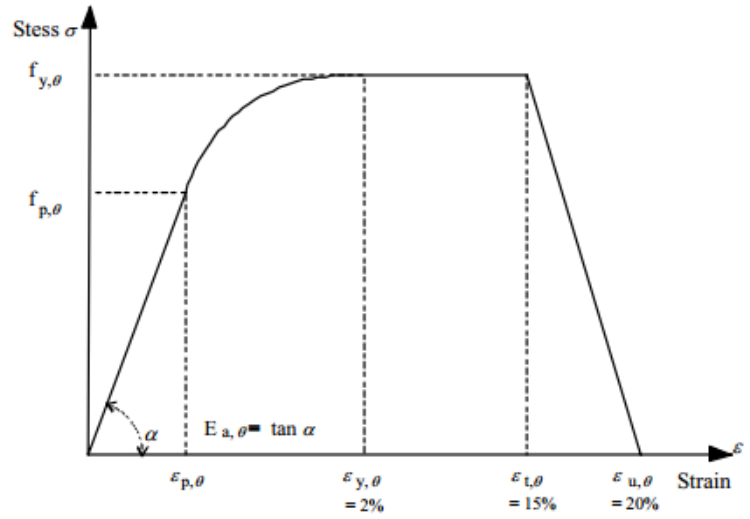


Figure 11: Stress-strain relationship for carbon steel at elevated temperatures.

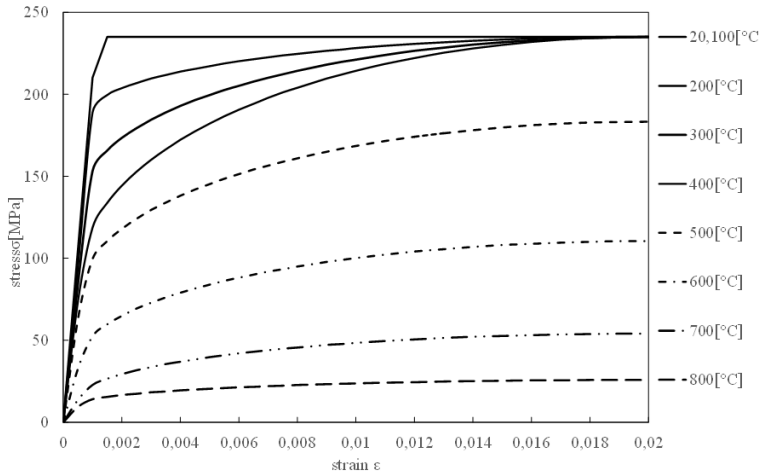


Figure 12: Stress-strain relationship for S235 carbon steel at elevated temperatures.

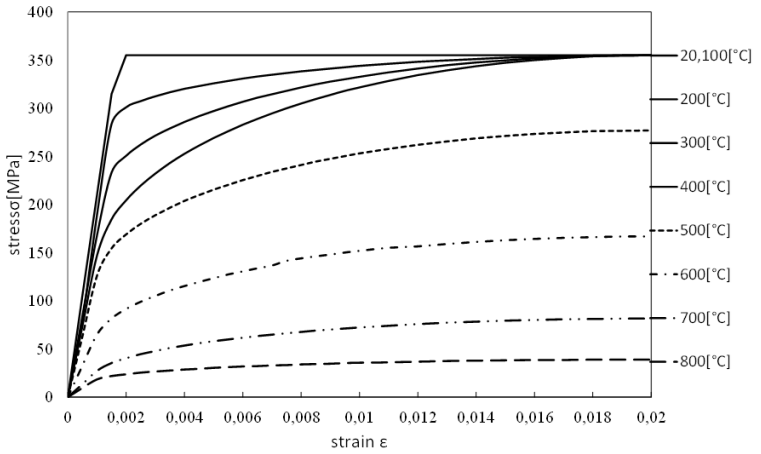


Figure 13: Stress-strain relationship for S355 carbon steel at elevated temperatures.

## 2.4 Nominal fire curves:

A nominal temperature-time curve does not represent the temperature of a real fire. Although they do not represent real fires, they were established from experience on real fires and are the most frequently used, fire analysis design is taking into account the relevant temperature-time curves. Eurocode 1 (EN 1991-1-2) [12], introduces three different nominal temperature-time curves.

Each of these curves is used for special types of fires. The most commonly used is the standard or ISO fire curve. The other are external fire curve and the hydrocarbon fire curve.

### 2.4.1 Standard fire curve ISO 834:

This curve is often referred to as cellulosic heating curve. Although it does not represent an actual fire, it is used as test method for determining the fire resistance of various elements of construction when subjected to standard fire exposure conditions, [12]. The standard temperature-time curve is given according to next expression.

$$\theta_g = 20 + 345\log(8t + 1)\ [°C] \tag{13}$$

Where $\theta_g$ is the gas temperature in the fire compartment [°C] and t is the time [min]. The coefficient of heat transfer by convection is equal to $\alpha_c = 25 \mathrm{W/m^2K}$ . Figure 14, presents standard fire ISO834 curve.

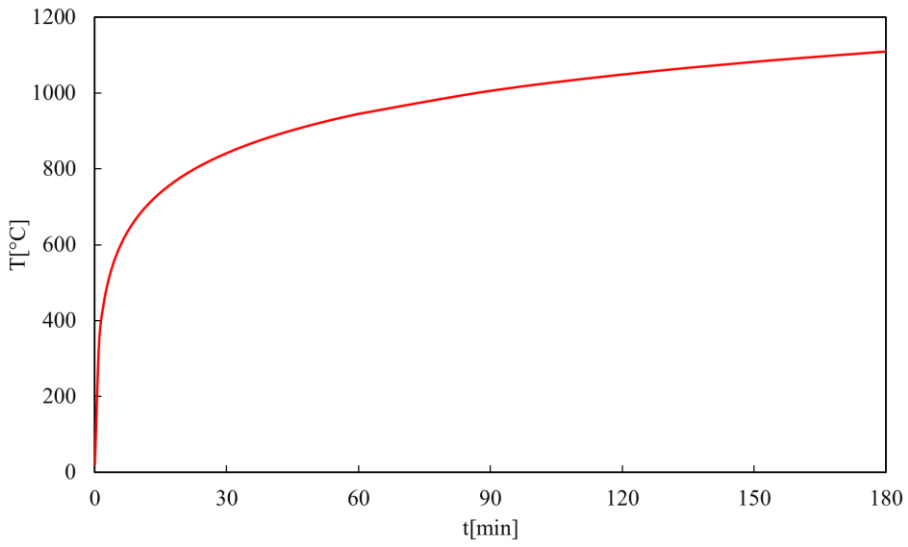


Figure 14 : Standard fire curve ISO834.

2.4.2 External fire curve:

The external fire curve is intended for the outside of separating external walls which are exposed to the external plume of a fire coming either from the inside of the respective fire compartment from a compartment situated below or adjacent to the respective external wall. This curve is not to be used for the design of external steel structures for which a specific model exists, [12]. The external fire curve is given by:

$$\theta_g = 20 + 600(1 - 0.687e^{-0.32t} - 0.313e^{-0.38t}) \text{ [°C]} \quad (14)$$

2.4.3 Curve of hydrocarbons:

The hydrocarbon is a nominal temperature-time curve used in case where storage of hydrocarbon materials makes fires extremely severe, [12]. The hydrocarbon temperature-time curve is given by:

$$\theta_g = 20 + 1080 * (1 - 0.325e^{-0.167t} - 0.675e^{-2.5t}) \text{ [°C]} \quad (15)$$

Where $\theta_g$ is the gas temperature in the fire compartment [°C] and t is the time [min]. The coefficient of heat transfer by convection is equal to $\alpha_c = 50[\text{W/m}^2\text{K}]$.

## 2.5 Steel temperature development

2.5.1 Unprotected internal steelwork

For an equivalent uniform temperature distribution in the cross-section. The increase of temperature Δθa.t in an unprotected steel member during a time interval Δt should be determined from equation of EC3-1-2,[11] given by:

$$\Delta\theta_{a,t} = k_{sh} \frac{A_m / V}{c_a \rho_a} \dot{h}_{net} \Delta t \quad (16)$$

where: $\text{A}_\text{m} / \text{V}$ is the section factor for unprotected steel members [1/m].with $A_m$ is the surface area of the member per unit length [$\text{m}^2$/m] and $V$ is the volume of the member per unit length [$\text{m}^3$/m]; $c_a$ represent is the specific heat of steel and varies with the steel temperature $\theta_a$ .and $\rho_a$ is unit mass of steel = 7850 [$\text{kg/m}^2$]. $\Delta t$ Represent the time interval [s]. This is limited to a maximum of 5 second. $k_{sh}$ is the correction factor for the shadow effect according to equation bellow:

For I sections under nominal fire conditions;

$$k_{sh} = 0.9[A_m / V]_b / [A_m / V] \tag{17}$$

For all other scenarios

$$k_{sh} = [A_m / V]_b / [A_m / V] \tag{18}$$

Where $\dot{h}_{net}$ is the design value of the net heat flux per unit area in accordance with equation of EC1-1-2, [12] given by:

$$\dot{h}_{net} = \dot{h}_{net,C} + \dot{h}_{net,r} \tag{19}$$

Where $\dot{h}_{net,c}$ is the convective heat flux in according with EC1-1-2, defined by:

$$\dot{h}_{ne,c} = \alpha_c \left(\theta_g - \theta_m\right) \tag{20}$$

With $\alpha_c$ is the coefficient of heat transfer by convection and should be taken as 25 [W/m$^2$K] for the standard and external fire curves, $\theta_m$ represent the member temperature in this case equal to $\theta_a$ the steel temperature and $\theta_g$ the gas temperature in the compartment in [°C] and t represents the time in minutes.

Where $h_{net,r}$ is in according with EC1-1-2 given by equation:

$$h_{net,r} = \phi \varepsilon_m \varepsilon_f \sigma[(\theta_r + 273)^4 - (\theta_m + 273)^4] \tag{21}$$

$\Theta_r$ Is the effective radiative temperature of the environment in this case $\theta_r = \theta_g$ the gas temperature, $\phi$ is the view factor for which a recommended value is 1.0 where $\sigma$ is the Stephan Boltzmann constant equal to 5.67x10$^8$ [W/m$^2$K$^4$] and $\varepsilon_m$ represent the surface emissivity of the member for which a recommended value is 0.7 and $\varepsilon_f$ is the emissivity of the fire for which a recommended value is 1.

The critical time is reached when θa.t = θa.cr .The critical temperature θa.cr at time t for a member is determined for any degree of utilization μ0 and evaluated using analytical approach from EN 1993-1-2, [11].

$$\theta_{a,cr} = 39.19 \ln\left[\frac{1}{0.9674\mu_0^{3.833}} - 1\right] + 482(^\circ C) \qquad (22)$$

The degree of utilization $\mu_0$ is the design loading in fire as a proportion of the design resistance at ambient temperature (or at time t=0) but using the material partial safety factors which apply in fire design rather than in normal strength design.

2.5.2 Internal steelwork with fire protection

For an equivalent uniform temperature distribution in the cross-section the increase of temperature, $\Delta\theta_a$, in a protected steel member during a time interval Δt should be determined according with EC3-1-2 given by equation (23):

$$\Delta\theta_{a,t} = \frac{\lambda_p A_p / V}{d_p c_a \rho_a} \frac{(\theta_{g,t} - \theta_{a,t})}{(1+\phi/3)} \Delta t - (e^{\phi/10} - 1)\Delta\theta_{g,t} \qquad (23)$$

$$\text{With } \phi = \frac{c_a \rho_p}{c_a \rho_a} d_p A_p / V$$

Where $A_p / V$ the section factor is for protected steel members [1/m] ,$\lambda_p$ represents the thermal conductivity of the fire protection system, $d_p$ is the thickness of the fire protection material, $c_p$ is the temperature independent specific heat of fire protection and $\rho_p$ is the unit mass of fire protection material.

## 2.6 Safety verification of solid and cellular beams

2.6.1 Safety verification at ambient temperature:

**i. Bending moment resistance:**

The design value of the bending moment $M_{Ed}$ at each cross-section should satisfy:

$$\frac{M_{Ed}}{M_{Rd}} \leq 1{,}0 \qquad (24)$$

Where $M_{Rd}$ is the design resistance for bending about one principal axis which is equal to the plastic moment resistance $M_{pl,Rd}$. For cross section class 1and 2 and according (clause 6.2.5 of EC3-1-1), [13] is determined as follow:

$$M_{Rd} = M_{pl,Rd} = \frac{W_{pl} f_y}{\gamma_{M0}} \tag{25}$$

**ii. Lateral torsional buckling resistance:**

At ambient temperature (20[°C]) lateral torsional buckling resistance. $M_{b\ Rd}$ of a laterally unrestrained steel beam with Class 1 and 2 cross-sections is determined. according to (clause 6.3.2 of EC3-1-1), [13] by the following expression.

$$M_{b,Rd} = \chi_{LT} W_{pl_y} \frac{f_y}{\gamma_{M1}} \tag{26}$$

Where $\chi_{LT}$ is the reduction factor for lateral-torsional buckling. $W_{pl_y}$ Is the plastic section modulus about the y-y axis. $f_y$ Is the yield stress of steel. $\gamma_{M1}$ Is the partial safety factor for a material property, also taking into account model uncertainties and dimensional variations, $\gamma_{M1}$ =1.0 is used in this study.

The reduction factor for lateral-torsional buckling $\chi_{LT}$ can be determined by using the two methods. In this study, the General Method was used $\chi_{LT}$. Is determined as follows:

$$\chi_{LT} = \frac{1}{\phi_{LT} + \sqrt{\phi_{LT}^{\ 2} - \overline{\lambda}_{LT}^{\ 2}}} \tag{27}$$

Where

$$\overline{\lambda}_{LT} = \sqrt{\frac{W_y f_y}{M_{cr}}} \tag{28}$$

$$\phi_{LT} = 0.5\left[1 + \alpha_{LT}(\overline{\lambda}_{LT} - 0.2) + \overline{\lambda}_{LT}^{\ 2}\right] \tag{29}$$

Where $\overline{\lambda}_{LT}$ is the non-dimensional slenderness for LTB. $M_{cr}$ Is the elastic critical moment for lateral torsional buckling. As it is mentioned in expression (32) $\alpha_{LT}$ is the imperfection factor given in Table 3. The imperfection factor defined according to Annex N EC3-1.1, [13] according the buckling curves given in Table 4.

Where h denotes the height and b denotes the width of the cross section.

Table 3: Imperfection factors, [13].

| Buckling curve | a | b | c | d |
|---|---|---|---|---|
| Imperfection factor $\alpha_{LT}$ | 0.21 | 0.34 | 0.49 | 0.76 |

Table 4: Buckling curves, [13].

| Cross-section | limits | Buckling curve |
|---|---|---|
| | | General case |
| Rolled I-sections | h/b≤ 2 | a |
| | h/b> 2 | b |
| Welded I-sections | h/b≤2 | c |
| | h/b>2 | d |
| Other cross-sections | - | d |

**Elastic critical moment for lateral torsional buckling:**

Method for doubly symmetric sections:

The method given hereafter only applies to uniform straight members for which the cross section is symmetric about the bending plane. The conditions of restraint at each end are at least:

- restrained against lateral movement
- restrained against rotation about the longitudinal axis

The elastic critical moment may be calculated from the following formula derived from the buckling theory

$$M_{cr} = C_1 \frac{\pi^2 EI_z}{(KL)^2} \left\{ \sqrt{\left(\frac{k}{k_w}\right)^2 \frac{I_w}{I_z} + \frac{(kL)^2 GI_t}{\pi^2 EI_z} + (C_2 z_g)^2} - C_2 z_g \right\} \qquad (30)$$

Where

E is the Young modulus (E=210000 N/mm²) and G represent the shear modulus (G= 80770 N/mm²). With $I_z$ is the second moment of area about the week axis.

$I_t$ is the torsion constant. $I_w$ represents the-warping constant. L the beam length between points that have lateral restraint and k and $k_w$ are effective length factors $z_g$ is the distance between the point of load application and the shear centre

Note: For doubly symmetric sections. The shear centre coincides with the centroid. C1 and C2 are coefficients depending on the loading and end restraint conditions as it shown in the Table 5.

Table 5: coefficient depending on the loading and end restraint In the common case.

| Loading and support conditions | Diagram of moments | $k_z$ | $C_1$ | $C_2$ | $C_3$ |
|---|---|---|---|---|---|
| 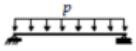 |  | 1.0<br>0.5 | 1.12<br>0.97 | 0.45<br>0.36 | 0.525<br>0.478 |
| 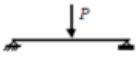 |  | 1.0<br>0.5 | 1.35<br>1.05 | 0.59<br>0.48 | 0.411<br>0.338 |
| 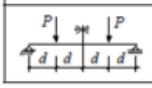 |  | 1.0<br>0.5 | 1.04<br>0.95 | 0.42<br>0.31 | 0.562<br>0.539 |

In the common case of normal support conditions at the ends (fork supports). k and kw are taken equal to 1.

$$M_{cr} = C_1 \frac{\pi^2 EI_z}{(KL)^2} \left\{ \sqrt{\frac{I_w}{I_z} + \frac{(kL)^2 GI_t}{\pi^2 EI_z} + (C_2 z_g)^2} - C_2 z_g \right\} \tag{31}$$

When the bending moment diagram is linear along a segment of a member delimited by lateral restraints. Alternatively, when the transverse load is applied in the shear centre. C2 zg = 0 and C1=1.12. The latter expression should be simplified as follows:

$$M_{cr} = C_1 \frac{\pi^2 EI_z}{(KL)^2} \left\{ \sqrt{\frac{I_w}{I_z} + \frac{(kL)^2 GI_t}{\pi^2 EI_z}} \right\} \tag{32}$$

For doubly symmetric I-profiles. The warping constant Iw may be calculated as follows:

$$I_w = \frac{I_z (h - t_f)^2}{4} \tag{33}$$

Where h is the total depth of the cross-section and $t_f$ is the flange thickness.

### iii. Shear resistance of perforated steel section

The shear resistance should be established from the shear area of the perforated steel section. According to EN 1993-1-1, [13] the design plastic shear resistance of a cross section is given as:

$$V_{pl,Rd} = \frac{A_v f_y / \sqrt{3}}{\gamma_{M0}} \tag{34}$$

Where $A_v$ is the shear area.

For an unperforated I-section beam, the shear area corresponds to the area of the web. However, the perforated cross section is effectively two Tee sections. for which gives an

effective shear area according to SCI (The Steel Construction Institute) [14] of a rolled section Tee as:

$$A_v = \left(A - b_f t_f + (2r + t_w) \times 0.5 t_f\right) \tag{35}$$

Moreover, for a welded Tee section as:

$$A_v = t_w (h_{w,T} \_ 0.5 t_f) \tag{36}$$

Where

A is the cross-sectional area and bf is the overall width of the Tee. tw is the web thickness of the tee, with tf is the flange thickness of the Tee, r is the root radius of the Tee, $h_{w.T}$ is the overall depth of the Tee. Figure 15 present main dimension of tee section.

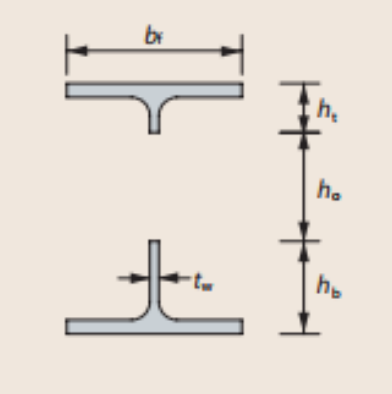


Figure 15: Main dimension of cellular beam cross section, [14].

The plastic shear resistance of the perforated section is thus:

$$V_{pl,Rd} = \frac{(A_{v,tT} + A_{v,bT}) f_y / \sqrt{3}}{\gamma_{M0}} \tag{37}$$

Where $A_{v,tT}$ and $A_{v,bT}$ are the shear areas of the two Tees.

**iv. Plastic bending resistance of Tees**

The plastic bending resistance of a top or bottom Tee section in the absence of axial force (and in the absence of high shear) is given by the following expression, assuming that the plastic neutral axis is in the flange of the Tee:

$$M_{pl,Rd} = \frac{A_{w,T} f_y}{\gamma_{M0}} \left(0.5 h_{w,T} + t_f - z_{pl}\right) + \frac{A_f f_y}{\gamma_{M0}} \left(0.5 h_f - z_{pl} + z_{pl}^{\ 2} / t_f\right) \tag{38}$$

Where $z_{pl}$ is the distance between the plastic neutral axis and the extreme fibre of the steel flange $= (A_f + A_{w,T})/(2 b_f)$ $A_{w,T}$ is the cross sectional area of web of the Tee

$(h_{w,T} \times t_w)$ then $A_f$ is the cross sectional area of the flange with $b_f$ is the breadth of the flange and $h_{w,T}$ is the depth of web of Tee $t_f$ is the flange thickness, [14].

To determine the plastic bending resistance at the centreline of the opening according to SCI clause 3.2.2 [14].The plastic bending resistance is then given by:

$$M_{pl,Rd} = N_{bT,Rd} * h_{eff} \tag{39}$$

$N_{bT,Rd}$ is the tensile resistance of the bottom Tee is given by:

$$N_{bT,Rd} = \frac{A_T * fy}{\gamma_{M0}} \tag{40}$$

Where $h_{eff}$ is the effective depth of the beam between the centroids of the tees.

$$h_{eff} = h - 2 * Zc \tag{41}$$

Where, h denote total height of cross section and $Zc$ the distance from the centroid of the tee to the extreme fibre of the flange given by:

$$Zc = \frac{0.5tf * A_f + (tf + 0.5 * h_{w,T}) * A_{w,T}}{A_f + A_{w,T}} \tag{42}$$

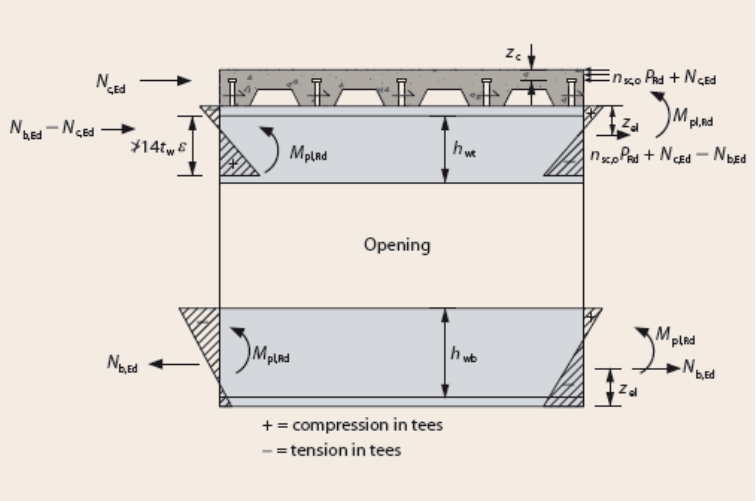


Figure 16: properties of perforated beam, [14].

2.6.2 Safety verification at elevated temperature:

**i. Bending moment resistance:**

In fire, condition the design moment resistance $M_{fi.\theta.Rd}$ of a Class 1 or Class 2 cross-section with a uniform temperature $\theta_a$ According to EN3 1993-1-2, [11] should be determined by:

$$M_{fi,\theta,Rd} = k_{y,\theta}[\gamma_{M,0} / \gamma_{M,fi}]M_{R,d} \tag{43}$$

Where $M_{R,d}$ is the plastic moment resistance of the gross cross-section at elevated temperature $M_{pl.Rd}$ for normal temperature design according to EN 1993-1-1, [13]. $k_{y,\theta}$ is the reduction factor for the yield strength of steel at the steel temperature θa.

**ii. Lateral torsional buckling resistance:**

At elevated temperature the design buckling resistance moment of a laterally unrestrained beam with a class 1, 2 or 3 cross-section type According to EN 1993-1-2, [11] is obtained as follows:

$$M_{b,fi,t,Rd} = \chi_{LT,fi} W_y k_{y,\theta,com} f_y \frac{1}{\gamma_{M,fi}} \tag{44}$$

Where $W_y$ is the appropriate section modulus ($W_y$ =$W_{pl.y}$ the plastic section modulus in y-axis for class 1 or 2 cross sections or $W_y$ =$W_{el.y}$. the elastic section modulus in y-axis for class 3 cross-sections). $k_{y\theta,com}$ denotes the reduction factor for the yield strength of steel at the maximum temperature in the compression flange $\theta_{a,com}$ reached at time t and $\chi_{LT,fi}$ is the reduction factor given by the following equations:

$$\chi_{LT,fi} = \frac{1}{\phi_{LT,\theta,com} + \sqrt{\left[\phi_{LT,\theta,com}\right]^2 - \left[\bar{\lambda}_{LT,\theta,com}\right]^2}} \tag{45}$$

With:

$$\phi_{LT,\theta,com} = \frac{1}{2}\left[1 + \alpha\bar{\lambda}_{LT,\theta,com} + \left(\bar{\lambda}_{LT,\theta,com}\right)^2\right] \tag{46}$$

The non-dimensional slenderness $\bar{\lambda}_{LT,\theta,com}$ is given by:

$$\bar{\lambda}_{LT,\theta,com} = \bar{\lambda}_{LT}\sqrt{\frac{k_{y,\theta}}{k_{E,\theta}}} \tag{47}$$

Where $k_{E,\theta}$ is the reduction factor for the slope of the linear elastic range at the steel temperature $\theta_a$, and $\overline{\lambda}_{LT}$ is the non-dimensional slenderness for lateral–torsional buckling at ambient temperature given by:

$$\overline{\lambda}_{LT} = \sqrt{\frac{W_y f_y}{M_{cr}}} \tag{48}$$

Where $M_{cr}$ is the elastic critical moment for lateral–torsional buckling as it is mentioned in expression (32).

The imperfection factor $\alpha$ is a function of the steel grade and is given by

$$\alpha = 0.65\sqrt{235/f_y} \tag{49}$$

EN1993-1-2, [11] does not take into account the moment distribution between lateral restraints of the beam in the computation of $M_{b,fi,t,Rd}$. Which means that a uniform distribution of the maximum moment along the beam is considered normally leading to conservation result. On the contrary, this aspect is considered in EN1993-1-1, [13] thought a factor $f$ that increase the resisting moment, computed function of the shape of bending moment diagram. By means of numerical investigation (Vila real et al) [15] showed that the shape of bending moment diagram along the beam is important also in case of fire and proposed a formula for the factor $f$ to be applied in the fire design situation as is the case at room temperature.

$$\chi_{LT,fi,\text{mod}} = \frac{\chi_{LT,fi}}{f} \text{ but } \chi_{LT,fi,\text{mod}} \leq 1 \tag{50}$$

With

$$f = 1 - 0.5(1 - k_c) \tag{51}$$

The correction factor $k_c$ is defined according to Table 6:

Table 6: Correction factors $k_c$ for the new proposal.

| Bending diagram | Class 1, 2, 3 sections $k_c$ |
|---|---|
| 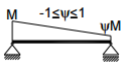  | $0.6+0.3\psi+0.15\psi^2$ but $k_c \leq 1$ |
|  | 0.79 |
|  | 0.91 |
| Note: for others bending diagrams $k_c = 1$. | |

# CHAPTER.3 STEEL TEMPERATURE DEVELOPMENT OF STEEL BEAMS EXPOSED TO FIRE

## 3.1 Introduction:

The effect of high temperatures on the structure following a fire can be described considering the heat flux transmitted by radiation and convection due to a temperature difference between the hot gas and the steel structural element.

The Eurocodes permit to verify the fire resistance to be determined by either simple or advanced calculation models. This guide covers simple models for both steel and composite members. The simple models offer the choice between calculation in the time domain (determining the time at which the fire resistance has fallen to the point of failure) or in the temperature domain (determining a uniform 'critical temperature' at which failure occurs), [9].

Several experimental and numerical modelling studies have been carried out in order to better understand the behaviour of structural elements under the effect of high temperatures and under scenario conditions of the most varied fire.

## 3.2 Steel temperature evolution using the simple calculation method

To determine the temperature evolution of different beams a set of two scripts were developed in Matlab, to study the behaviour of different solid cross section IPE (IPE220. IPE360 and IPE500) and equivalent cross section from HEB profile with and without fire protection material, considered gypsum boards.

A parametric analysis was done, considering different sections exposed to 3 sides and table below compare the section factors of both solid cross section (IPE and HEB profile) Section factor for unprotected solid beam is determined:

$$\left[\frac{A_m}{V}\right] = \left[\frac{\text{box surface area per unit length}}{\text{volume of the member per unit length}}\right]$$

Table 7: Section factor for unprotected solid beams.

| Cross section | IPE profile | | | HEA profile | | |
|---|---|---|---|---|---|---|
| | IPE220 | IPE360 | IPE500 | HEB220 | HEB360 | HEB500 |
| SF[$m^{-1}$] | 221 | 163 | 134 | 115 | 86 | 76 |
| Box SF[$m^{-1}$] | 165 | 122 | 104 | 72 | 56 | 54 |

The temperature evolution in function of time for different-unprotected sections solid beam made from IPE cross section is shown in Figure 17. A similar result is presented in Figure 18 For the HEB cross section sections Figure 19 present comparison between IPE and HEB cross section.

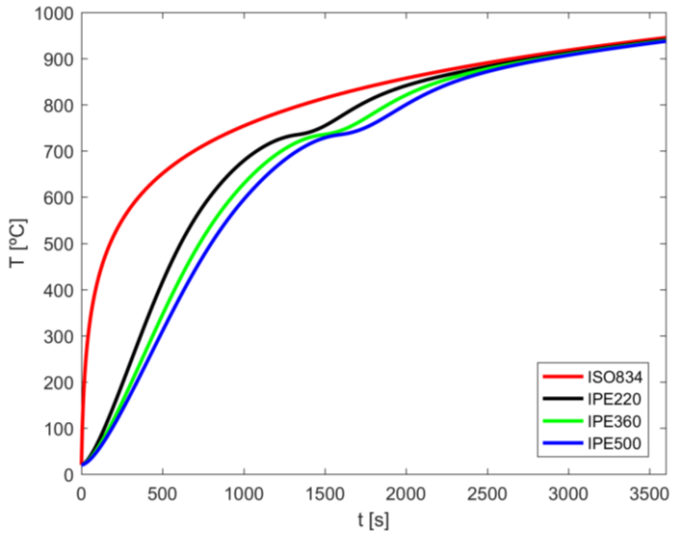


Figure 17: Temperature evolution for different unprotected IPE sections.

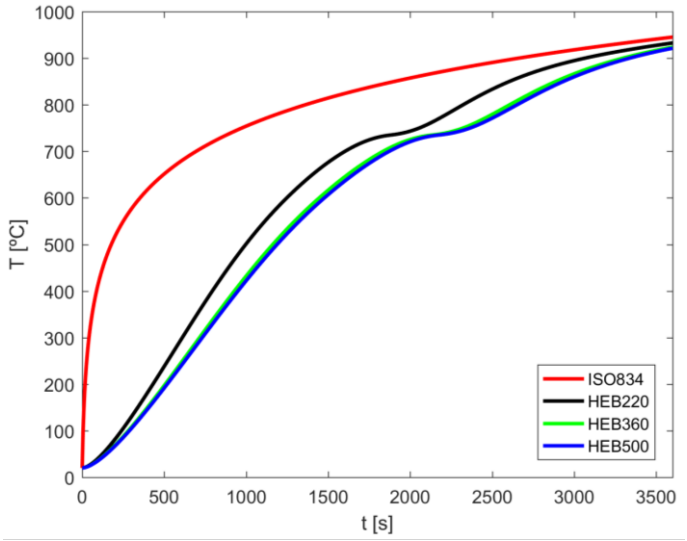


Figure 18: Temperature evolution for different unprotected HEB sections.

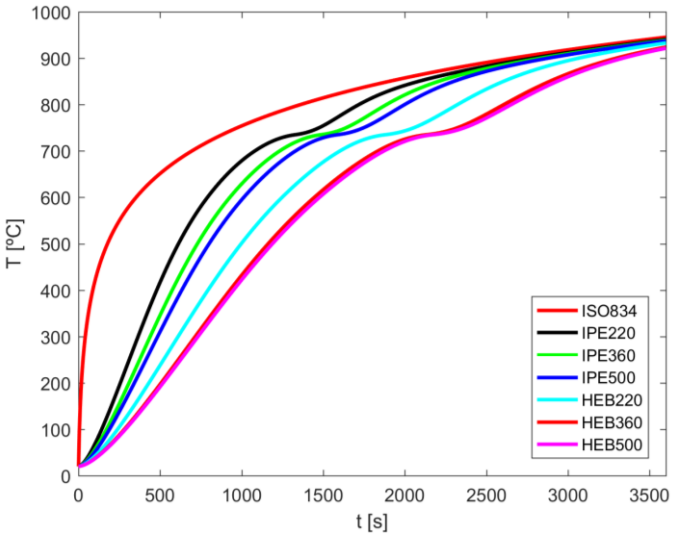


Figure 19: comparison of Temperature evolution for different unprotected HEB and IPE sections.

The temperature evolution of cross section increase faster and take less time to heat when the section factor Am/V is higher so as much the section factor is small, the cross section will heat slowly and take more time to active a specify temperature.

To study the behaviour of different solid cross section beams with fire protection, a similar study was done considering both types of sections, protected with Gypsum boards. The thermal properties considered for this calculation are presented in Table 8.

Table 8: Properties of gypsum boards.

| **Property** | **Value** |
|---|---|
| Thickness of gypsum – dp[mm] | 15 |
| Density of gypsum - $\rho_p$ [kg/m$^3$ ] | 800 |
| Specific Heat of gypsum - Cp [J/kg°K] | 1700 |
| Thermal Conductivity of gypsum kp [W/m°K] | 0.2 |

The protected sections studied are presented in Table 9 for fire exposures from 3 sides.

Table 9: Section factor for protected solid beams.

| Cross section | IPE profile | | | HEA profile | | |
|---|---|---|---|---|---|---|
| | IPE220 | IPE360 | IPE500 | HEB220 | HEB360 | HEB500 |
| $SF_P$[m$^{-1}$] | 165 | 122 | 104 | 72 | 56 | 54 |

The temperature evolution in function of time for different-protected sections solid beam made from IPE cross section is shown in Figure 20. A similar result is presented in Figure 21 for the HEB cross section sections of Table 7 and Figure 22 presents comparison between IPE and HEB cross section.

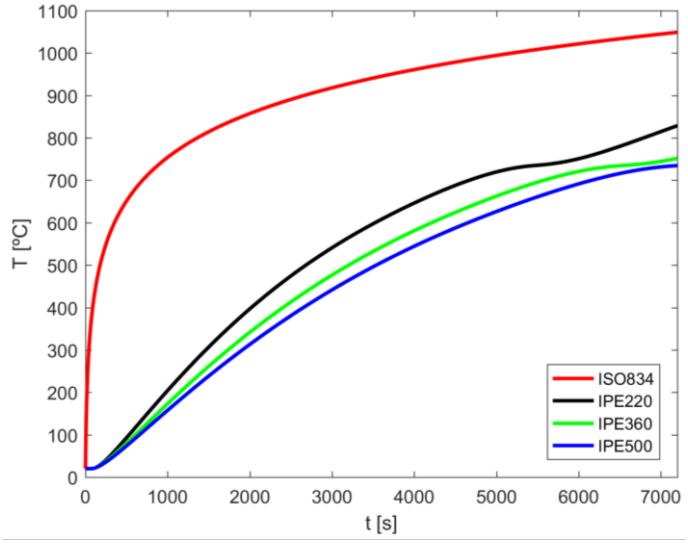


Figure 20: Temperature evolution for protected IPE solid beam.

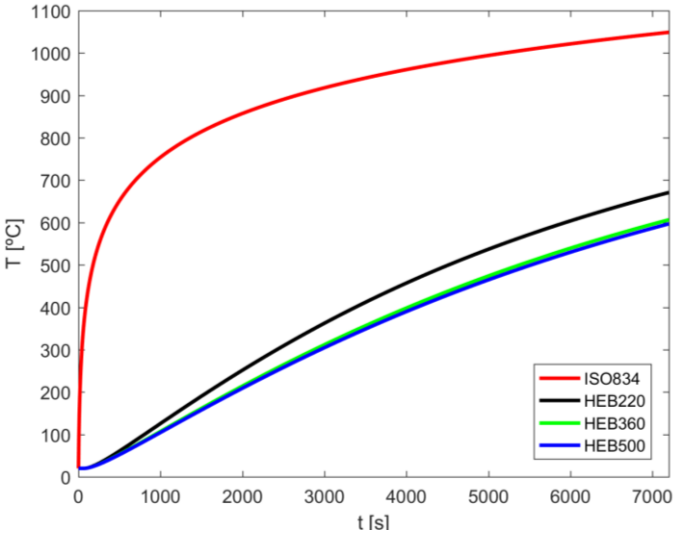


Figure 21: Temperature evolution for different protected HEB sections.

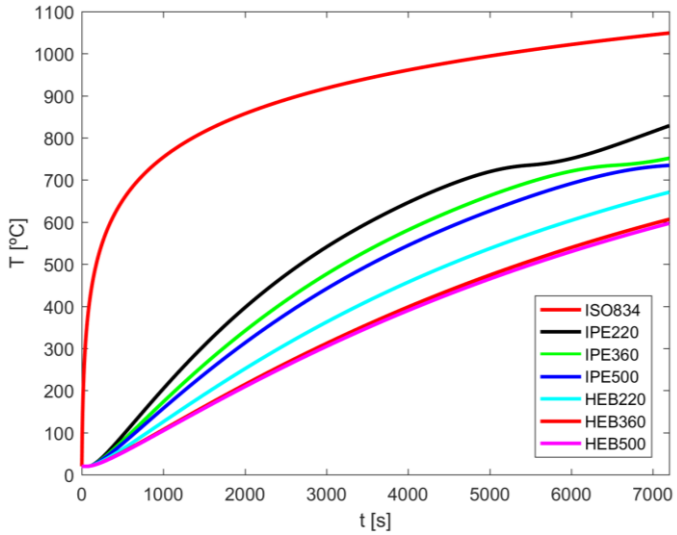


Figure 22: Comparison of temperature evolution for different unprotected HEB and IPE sections.

The result of temperature evolution for different solid beams protected with gypsum shows that, the cross section with height section factor heat faster than the section with small section factor. The section factor for insulated sections by a encasement are based on the dimensions of the section, h and b, even if the encasement does not touch the section and in that case, the surface that radiates energy to the steel section is the inside surface of the encasement.

### 3.3 Experimental fire tests of solid and cellular beams

To estimate the behaviour of solid and cellular beams and compare it the experimental result with simplified method with numerical results.

Experimental tests were performed at the Polytechnic Institute of Bragança to estimate the behaviour of solid and cellular beams with and without intumescent protection by Lamri B, [16].

All the sections are made from hot rolled IPE220 steel profiles with 600 [mm] length and in case of the cellular sections the circular holes cut directly from the web, resulting a section with the same height with different diameter web post and thickness of intumescent coating as represented in Table 10 and shown in following Figures.

Table 10: Geometries and properties of the tested beams, [16].

| Ref. | Beam type | DFT [μm] | D [mm] | W [mm] |
|---|---|---|---|---|
| P1 | Solid | - | - | - |
| P2 | Solid | - | - | - |
| P3 | Solid | 1047.3 | - | - |
| P4 | Solid | 1187.5 | - | - |
| P5 | Cellular | - | 120 | 60 |
| P6 | Cellular | - | 120 | 60 |
| P7 | Cellular | 860.4 | 120 | 60 |
| P8 | Cellular | 1311.0 | 120 | 60 |
| P9 | Cellular | - | 120 | 75 |
| P10 | Cellular | 960.4 | 120 | 75 |
| P11 | Cellular | 1205.4 | 160 | 75 |
| P12 | Cellular | - | 160 | 80 |
| P13 | Cellular | 993.7 | 160 | 80 |
| P14 | Cellular | 1360.0 | 160 | 80 |
| P15 | Cellular | - | 160 | 100 |
| P16 | Cellular | 943.0 | 160 | 100 |
| P17 | Cellular | 1424.0 | 160 | 100 |

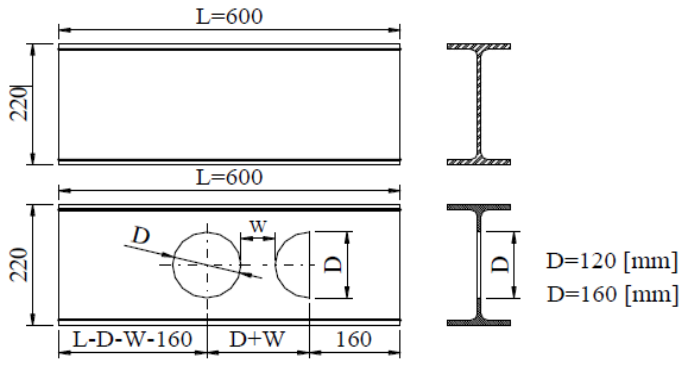


Figure 23: Dimensions of the tested solid and cellular beams, [16].

For the analysis of the steel temperature evolution several thermocouples type K were used as recommended by the standard EN13381-9, [17].

For the case of unprotected beams the thermocouples wires were welded to the steel surface but for the sections with fire protection, the thermocouples were installed after coating the steel member and mineral insulated thermocouples with Inconel sheath were used by means of a drilled hole of 2 [mm].

The fire resistance tests were performed on a fire furnace with interior dimensions of 1x1x1 [$m^3$] insulated with refractory bricks and ceramic fibre.

The specimens were placed inside the furnace protected with intumescent coating with the top flange insulated with ceramic mat in contact with the furnace roof, and with both ends protected representing an exposure condition as presented in Figure 24.

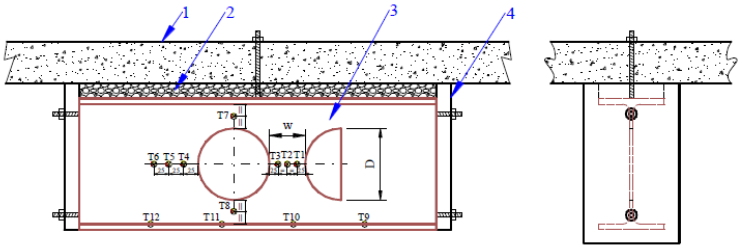


Figure 24: Test setup position and numbering of the thermocouples, [16].

### 3.3.1 Temperature results of solid and cellular beams

The steel temperature evolution of the tests was measured by the attached thermocouples. The flange temperature was determined by the thermocouples T9 to T12 and the web post temperatures by the thermocouples T1, T2 and T3. The data obtained from T7 and T8 can be used to verify the non-uniform temperature distribution across the section due to the three-side fire exposure.

The temperature evolution for the unprotected solid beams, P1, P2 is present in Figure 25, Figure 26 respectively.

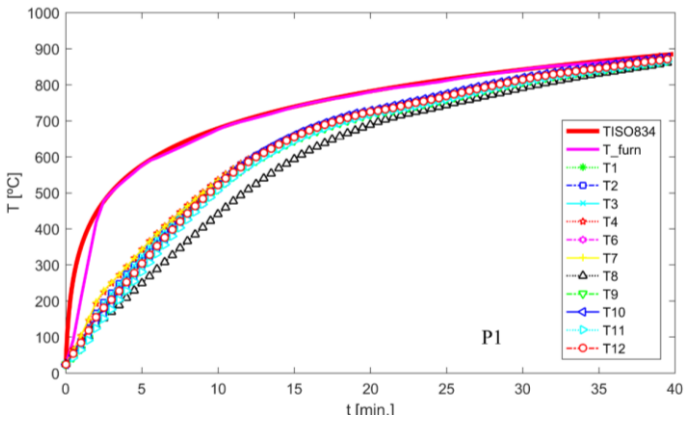


Figure 25**:** Temperature evolution results of unprotected solid beam P1, [16].

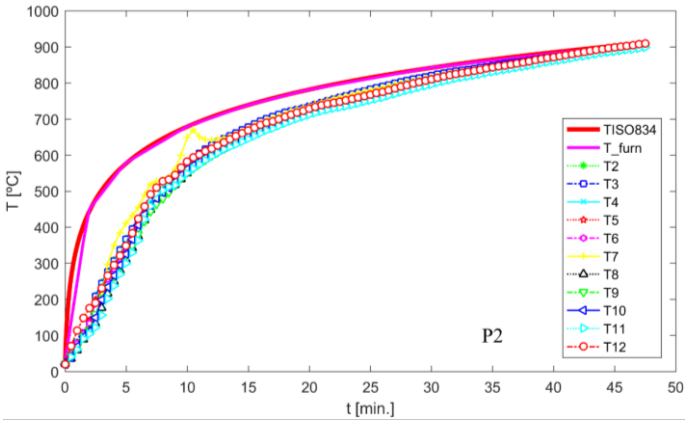


Figure 26: Temperature evolution results of unprotected solid beam P2, [16].

The temperature evolution for the unprotected cellular beams, P5 P6, P9, P12, P15 is presented in from Figure 27 to Figure 31 respectively.

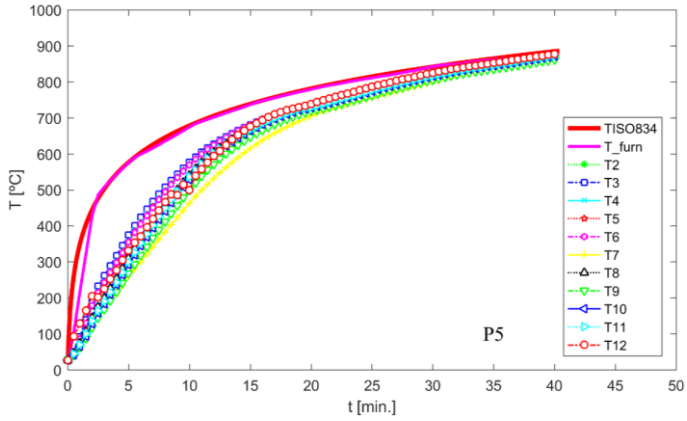


Figure 27: Temperature evolution for the unprotected cellular beams P5, [16].

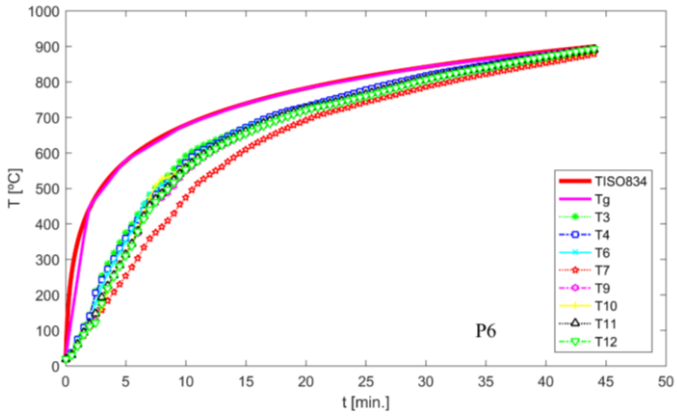


Figure 28**:** Temperature evolution results of unprotected cellular beam P6, [16].

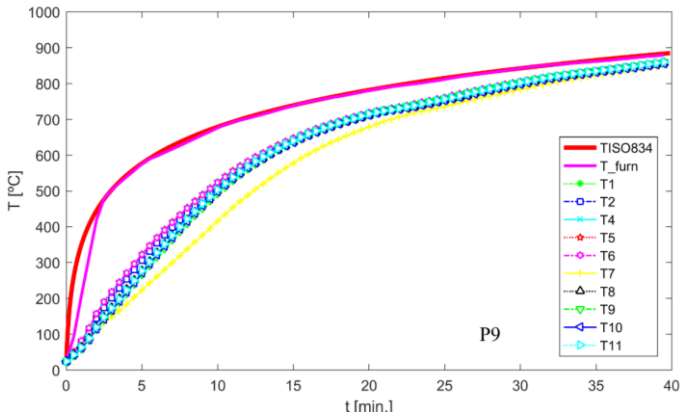


Figure 29**:** Temperature evolution results of unprotected cellular beam P9, [16].

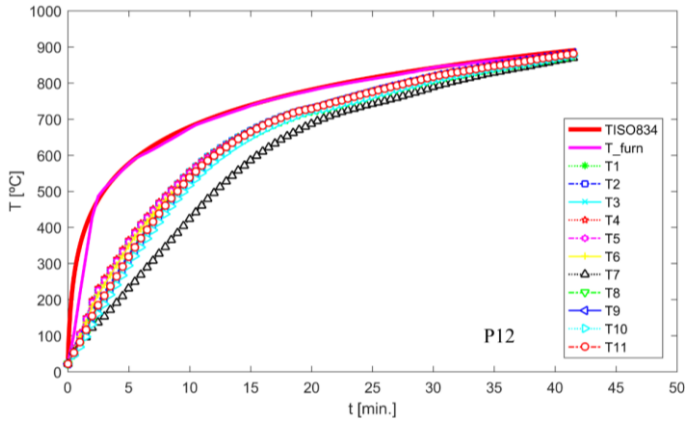


Figure 30**:** Temperature evolution results of unprotected cellular beam P12, [16].

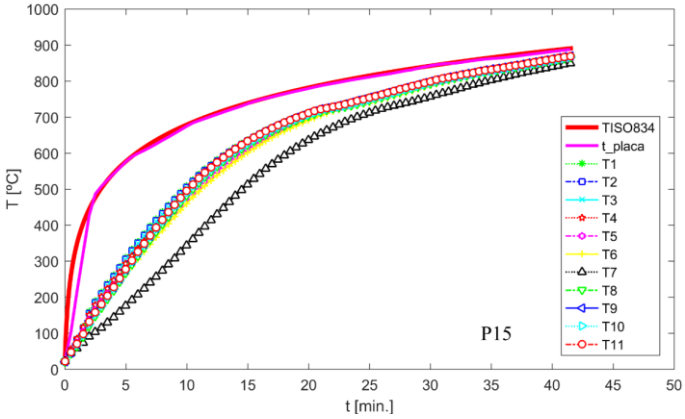


Figure 31**:** Temperature evolution results of unprotected cellular beam 15, [16].

### 3.4 Comparison between experimental results and simple calculation method

P1 and P2 are unprotected solid beams made from IPE220 shown in Table 10 the comparison between results of EC3-part 1-2, [11]which are obtained from Matlab and experimental results.

Table 11 present a comparison during time of temperature evolution according to Eurocode 3 and the mean temperature evolution in experimental test for unprotected solid beam P1 and these results illustrated in Figure 32.

Table 11: Experimental and EC-3 results for P1.

| P1 | | | |
|---|---|---|---|
| t (min) | T_EXP[°C] | T_EC3 [°C] | Diffrence [°C] |
| 0 | 24.1 | 20 | 4.1 |
| 0.5 | 52.72 | 27.86 | 24.86 |
| 1 | 81.44 | 43.24 | 38.2 |
| 5 | 306.46 | 253.8 | 52.66 |
| 10 | 516.18 | 513.35 | 2.82 |
| 15 | 648.03 | 661.27 | 13.24 |
| 20 | 720.21 | 728.77 | 8.55 |
| 25 | 764.87 | 765.11 | 0.24 |
| 30 | 810.16 | 821.86 | 11.7 |
| 35 | 842.25 | 854.28 | 12.03 |
| 40 | 870.55 | 877.1 | 6.55 |

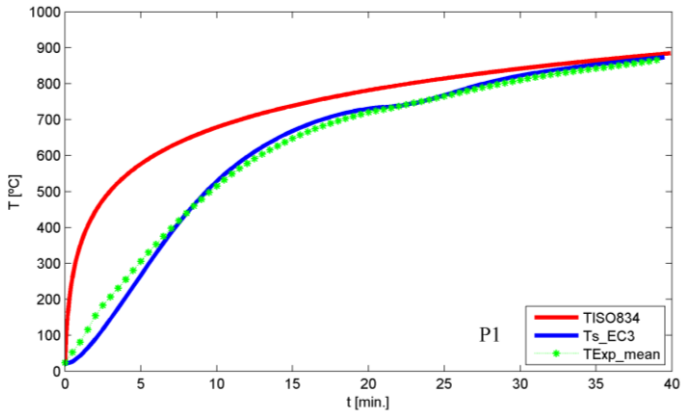


Figure 32: Eurocode and experimental mean temperature for P1.

Table 12 presents a comparison during time of temperature evolution according to Eurocode 3 and the mean temperature evolution in experimental test for unprotected solid beam P1 and this result illustrated in Figure 33.

Table 12: Experimental and EC-3 results for P2.

| P2 | | | |
|---|---|---|---|
| t (min) | T_EXP [°C] | T_EC3 [°C] | Diffrence[°C] |
| 0 | 20.54 | 20 | 0.53 |
| 0.5 | 45.17 | 26.79 | 18.38 |

| | | | |
|---|---|---|---|
| 1 | 76.57 | 43.09 | 33.48 |
| 5 | 345.5 | 267.4 | 78.1 |
| 10 | 570.27 | 528.31 | 41.96 |
| 15 | 663.75 | 668.41 | 4.65 |
| 20 | 725.89 | 730.29 | 4.39 |
| 25 | 769.32 | 767.91 | 1.41 |
| 30 | 810.24 | 767.91 | 42.33 |
| 35 | 840.61 | 853.03 | 12.42 |
| 40 | 867.14 | 875.49 | 8.35 |

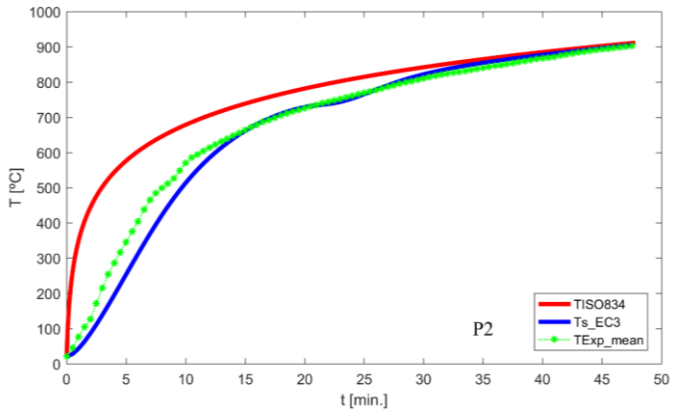


Figure 33: Eurocode and experimental mean temperature for P2.

Considering the result from P1 and P2. The mean temperature in experimental test increase faster and it is higher than the temperature evolution from the Eurocode up to almost 13 min, After both of Eurocode and experimental result have almost the same temperature evolution behaviour.

The same comparison is done for cellular beams, P6, P9, P12, and P15 they are unprotected cellular beam with IPE 220 cross section with different web-post dimensions and holes diameter. Which in experimental test the mean evolution temperature are considered in two points, the mean temperature in web-post (T_EXP_WP) and in the flange (T_EXP_F).

The evolution temperature results according to Eurocode 3 are obtained from different scripts developed in matlab; the results are shown below.

Table 13show the mean evolution temperature in experimental test in web-post, flange, and Eurocode temperature evolution for cellular beam P6 with diameter equal to 120mm and web-post equal to 60mm. the result is illustrated in Figure 34.

Table 13: Experimental and EC-3 results for P6.

| t(min) | T_EXP_WP | T_EXP_F | T-EC3 |
|---|---|---|---|
| 0.0 | 18.62 | 18.87 | 20.00 |
| 0.5 | 36.56 | 32.07 | 27.55 |
| 1 | 77.20 | 59.76 | 42.16 |
| 5 | 374.96 | 312.83 | 239.88 |
| 10 | 591.77 | 555.15 | 491.29 |
| 15 | 671.79 | 655.91 | 645.63 |
| 20 | 729.04 | 721.19 | 722.80 |
| 25 | 773.83 | 760.96 | 754.55 |
| 30 | 815.55 | 805.64 | 814.54 |
| 35 | 844.33 | 838.33 | 851.63 |
| 40 | 870.04 | 868.00 | 875.77 |

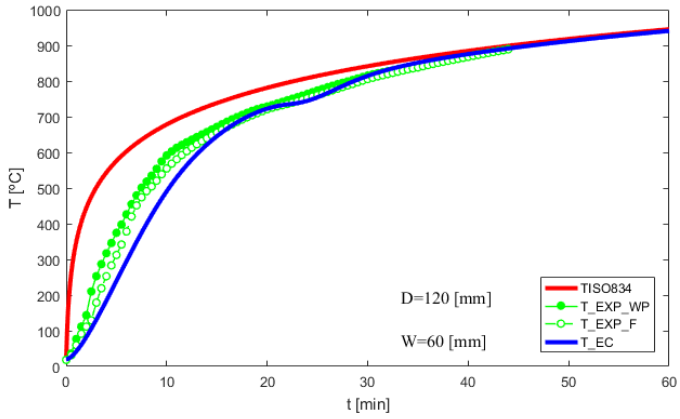


Figure 34: Eurocode and experimental mean temperature for P6.

Table 14 show the mean evolution temperature in experimental test in web-post and flange, and Eurocode temperature evolution for cellular beam P9 with diameter equal to 120mm and web-post equal to 75mm. and result are illustrated in Figure 35.

Table 14: Experimental and EC-3 results for P9.

| t(min) | T_EXP_WP | T_EXP_F | T-EC |
|---|---|---|---|
| 0 | 23.77 | 23.69 | 20.00 |
| 0.50 | 46.83 | 42.07 | 27.55 |
| 1 | 73.51 | 62.38 | 42.16 |
| 5 | 307.18 | 273.94 | 239.88 |
| 10 | 513.64 | 499.88 | 491.29 |
| 15 | 640.65 | 638.79 | 645.63 |
| 20 | 712.33 | 714.12 | 722.80 |
| 25 | 754.49 | 755.78 | 754.55 |
| 30 | 800.36 | 802.29 | 814.54 |
| 35 | 830.61 | 833.81 | 851.63 |
| 40 | 857.69 | 860.80 | 875.77 |

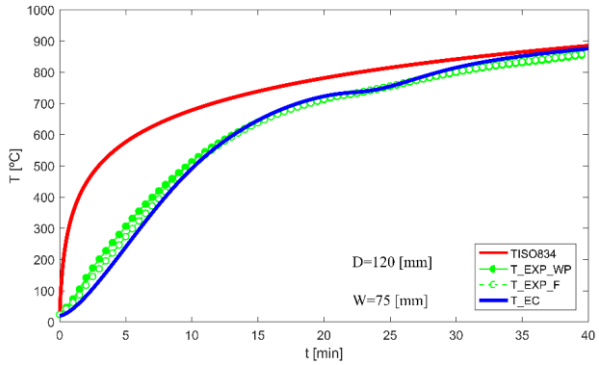


Figure 35: Eurocode and experimental mean temperature for P9.

The temperature evolution in experimental test for P6 and P9 are higher and increase faster than the Eurocode up 13 min after almost they have the same behaviour of temperature evolution. The temperature evolution in web-post is always higher than in the flange and Eurocode. Table 15 show the mean evolution temperature in experimental test in web-post and flange and Eurocode temperature evolution for cellular beam P12 with diameter equal to 160mm and web-post equal to 80mm. and result is illustrated in Figure 36.

Table 15: Experimental and EC-3 results for P12.

| t(min) | T_EXP_WP | T_EXP_F | T-EC3 |
|---|---|---|---|
| 0 | 21.47 | 21.83 | 20.00 |
| 0.5 | 61.30 | 49.82 | 30.72 |
| 1 | 101.59 | 76.87 | 51.13 |
| 5 | 361.07 | 306.45 | 306.26 |
| 10 | 555.44 | 528.41 | 566.39 |
| 15 | 669.34 | 659.20 | 688.72 |
| 20 | 730.70 | 726.63 | 735.34 |
| 25 | 777.72 | 772.31 | 785.20 |
| 30 | 817.19 | 814.81 | 830.25 |
| 35 | 846.26 | 845.22 | 857.38 |
| 40 | 872.24 | 872.16 | 878.98 |

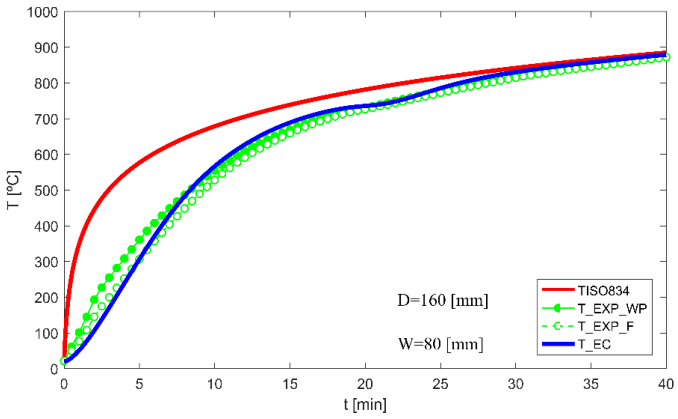


Figure 36: Eurocode and experimental mean temperature for P12.

The evolution of temperature in web-post is higher than temperature evolution in the flange and Eurocode. In the first minutes, the evolution of temperature in web post is to much higher and noticeable but after along the time the difference of temperature evolution decrease but still always the highest temperature.

Table 16, show the mean evolution temperature in experimental test in web-post and flange and Eurocode temperature evolution for cellular beam P15 with diameter equal to 160mm and web-post equal to 100mm. is result are illustrated in Figure 37.

Table 16: Eurocode and experimental mean temperature for P15.

| t(min) | T_EXP_WP | T_EXP_F | T-EC3 |
|---|---|---|---|
| 0 | 22.00 | 21.58 | 20.00 |
| 0.5 | 53.50 | 45.39 | 30.72 |
| 1 | 82.70 | 68.59 | 51.13 |
| 5 | 306.44 | 273.71 | 306.26 |
| 10 | 505.94 | 490.85 | 566.39 |
| 15 | 634.83 | 629.53 | 688.72 |
| 20 | 710.98 | 708.30 | 735.34 |
| 25 | 754.62 | 751.32 | 785.20 |
| 30 | 798.53 | 796.63 | 830.25 |
| 35 | 830.19 | 830.06 | 857.38 |
| 40 | 857.90 | 858.72 | 878.98 |

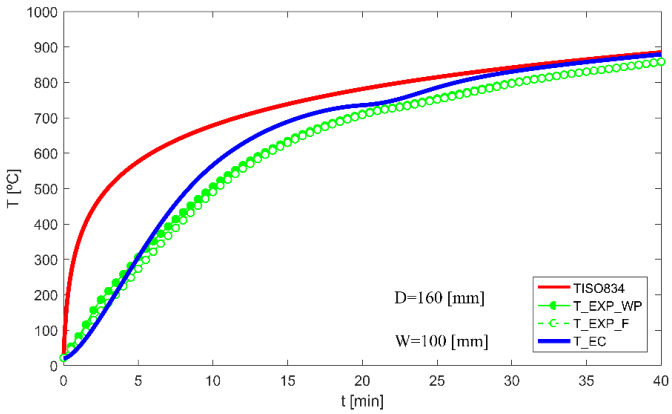


Figure 37: Eurocode and experimental mean temperature for P15.

In the first 5 min the evolution of the temperature in web post is faster after that we can notice that evolution of temperature from Eurocode follow the experimental test temperature results.

From all result above, we conclude that the web post width and diameter of holes influence in the temperature evolution in the cellular beam.

## 3.5 Thermal analysis using the Finite Element Method

### 3.5.1 Numerical modelling of steel beams in fire

ANSYS 16.2 is a general-purpose Finite Element Analysis (FEA) program that solves a vast area of solid and structural mechanics problems in geometrically complicated regions. ANSYS provides solutions for many type of analysis and is a commercial general-purpose finite element analysis program.

To simulate thermal behaviour of solid and cellular beams in fire condition with three-dimensional model using ANSYS software, one layer thermal 3-D shell element SHELL131 with four nodes with one layer was used. It allows for in plane and through thickness thermal conduction capability applicable to a 3-D transient thermal analysis, using the heat flow as the convergence on time ($10^{-3}$).

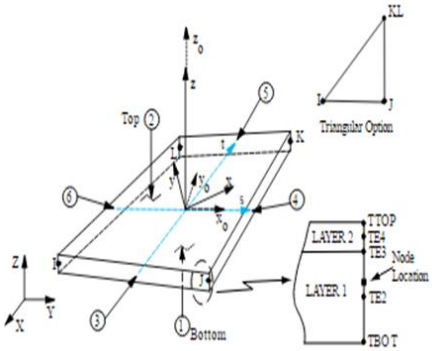


Figure 38: Finite element SHELL131.

Solid and cellular steel beams are subjected to fire conditions according to the standard fire nominal curve ISO834. Figure 39 present typical FE mesh of solid and cellular models.

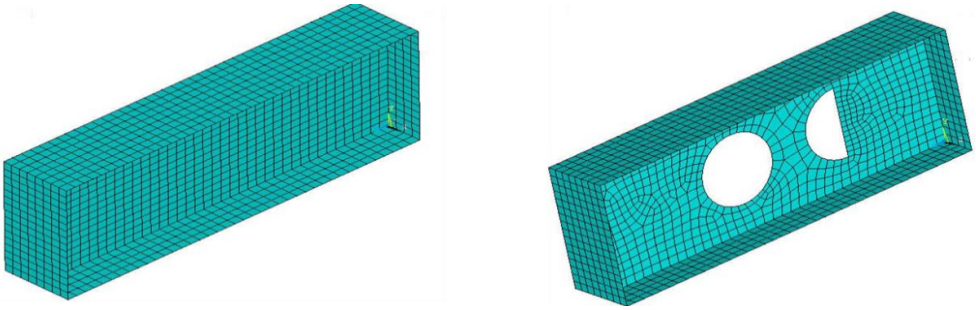

Figure 39: Typical FE mesh of solid and cellular models.

The simulations account for radiation with the emissivity coefficient εr of 0.7 at steel surface and convection with constant convective coefficient $\alpha c$= 25[W/m²K].

Steel beams finite element model accounts for three exposed sides assuming that top flange is insulated so that heat flux is zero on the top of the flange.

The beam-ends that are insulated by ceramic mat layer of 50 [mm] are modelled by shell elements with applied convection and radiation.

Validation of the thermal model is done against experimental fire furnace test performed at the Polytechnic Institute of Bragança to evaluate the behaviour cellular beams under fire condition. The sections is made from hot rolled IPE220 steel profile with 600 [mm] length with circular holes cut directly into the web as represented in Figure 24.

The figure below show the temperature distribution in solid and cellular beam finite element model.

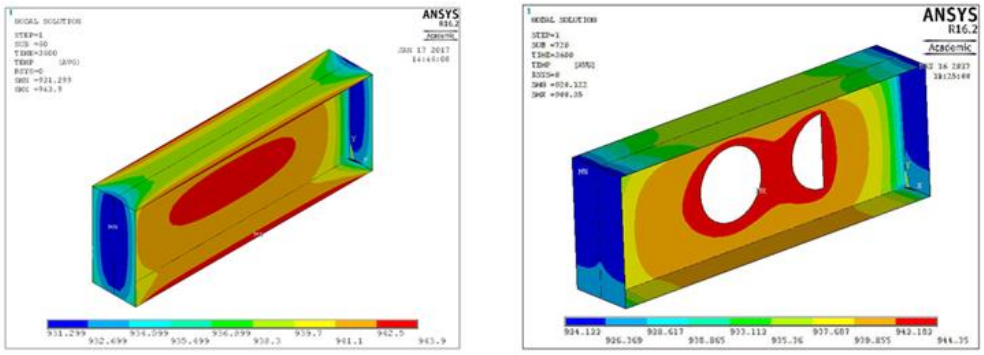


Figure 40: Distribution of temperature in solid and cellular element model.

3.5.2 Comparison between the experimental. Numerical and simple calculation method results

The result below presents a comparison of temperature evolution for unprotected solid and cellular beams between simple calculation methods which is illustrated in results (T_EC) and experimental test, The mean temperature is measured in the flange (T_EXP_F) and in web post (T_EXP_WP) of the beams and numerical results obtained from transient thermal analysis by ANSYS. The result was taken in top of beam (T_T) and in the web post (T_M) and in the bottom (T_B)

Table 17 to Table 21 present comparison result of solid beam P2 and cellular beams with different web post and diameter. P6, P9, P12, P15 respectively, considering the time to

reach a reference temperatures of (500, 550 and 600) [ºC] and the global average steel temperature for 15 and 30 [min] for simple method, experimental and numerical analysis.

Figure 41 to Figure 45 illustrate the temperature evolution during time for simple method, experimental and numerical analysis for the solid beam P2 and cellular beams with different web post and diameter. P6, P9, P12, P15 respectively.

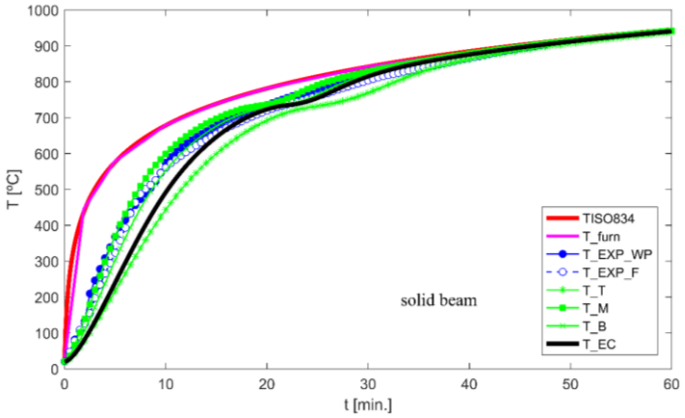


Figure 41: Comparison curve for solid beam P2.

Table 17: Average temperature of simple method, experimental and numerical analysis for P2.

| | **T[°C]** | | **t[min]** | | |
|---|---|---|---|---|---|
| | 15min | 30min | 500°C | 550°C | 600°C |
| T_EXP_WP | 677.90 | 819.87 | 8.37 | 9.56 | 10.85 |
| T_EXP_F | 654.95 | 803.57 | 7.95 | 9.65 | 11.81 |
| T_TOP | 599.29 | 768.81 | 11.55 | 13.14 | 15.03 |
| T_MIDLE | 697.35 | 828.44 | 7.30 | 8.50 | 10.05 |
| T_BOTTOM | 676.13 | 820.078 | 8.64 | 9.92 | 11.51 |
| T_EC3 | 645.94 | 814.68 | 10.20 | 11.54 | 13.16 |

The result above show that both of experimental and numerical results have the same temperature evolution but in top of flange from numerical analysis (T_TOP) take more time to reach the reference temperatures and less temperature in reference time due to insulation.

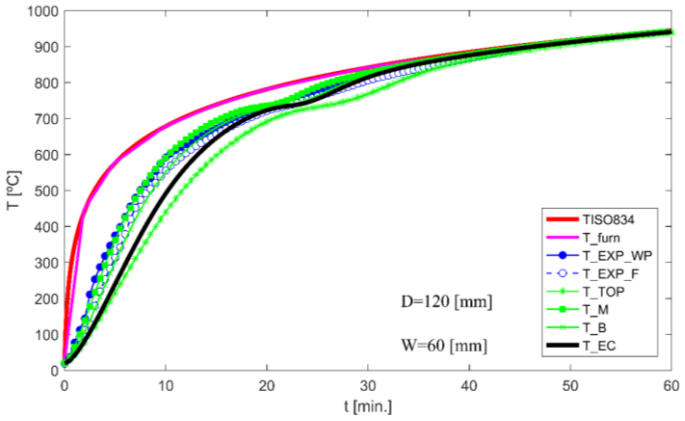


Figure 42: Comparison curves for cellular beam P6.

Table 18: Average temperature of simple method, experimental and numerical analysis for P6.

| | **T[°C]** | | **t[min]** | | |
|---|---|---|---|---|---|
| | 15min | 30min | 500°C | 550°C | 600°C |
| T_EXP_WP | 671.79 | 815.55 | 7.74 | 8.89 | 10.36 |
| T_EXP_F | 655.90 | 805.63 | 8.31 | 9.84 | 11.83 |
| T_TOP | 596.86 | 768.06 | 11.65 | 13.24 | 15.13 |
| T_MIDLE | 693.62 | 827.01 | 7.49 | 8.74 | 10.32 |
| T_BOTTOM | 674.78 | 819.11 | 8.68 | 9.96 | 11.57 |
| T_EC3 | 645.63 | 814.53 | 10.21 | 11.56 | 13.17 |

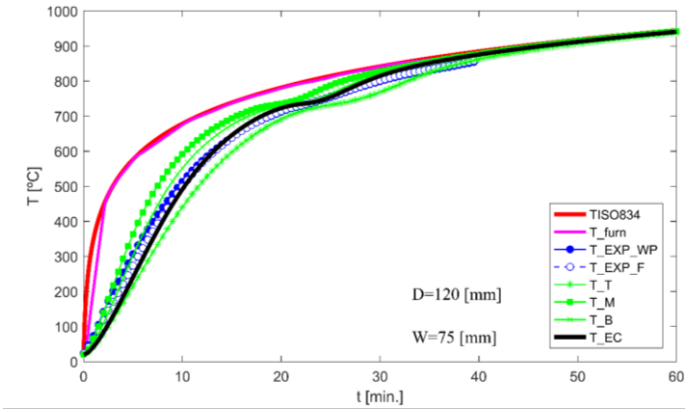


Figure 43: Comparison curve for cellular beam P9.

The result above show that both of experimental and numerical results have the same temperature evolution behaviour but in top of flange from numerical analysis (T_TOP) take more time to reach the reference temperatures and less temperature in reference time due to insulation.

Table 19: Average temperature of simple method, experimental and numerical analysis for P9.

| | **T[°C]** | | **t[min]** | | |
|---|---|---|---|---|---|
| | 15min | 30min | 500°C | 550°C | 600°C |
| T_EXP_WP | 640.19 | 799.35 | 9.62 | 11.16 | 13.12 |
| T_EXP_F | 638.27 | 801.31 | 8.31 | 11.46 | 13.29 |
| T_TOP | 597.26 | 768.24 | 11.63 | 13.22 | 15.11 |
| T_MIDLE | 693.97 | 827.12 | 7.47 | 8.71 | 10.29 |
| T_BOTTOM | 674.91 | 819.18 | 8.67 | 9.95 | 11.56 |
| T_EC3 | 645.63 | 814.53 | 10.21 | 11.56 | 13.17 |

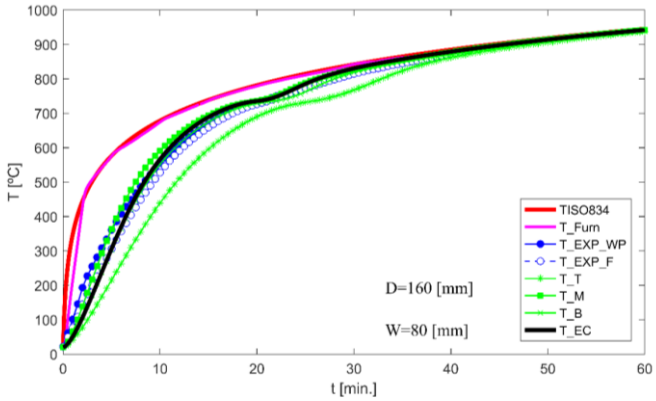


Figure 44: Comparison curve for cellular beam P12.

Table 20: Average temperature of simple method, experimental and numerical analysis for P12.

| | T[°C] | | t[min] | | |
|---|---|---|---|---|---|
| | 15min | 30min | 500°C | 550°C | 600°C |
| T_EXP_WP | 668.98 | 817.16 | 8.38 | 9.85 | 11.62 |
| T_EXP_F | 658.83 | 814.78 | 9.26 | 10.63 | 12.34 |
| T_TOP | 595.45 | 767.35 | 11.68 | 13.29 | 15.19 |
| T_MIDLE | 693.7 | 827.07 | 7.48 | 8.73 | 10.31 |
| T_BOTTOM | 674.62 | 818.95 | 8.67 | 9.96 | 11.57 |
| T_EC3 | 688.72 | 830.25 | 8.37 | 9.55 | 11.02 |

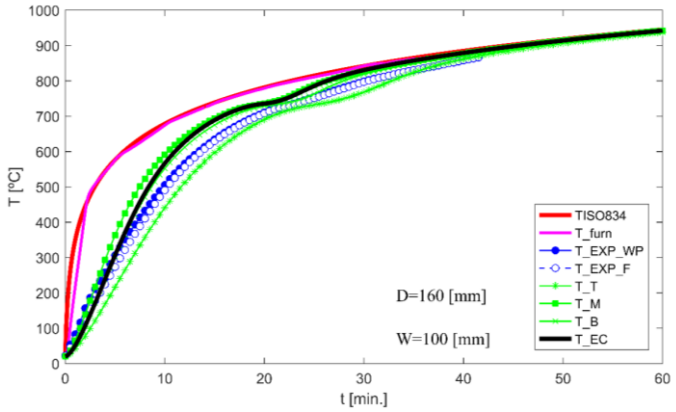


Figure 45: Comparison curve for cellular beam P15.

Table 21: Average temperature of simple method, experimental and numerical analysis for P15.

| | T[°C] | | t[min] | | |
|---|---|---|---|---|---|
| | 15min | 30min | 500°C | 550°C | 600°C |
| T_EXP_WP | 634.62 | 798.49 | 9.84 | 11.82 | 13.39 |
| T_EXP_F | 629.15 | 796.59 | 10.26 | 11.79 | 13.68 |
| T_TOP | 596.7 | 768.15 | 11.64 | 13.24 | 15.13 |
| T_MIDLE | 693.76 | 827.02 | 7.47 | 8.72 | 10.30 |
| T_BOTTOM | 674.96 | 819.16 | 8.65 | 9.94 | 11.55 |
| T_EC3 | 688.72 | 830.25 | 8.37 | 9.55 | 11.02 |

The results above present a comparison of temperature evolution between experimental test, numerical model and Eurocode. The temperature in web post is in all cases higher than the bottom or top of cross section and reach reference temperatures faster. The top of beams reach needs more time to reach the reference temperature. The results present a good correlation between the finite element calculation and the tests; therefore, the finite element model can be considered precise enough to run thermal analyses on solid and cellular beams.

# CHAPTER.4 THERMOMECHANICAL NUMERICAL ANALYSIS OF SOLID AND CELLULAR BEAMS IN FIRE

## 4.1 Introduction

It is well known that steel among all materials suffers a great reduction of yield stress and Young's modulus under the effect of high temperatures. Remarkable progress has been made during the last decade in understanding the parameters, which influence the development of building fires and the behaviour of fire exposed structural materials and structures. In particular, for steel structures, this progress has resulted in detailed rules for the design and calculation of structural steel beam behaviour and load bearing capacity in fire the failure of steel beam is reached when its strength is exceeded at one or more particular points known as plastic hinges depending on the way it is supported. Extensive research has been carried out in recent years on the numerical simulation using finite element method (FEM) as an alternative to the original plastic hinge analysis method. Moreover, when dealing with open cross-section cellular beam significant phenomenon of collapse mechanisms occur and early research studies dealt with under ambient temperatures. Under fire conditions. studies were to dedicated solid beams and other projects considering heated cellular beams cases seeking for a good understanding of their performance as isolated members, [18].To investigate the thermomechanical behaviour of solid and cellular beam under fire condition. thermomechanical numerical analysis are done using finite element software ANSYS Thermomechanical numerical model.

The finite element software ANSYS was used to investigate the behaviour of solid and cellular steel beams. The beam models were meshed using Structural SHELL181 finite element. Model is generated along the seven meters span of the beam and through both flanges and web of the different beams with nonlinear material and large displacement behaviour considered in the analyses. This finite element presents four nodes with six DOF per node. Which are translations and rotations on the X. Y. and Z-axis. respectively Figure 46 [19].

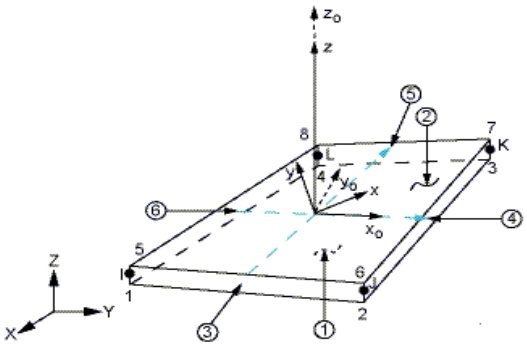


Figure 46: Finite element SHELL181.

The finite element models are fork supported at both ends; with uniform distributed load applied on nodes, varying with time ($q = 100t$) and constant temperature distribution in all elements.

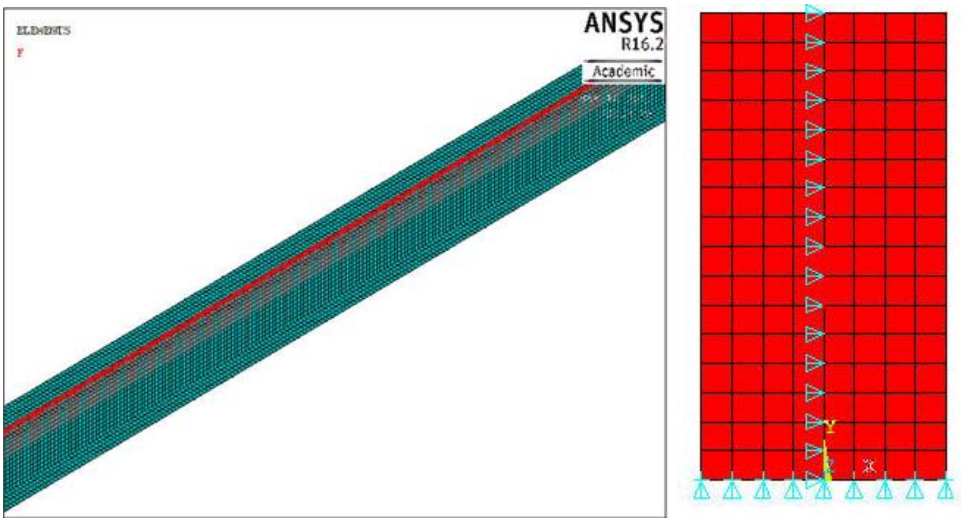


Figure 47: Mesh and boundary condition applied.

## 4.2 Cross section resistance numerical results and comparison with the Eurocode

A set of simulations were done in beams with 7 [m] span with an IPE220 cross section. Figure 48 presents the vertical displacement for different temperature from 20 [°C] to 800 [°C] varying with time in function of load.

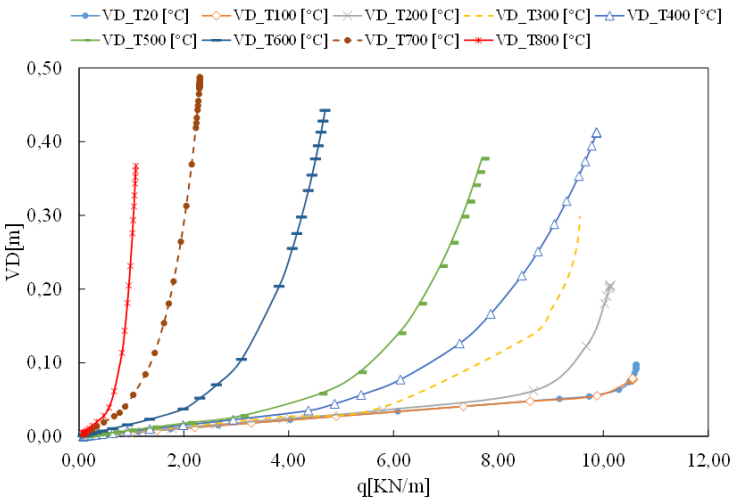


Figure 48: vertical displacement for different temperatures.

The applied mechanical load increases along the time. Beams underwent vertical displacements increasing progressively and linearly, until the beam is exposed to constant temperature 500°C. After that the vertical displacement increased very quickly with the load.

Table 22 present comparison results of the bending resistance for varying temperatures from 20°C until 800 ºC According to EN 1993-1-2 [11] obtained by equation (43) with the numerical analysis result.

Table 22: Bending resistance moment from EC3 and numerical result.

| T[°C] | Mr,d y[KN.m] | Mfi,o,Rd,Ansys[KN.m] | Mfi,o,Rd,Ansys/Mrd |
|---|---|---|---|
| 20 | 64,218 | 65,085 | 1,01 |
| 100 | 64,218 | 64,678 | 1,01 |
| 200 | 64,218 | 62,061 | 0,97 |
| 300 | 64,218 | 58,488 | 0,91 |
| 400 | 64,218 | 60,456 | 0,94 |
| 500 | 50,090 | 47,047 | 0,73 |
| 600 | 30,183 | 28,755 | 0,45 |
| 700 | 14,770 | 14,119 | 0,22 |
| 800 | 7,064 | 6,646 | 0,10 |

Figure 49 present the reduction factors plot of yield strength from Eurocode [11] and numerical results and it obtained from rapport between resistance moment at elevated temperature Mfi.θ,Rd and resistance moment at ambient temperature $M_{R,d}$, equal to the bending plastic resistance.

$$k_{y,\theta} = M_{fi,\theta,Rd} / M_{R,d} \tag{52}$$

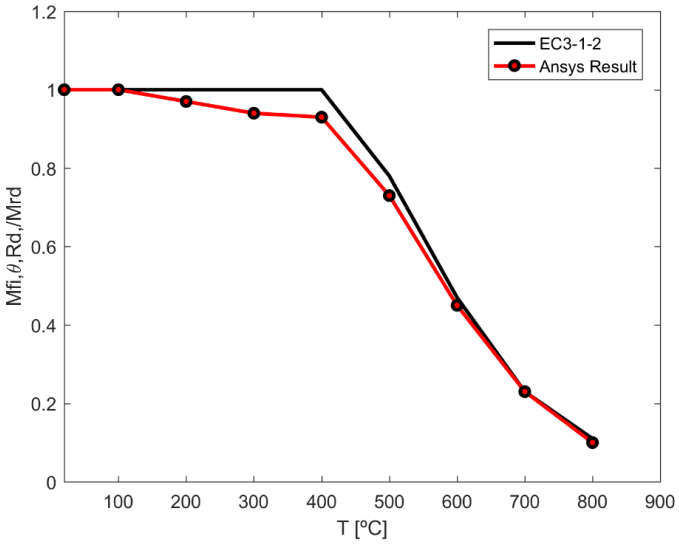


Figure 49: Reduction factor from EC3 and numerical analysis

Result from table and the graph illustrated in Figure 49 that from numerical analysis the resistance start to decrease after 100[°C] and this decrease due to effect of elastic modulus.

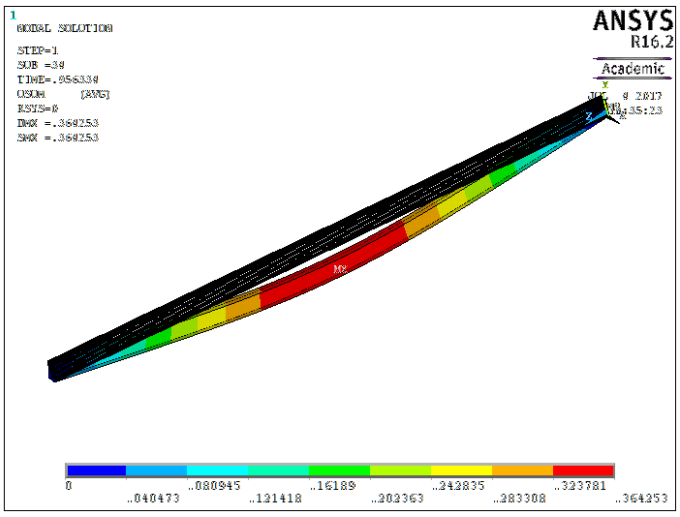


Figure 50: Solid beam IPE 220. T=500°C-max vertical deflection.

### 4.2.1 Cross section resistance of cellular beams

The finite element method has been widely used to study the failure of cellular beams a three-dimensional (3D) finite element model was simulated in this study using the ANSYS software package. The FE analysis considers both geometrical and material non-linarites. To allow for an explicit simulation of the various deformed shapes. The beam models were

meshed using the 4-node shell element. SHELL181. This element has six degrees of freedom at each node, Namely 3 translations and 3 rotations (in the x, y and z directions). The element is suitable for thin to moderately thick shell structures element sizes H/16 was used the general cellular beam.

Geometry and the imposed boundary conditions are shown in Figure 51, the investigated FE beam models of steel grade S355, beams are fork supported at both ends with uniform distributed load applied on nodes, varying with time ($q = 100t$), and constant temperature distribution. In all elements was conducted to checks cross-section resistance at web opening and post locations, shear buckling of the web and resistance of the beam to the lateral torsional buckling according to the principles of Eurocode 3 [11].

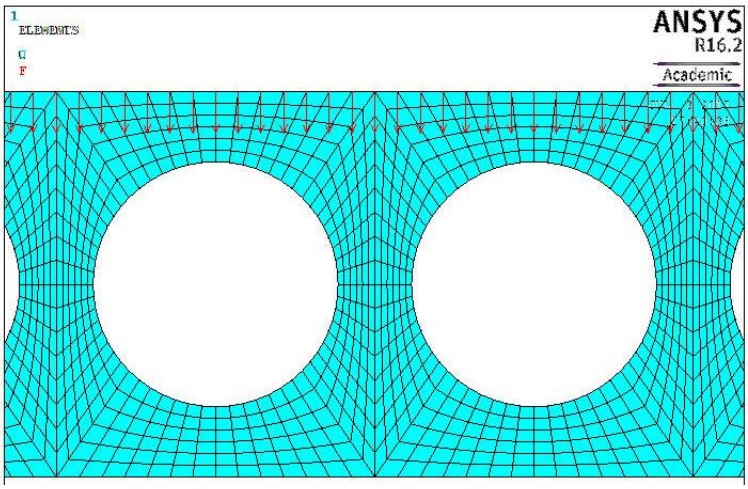


Figure 51: cellular beam finite element model.

A parametric analysis is performed for different cellular beams, considering the variation of temperatures and different cross section, presented in Table 23. The table shows the geometric dimensions of the analysed cellular beams, where h is the initial height of section and b is the width of cross section, a0 denote the holes diameter, w is web post width. $H_f$ is the final height of cellular beam. S denote web post width plus diameter a0 ,w0. $w_f$ are the width of solid ends of cellular beam. N holes is number of holes along the length and for all cases, the length was considered 7 meters.

a0/h holes diameter to the section height ratios and w/a0 web post width to hole diameter ration Hf/h final cross section height to initial height ratio.

Table 23: Dimensions and parameter considering for study cases.

| Case | Section | h | b | a0/h | w/a0 | Hf/h | a0 | w | Hf | S | N holes | w0.wf |
|---|---|---|---|---|---|---|---|---|---|---|---|---|

| | | | | | | | | | | | | |
|---|---|---|---|---|---|---|---|---|---|---|---|---|
| 1 | IPE 220 | 220 | 110 | 0.8 | 0.3 | 1.3 | 176.0 | 52.8 | 286.0 | 228.8 | 30.0 | 68.0 |
| 2 | IPE 600 | 600 | 220 | 0.8 | 0.3 | 1.3 | 480.0 | 144.0 | 780.0 | 624.0 | 10.0 | 380.0 |
| 3 | HE 220 A | 210 | 220 | 0.8 | 0.3 | 1.3 | 168.0 | 50.4 | 273.0 | 218.4 | 31.0 | 114.8 |
| 4 | HE 600 A | 590 | 300 | 0.8 | 0.3 | 1.3 | 472.0 | 141.6 | 767.0 | 613.6 | 11.0 | 125.2 |
| 5 | HE 220 B | 220 | 220 | 0.8 | 0.3 | 1.3 | 176.0 | 52.8 | 286.0 | 228.8 | 30.0 | 68.0 |
| 6 | HE 600 B | 600 | 300 | 0.8 | 0.3 | 1.3 | 480.0 | 144.0 | 780.0 | 624.0 | 10.0 | 380.0 |

Figure 52 present maximum vertical deflection case 1 section IPE220.

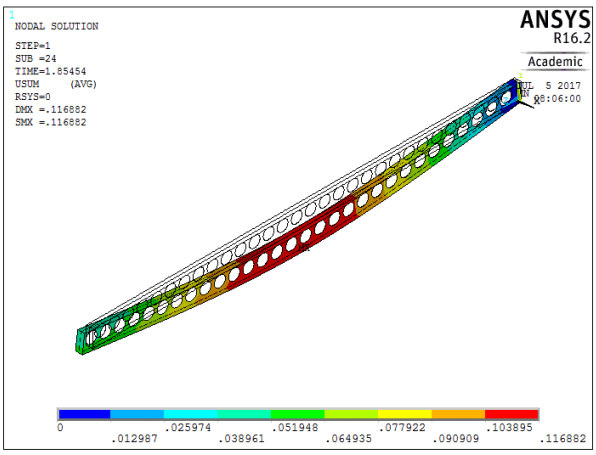


Figure 52: Maximum vertical deflection case 1 section IPE220.

Table 24 present results from numerical simulation the bending resistance moment corresponding to maximum load Qmax, and analytical result as plastic resistance moment for solid section Mpl -solid from Eurocode [11] and plastic bending resistance moment of Tee section Mpl.T.Rd given in equation(49), [14].

Table 24: Comparison between analytical and Ansys bending resistance.

| **Case 1 IPE220** | | | | | | | | | |
|---|---|---|---|---|---|---|---|---|---|
| **Temperature [°C** | **20°C** | **100°C** | **200°C** | **300°C** | **400°C** | **500°C** | **600°C** | **700°C** | **800°C** |
| Qmax[KN/m] | 20.088 | 20.057 | 18.035 | 15.646 | 13.890 | 11.366 | 5.482 | 2.521 | 1.421 |
| M Ansys[KN.m] | 123.04 | 122.85 | 110.47 | 95.83 | 85.07 | 69.61 | 33.57 | 15.44 | 8.70 |
| Mpl.T.Rd[KN.m] | 120.72 | 120.72 | 120.72 | 120.72 | 120.72 | 94.16 | 56.74 | 27.77 | 13.28 |
| Mpl -solid | 136.94 | 136.94 | 136.94 | 136.94 | 136.94 | 106.81 | 64.36 | 31.50 | 15.06 |
| **Case2 IPE600** | | | | | | | | | |
| Qmax[KN/m] | 163.078 | 161.676 | 142.534 | 127.669 | 108.044 | 89.402 | 48.726 | 26.542 | 13.168 |
| M Ansys[KN.m] | 998.85 | 990.27 | 873.02 | 781.98 | 661.77 | 547.59 | 298.45 | 162.57 | 80.66 |
| Mpl.T.Rd[KN.m] | 1470.22 | 1470.22 | 1470.22 | 1470.22 | 1470.22 | 1146.77 | 691.00 | 338.15 | 161.72 |
| Mpl -solid | 1715.60 | 1715.60 | 1715.60 | 1715.60 | 1715.60 | 1338.17 | 806.33 | 394.59 | 188.72 |
| **Case4 HE600A** | | | | | | | | | |
| Qmax[KN/m] | 181.972 | 181.021 | 170.315 | 157.372 | 139.125 | 117.818 | 68.943 | 30.900 | 20.395 |

| | | | | | | | | | |
|---|---|---|---|---|---|---|---|---|---|
| M Ansys[KN.m] | 1114.58 | 1108.75 | 1043.18 | 963.90 | 852.14 | 189.26 | 721.63 | 422.27 | 124.92 |
| Mpl.T.Rd[KN.m] | 2311.67 | 2311.67 | 2311.67 | 2311.67 | 2311.67 | 1803.10 | 1086.48 | 531.68 | 254.28 |
| Mpl -solid | 2568.71 | 2568.71 | 2568.71 | 2568.71 | 2568.71 | 2003.59 | 1207.29 | 590.80 | 282.56 |
| **Case6 HE600B** | | | | | | | | | |
| Qmax[KN/m] | 223.355 | 222.442 | 222.155 | 215.141 | 189.498 | 156.944 | 94.368 | 45.132 | 23.326 |
| M Ansys[KN.m] | 1368.05 | 1362.46 | 1360.70 | 1317.74 | 1160.67 | 961.28 | 578.01 | 276.44 | 142.87 |
| Mpl.T.Rd[KN.m] | 2792.43 | 2792.43 | 2792.43 | 2792.43 | 2792.43 | 2178.10 | 1312.44 | 642.26 | 307.17 |
| Mpl -solid | 3109.37 | 3109.37 | 3109.37 | 3109.37 | 3109.37 | 2425.31 | 1461.41 | 715.16 | 342.03 |

From the results presented in Table 24, the results of the bending resistance obtained from Ansys (M Ansys), are smaller the ones obtained from the analytic and simplified rules Mpl.T.Rd, and Mpl–solid. Where Mpl.T.Rd represent the bending resistance of Tee cellular beam determined from equation (48) and Mpl–solid present plastic resistance moment equation (25) in clause 2.6.

Figure 53 presents the temperature variation of bending resistance moment from Ansys (M Ansys) and plastic resistance moment Mpl –solid from Eurocode.

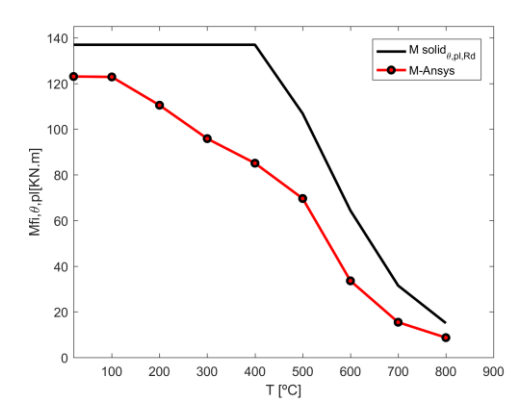


Case1: Section IPE220

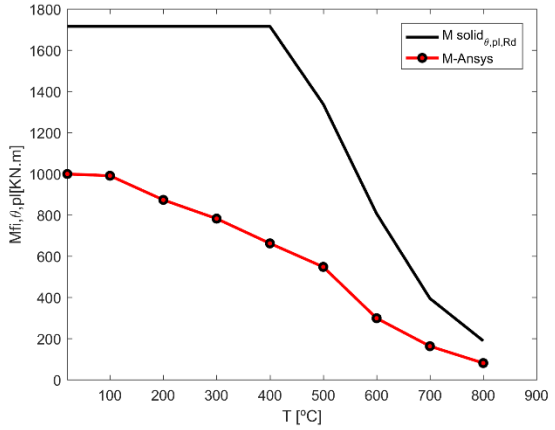


Case2: Section IPE600

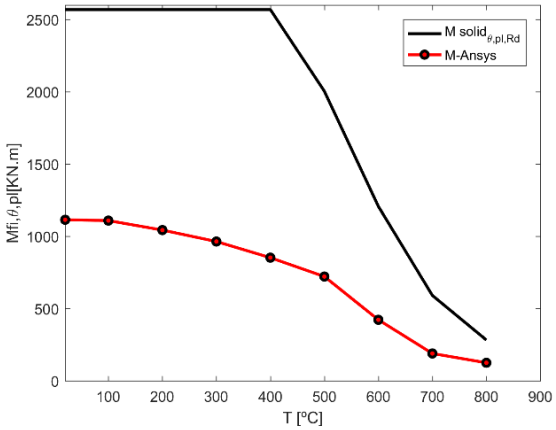


Case4: Section HE600A

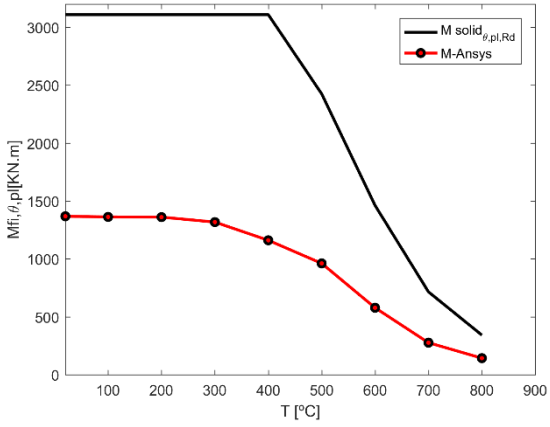


Case6: Section HE600B

Figure 53: Results for bending resistance of solid and cellular beams.

From the results shown in Figure 53, we can observe that for compact sections like the case 1 IPE 220, the results from Ansys are closer to plastic moment, representing almost 90% of the plastic moment resistant, reducing to 65% at 500°C. For more slender sections like HE 600A or HE600B the results from Ansys are much smaller than the plastic moment, reaching 40% 20°C and only 5% at 500°C.

Figure 54 presents the vertical displacement of different cellular beams in function of the applied load for the different temperature values analysed.

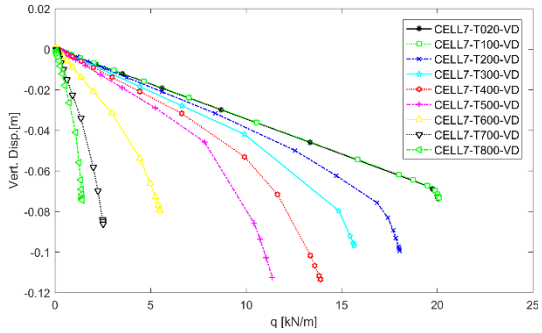


Case1: Section IPE220

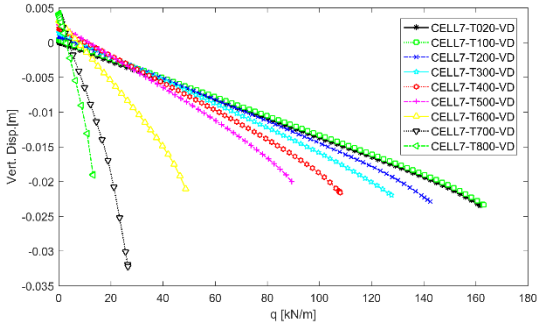


Case2: Section IPE600

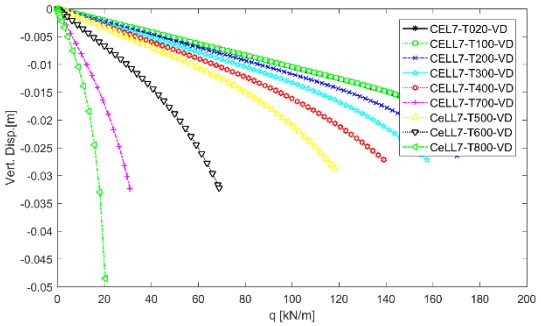


Case4: Section HE600A

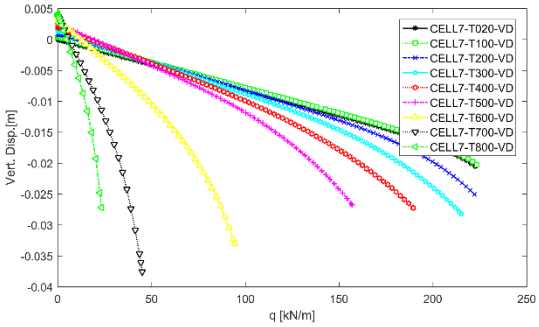


Case6: Section HE600B

Figure 54: Vertical displacement of cellular beams.

The failure of the perforated sections by bending corresponds to a global failure mode. It occurs in perforated sections subjected to pure bending, or when the effect of the shear force is negligible in comparison with that of the bending. In this case the failure occurs by appearance of two plastic hinges in the upper and lower sides of the perforated section as is shown in figure in Figure 55.

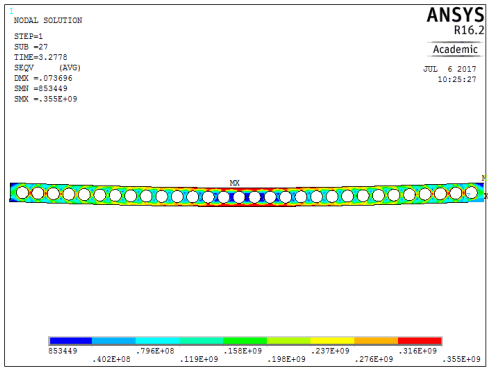


Von mises stress distribution IPE220 T=100°C

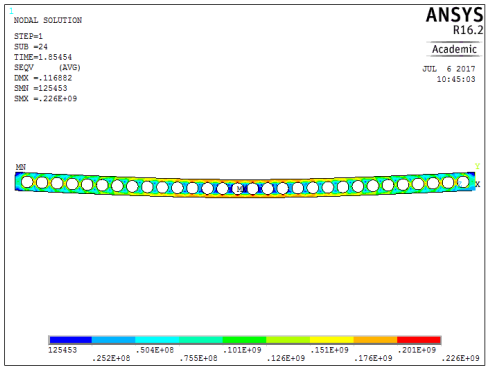


Von mises stress distribution IPE220 T=500°C

Figure 55: Failure mode due to plastification of Tee section-case 1 Section IPE220.

For cases 2 and 4 and 6, the failure mode was due to shear load in web post as we can see in Figure 56.

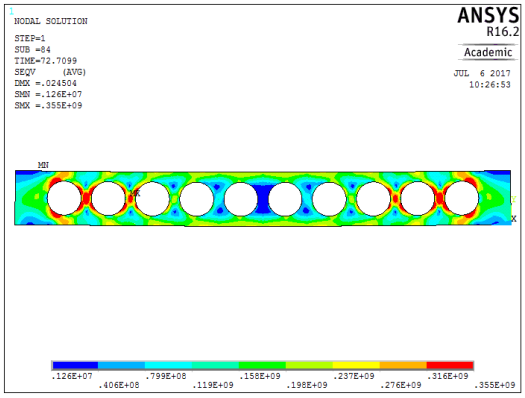


Von misses stress distribution at 500°C

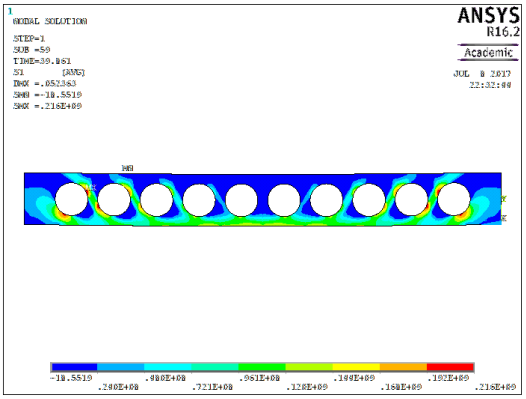


First stress distribution at 500°C

Case 2 section IPE600.

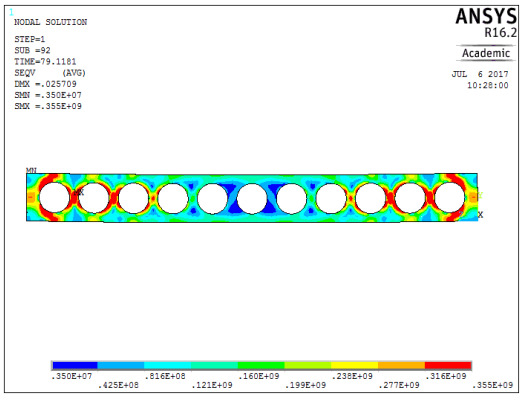


Von misses stress distribution at 500°C

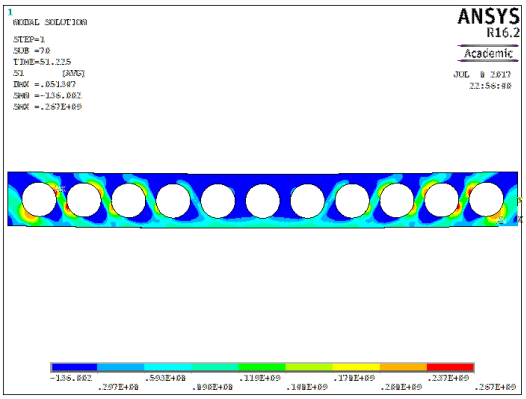


First stress distribution at 500°C

Case 4 section HE600A

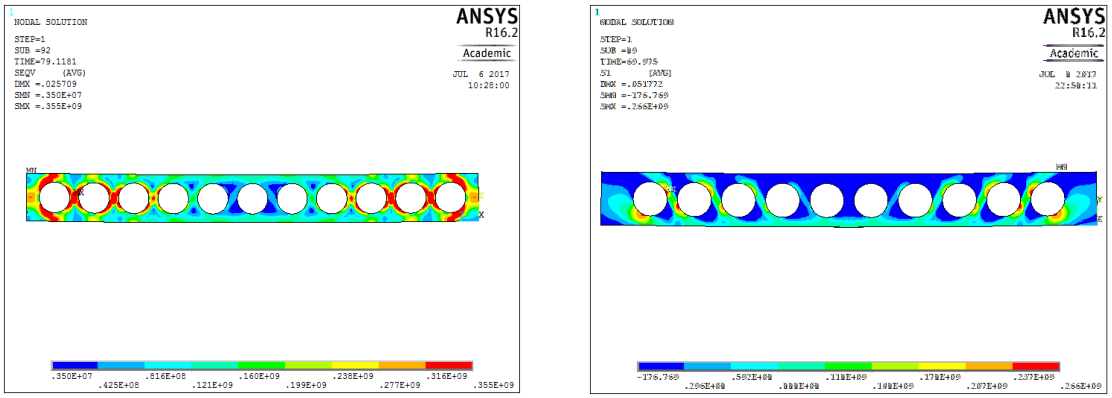


Von misses stress distribution at 500°C First stress distribution at 500°C

Case 6 section HE600B

Figure 56: Web post failure mode due to shear of different cellular beam.

### 4.3 Lateral torsional buckling numerical analysis of solid sections

Accidental fire conditions reduce the load bearing capacity and increase the risk of failure by lateral instability. Solid beams subjected to bending loads in the plane of their greatest flexural rigidity can buckle by combined twist and lateral bending called lateral-torsional buckling instability. Due to the low torsional and lateral flexural stiffness of slender beams. Their cross-section may rotate and deflect laterally. Although the solution to the problem of lateral-torsional buckling of steel beams at room temperature is well known. There is no solution for this problem at elevated temperature, [15].

A three-dimensional (3D) finite element model of ANSYS is simulated to determine the LTB resistance of solid beams. The Finite Element Method (FEM) is used to investigate the elastic stability of solid beams. However, a typical Eigenvalue analysis is also conducted to obtain the buckling load (Eigenvalue) and the corresponding buckling mode (Eigenvector). The elastic buckling analysis is performed on the geometry imperfection based on the first buckling mode resulting from the elastic eigenvalue analysis. In order to investigate influence of geometric imperfection on resistance moment, amplitudes of geometric imperfections L/1000, L/500 and L/250 have been considered and implemented in mid span.

The residual stresses adopted are constant across the thickness of the web and of the flanges. Triangular distribution with a maximum value of 0.3x $f_y$ MPa, for the S235 steel has been adopted.

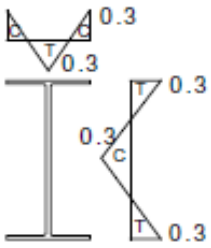


Figure 57: Residual stresses. C–compression; T–tension, [15].

### 4.3.1 Elastic buckling simulations of solid beams

The three-first lateral torsional global buckling modes with Eigen vector for temperatures from 20 [°C to 800°C, are illustrated in annex A1. Figure 58 presents the results of this simulation, considering the critical moment corresponding to three-first buckling modes in function of temperatures.

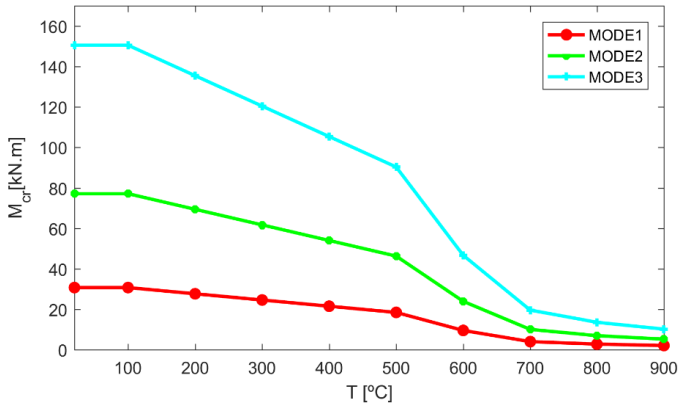


Figure 58: Critical moment plot for three-first global LTB modes.

Figure 59 presents the comparison between the critical moments determined from Eurocode given by equation (32) and critical moment obtained from result of numerical analysis. The results show that the critical moment from numerical analysis is higher than the ones determined from Eurocode.

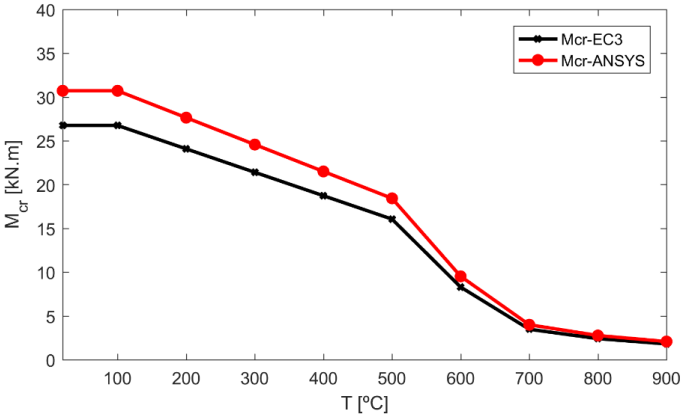


Figure 59: Comparison of critical moment between EC and numerical analysis.

Figure 60 presents the comparison of critical moment between EC and numerical analysis as function of non dimensional slenderness. Also in the figure it can be seen in comparison the elastic buckling curve from Euler. The influence is investigated in terms of the normalized critical moment ($M_{cr}/M_{pl}$), obtained from the FE model (Mcr-ANSYS), with plastic moment $M_{pl}$.

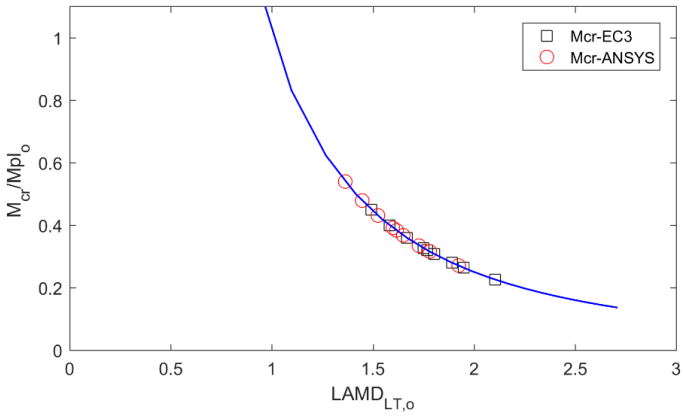


Figure 60: Comparison of critical moment between EC and numerical analysis.

4.3.1.1 Influence of the geometric imperfections

The result below present the influence of different amplitude of initial geometry imperfection on the resistance with increasing the temperature from 20°C to 800°C The results were compared to the simple model presented in Eurocode 3. Part 1-, [11], and to a new proposal, [15].

Figure 61 shows the results in function of temperatures and Figure 62 show the results in function of non-dimensional slenderness. The influence is investigated in terms of the normalized moment ($M/M_{fi.\theta.Rd}$). Where M represents the moment resistance obtained from the FE model, (MAnsys), and moment resistance determined from the Eurocode and normalized with plastic bending resistance. $M_{fi,\theta,Rd}$.

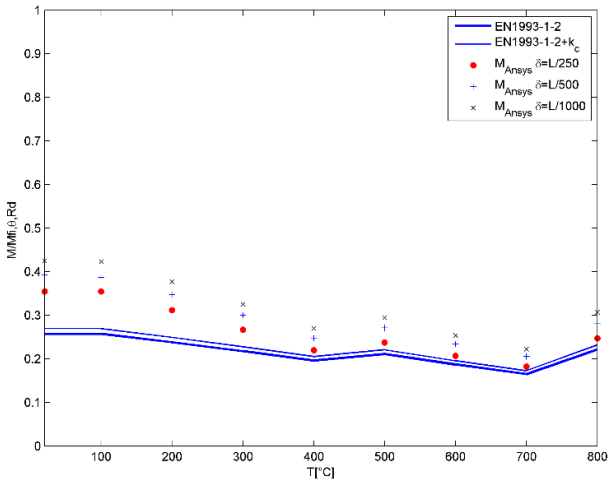


Figure 61: Influence of geometry imperfection in function of temperature.

From the result shown in the Figure 61 we notice that there is inverse relationship between the amplitude of imperfection and the resistance for different imperfections all results are above the both curve of Eurocode and new proposal that are presented in continue line. It is noted in Figure 61 that the resistance increase from 700°C to 800°C. This is due to ratio between yield strength reduction factor and elastic modulus reduction factor that affects the value of non-dimensional slenderness in fire condition equation (47).

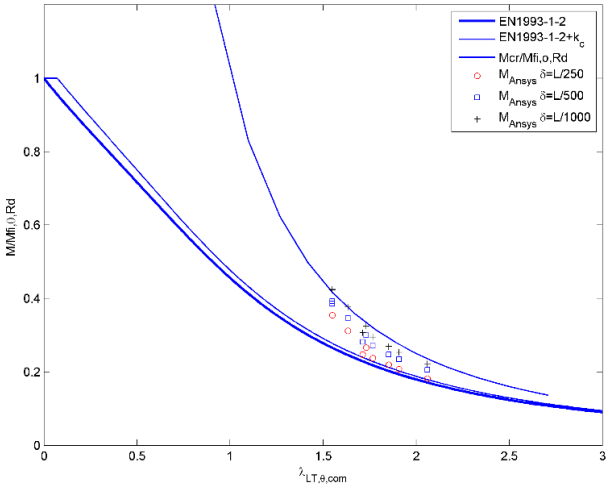


Figure 62: Influence of geometry imperfection in function of non-dimensional slenderness.

From the result shown in Figure 62 we can notice that curve for different geometry imperfections following the elastic curve and all of them are above the Eurocode curve from fire part 1-2. This results show that the numerical results are safe in comparison to the Eurocode results.

4.3.1.2 Influence of the residual stresses in the lateral torsional buckling the influence of temperature

The residual stresses in the lateral-torsional buckling of unrestrained steel I-beams has been numerically investigated, the results were compared to the simple model presented in Eurocode 3 Part 1-2 [11] and to a new proposal [15], that is being considered for approval in the Eurocode, [20]. The influence is investigated in terms of the normalized moment ($M/M_{fi.\theta.Rd}$). Where M represents the moment resistance obtained from the FE model, (MAnsys) and moment resistance determined from the Eurocode and normalized with plastic bending resistance, $M_{fi,\theta,Rd}$.

The load–vertical deflection curves and the load–lateral deflection curves are illustrated in Figure 63 and Figure 64, respectively.

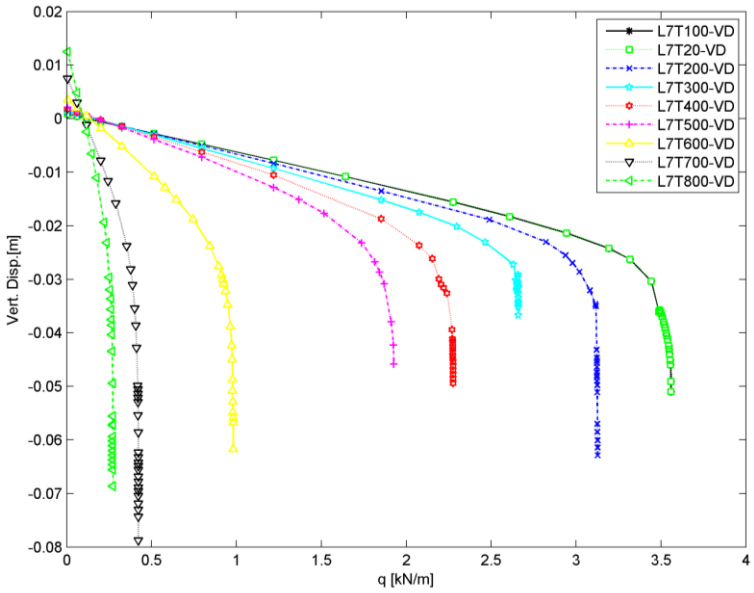


Figure 63: mid-span vertical displacement.

Mid-span vertical deflections are shown in Figure 64, as long as a mechanical load and residual stress was applied, the beams underwent vertical displacements increasing progressively and linearly until the temperature reached 500[°C], afterwards the deflections increased very quickly with the temperature, like is shown in the graph for temperature 700 [°C] and 800 [°C], in the beginning note a positive deflection and this due to applying first residual stress and constant temperature after that the load was applied.

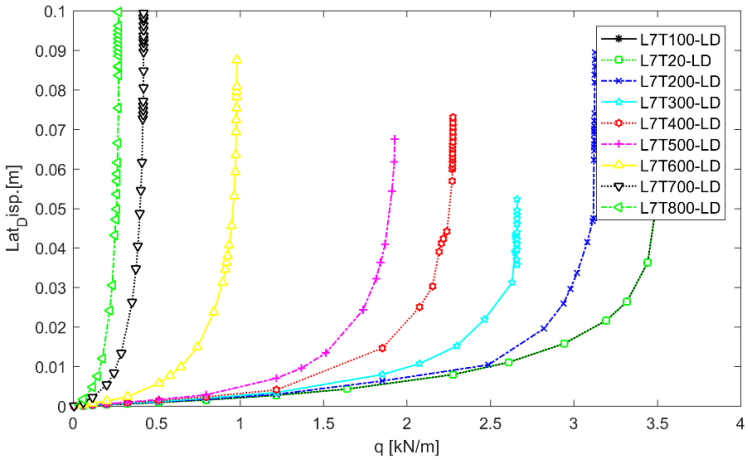


Figure 64: Mid-span lateral displacement.

As long as a mechanical load was applied during time. The beams underwent lateral displacements increasing progressively and linearly until the beam is exposed to constant temperature 500[°C]. The vertical displacement increased very quickly with the temperature rising.

The next figures show the influence of the residual stresses as the temperature increases from 20 to 800 [°C]. These figures clearly shows that the influence of the residual stresses decreases with increasing temperature. This is due to the stress–strain relationship at elevated temperature.

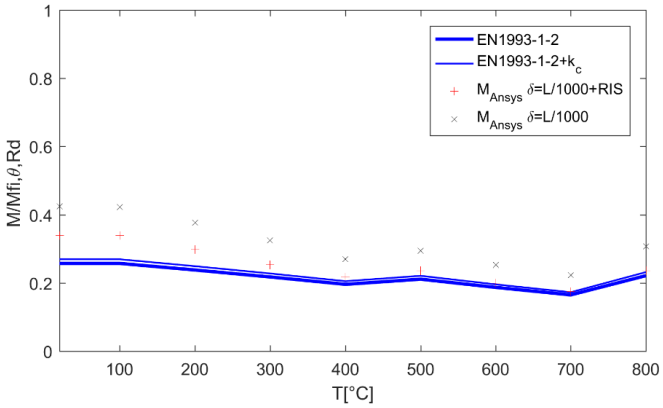


Figure 65: Influence of residual stress in function of temperature.

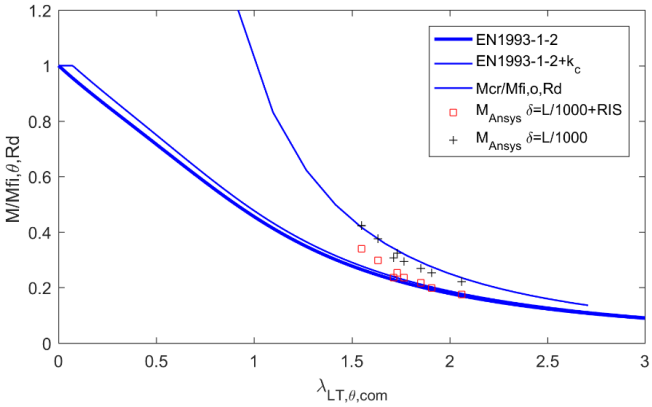


Figure 66: Influence of residual stress in function of non-dimensional slenderness.

4.3.1.3 The influence of the beam length for constant temperature.

Figure 67 present the distribution of residual stress in cross section in solid beam with 2m of length and Figure 68 present maximum vertical displacement for different beams length

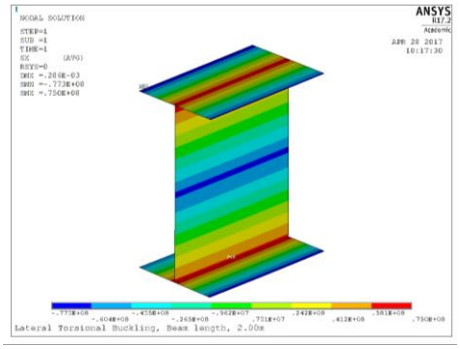


Figure 67: Distribution of residual stress in cross section.

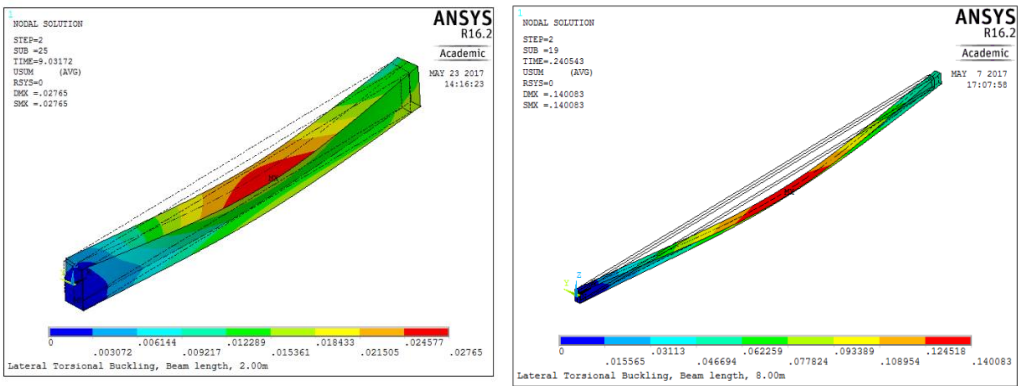


Figure 68: Maximum vertical displacement for different beams length.

The results of the influence of length beam at the resistance for room temperature in function of different lengths from 1 [m] to 8 [m], with increments of 1 [m], and non-dimensional slenderness shown in Figure 69Figure 70 respectively.

The length influence is investigated in terms of the normalized moment ($M/M_{fi.\theta.Rd}$) where M represents the moment resistance obtained from the FE model (MAnsys) and moment resistance determined from the Eurocode and normalized with plastic bending resistance. $M_{,Rd}$ .

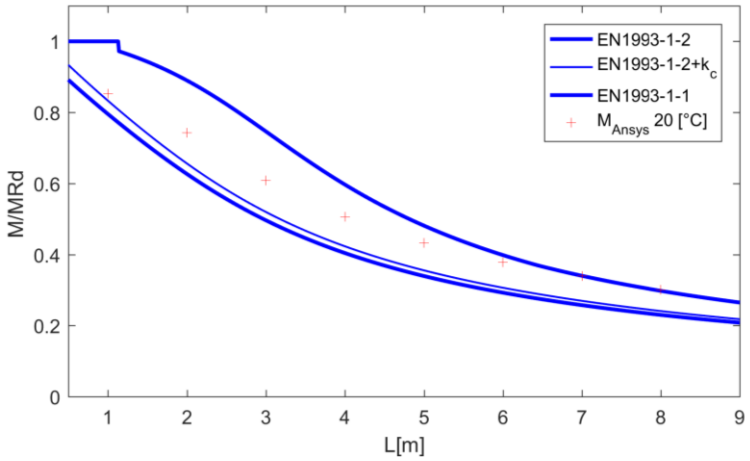


Figure 69: Influence of the beam length at room temperature.

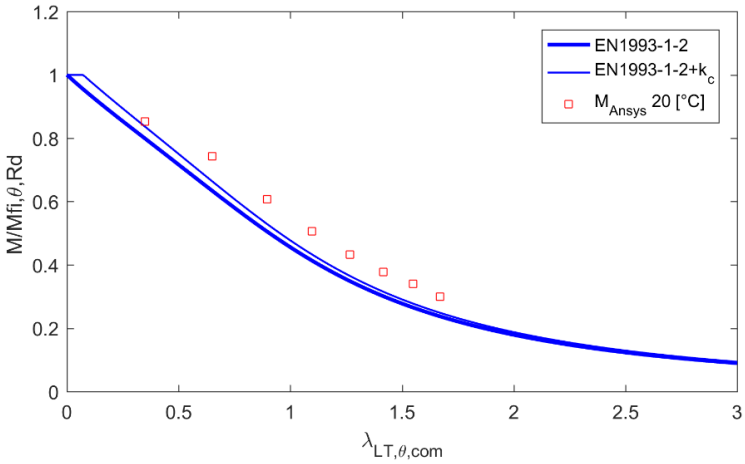


Figure 70: Influence of the beam length at room temperature in function on non-dimensional slenderness.

From results shown above for room temperature and all lengths the results are above design buckling curves from EC3, [11] and the new proposal, [15], and we could see that with increasing the beam length, the moment resistance from Ansys be more close to elastic curve so the safety is reserved.

To show the influence of beam length at elevated temperatures, a set of numerical simulations was done for all the beam lengths at different temperatures: temperature equal

to 400°C, 500°C and 600°C. The results are represented in Figure 71, Figure 73, Figure 75 in function of the beam length and in the Figure 72, Figure 74 and Figure 76 in function of non-dimensional slenderness. The values are normalized with respect to the cross section plastic resistant for the respective temperature, $M_{fi,\theta,Rd}$.

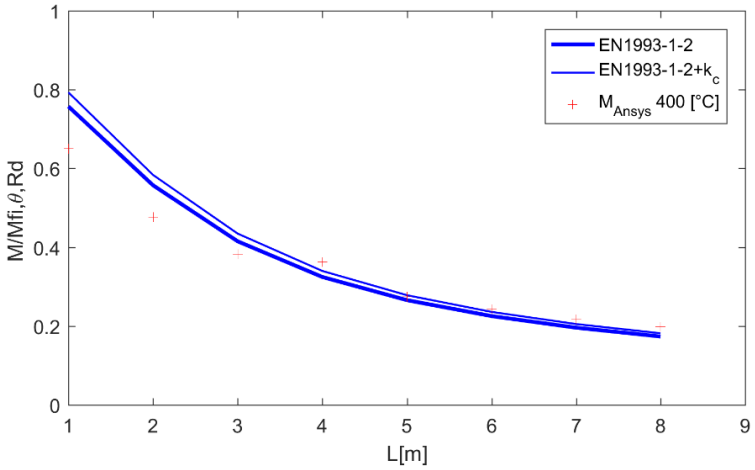


Figure 71: Influence of the beam length in 400°C.

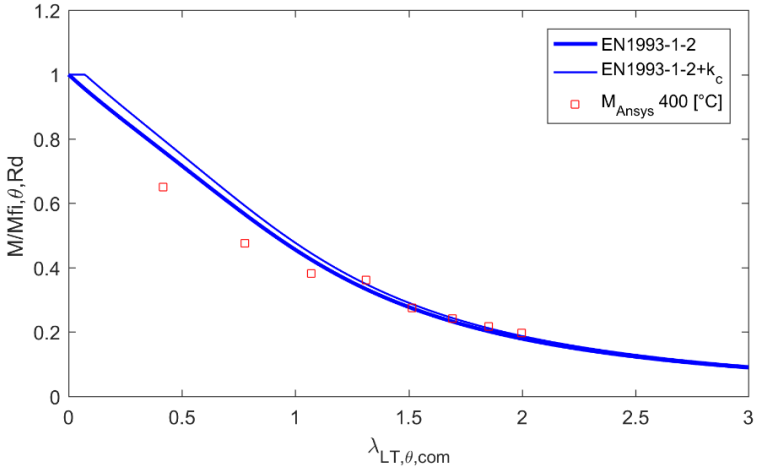


Figure 72: Influence of the beam length in 400°C in function of non-dimensional slenderness.

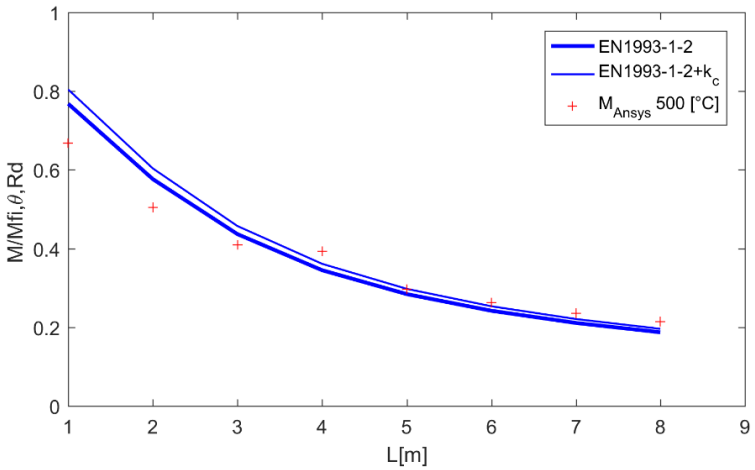


Figure 73: Influence of the beam length in 500°C.

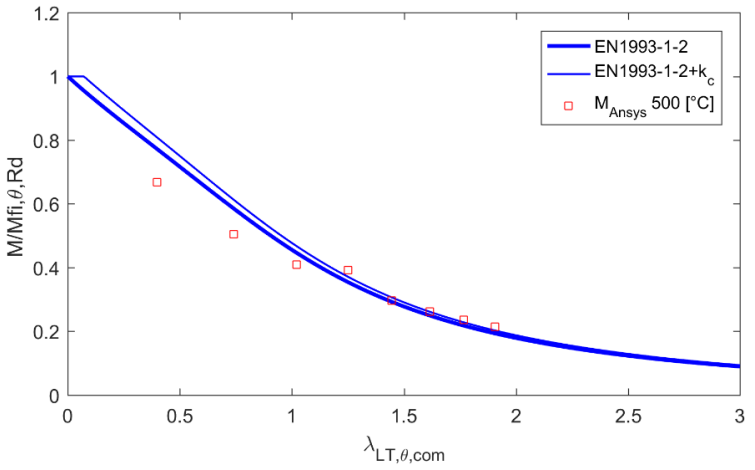


Figure 74: influence of the beam length in 500°C in function of non-dimensional slenderness.

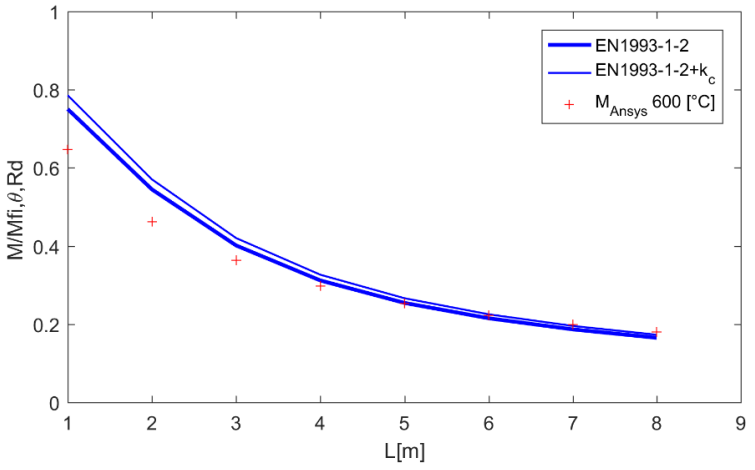


Figure 75: influence of the beam length in 600°C.

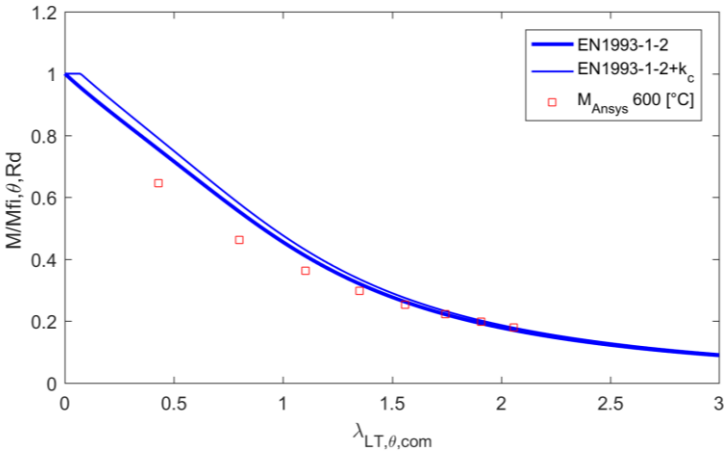


Figure 76: influence of the beam length in 600°C in function of non-dimensional slenderness.

From the results above, for temperatures 400°C and 500°C and 600°C is notice that the resistance for beams with length 1m to 4m. the resistance curve from Ansys are below both Eurocode Part 1-2 curve [11], and to a new proposal curve [15]. This is due to shear load effect for small length beams close to the end supports. For more slender beams, 5m to 8m, the results are following both Eurocode curves and the collapse mode is mainly due to bending.

## 4.4 Lateral torsional buckling numerical analysis of cellular sections

Either to investigate instabilities perturbed structural geometry or imperfections in the cellular beams are required a small initial imperfection is imposed on the non-deformed cellular beams. This imperfection represents effects from cutting and fabrication as well as residual stresses in the cellular beams. Generally, an imperfection pattern is selected based on the first mode from elastic eigenvalue analysis. Therefore, before investigating the in-elastic LTB behaviour an eigenvalue analysis was conducted to obtain the first buckling mode. The first elastic buckling mode should generally correspond to lateral torsional buckling. In this study the imperfection amplitude of L/1000 was imposed on the initial geometry and was implemented in mid span, with L being the span length of the beam, [21].

Figure 77 show both the load–vertical deflection curves and the load–lateral deflection curves of different cross section of cellular beams.

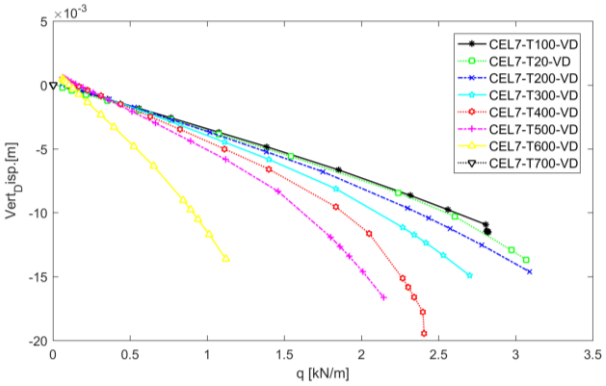


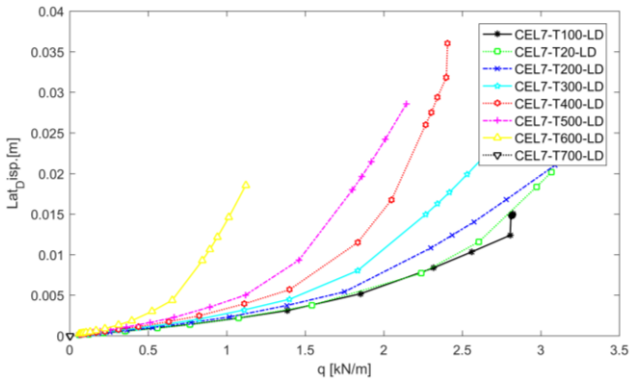


Case 1 IPE220

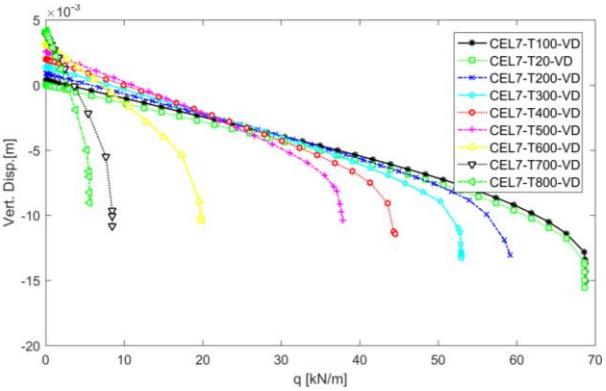


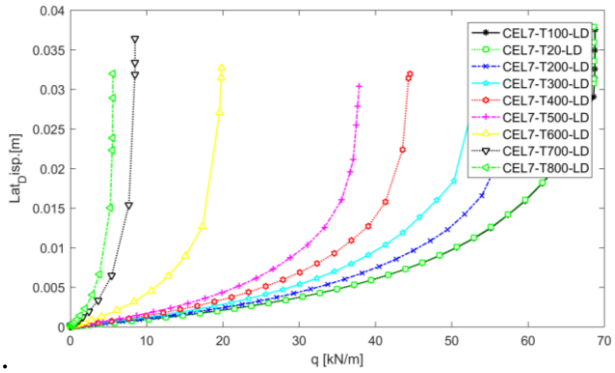


Case 2 IPE600

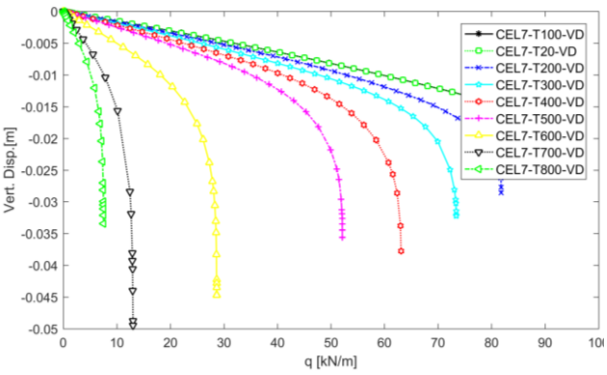


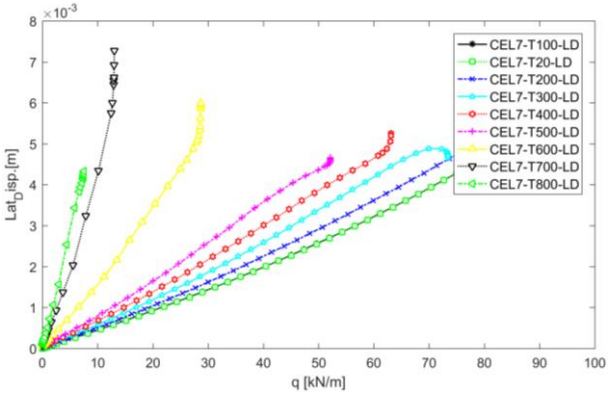


Case 4 HE600A

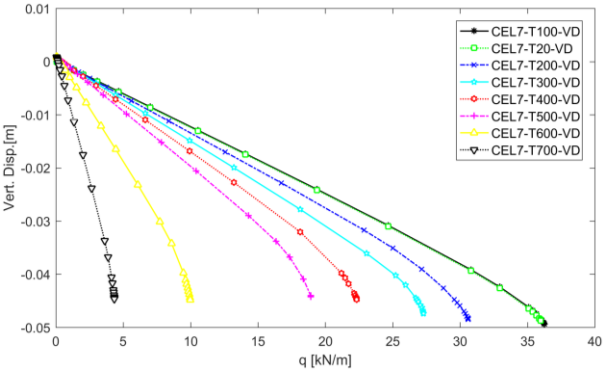


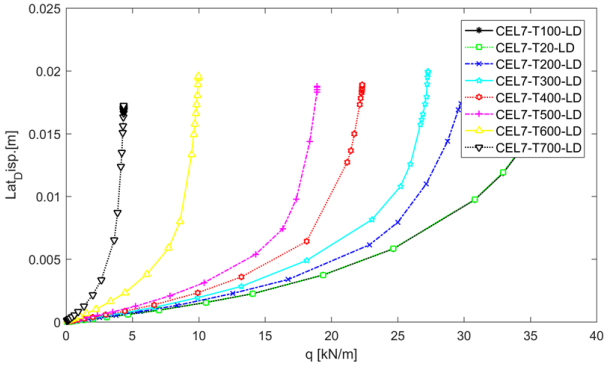


Case 5 HE220B

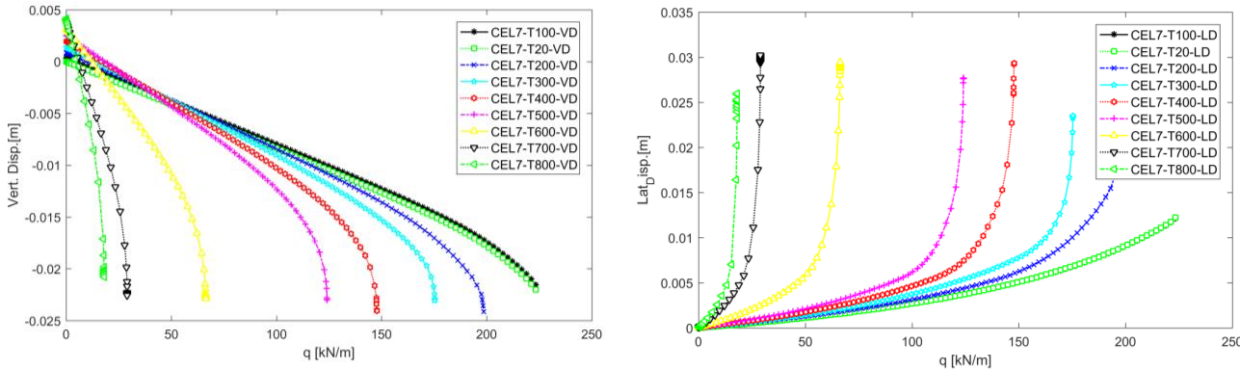


Case 6 HE600B

Figure 77: Vertical and lateral displacement of different cellular beams section.

Numerical results of LTB resistance for different cellular beams cross section have been compared with the simple formulas from Eurocode 3 Part 1.2 [11], and the new proposal, [15]. The comparisons are depicted in terms of the normalized moment ($M/M_{fi.\theta.Rd}$). Where M represents the moment resistance obtained from the FE model, (MAnsys) and moment resistance determined from the Eurocode and normalized with plastic bending resistance. $M_{fi,\theta,Rd}$ . LTB resistance ratio of the computed LTB resistance to the FE LTB resistance, with varying temperature. The results of these comparisons are shown, in Figure 78.

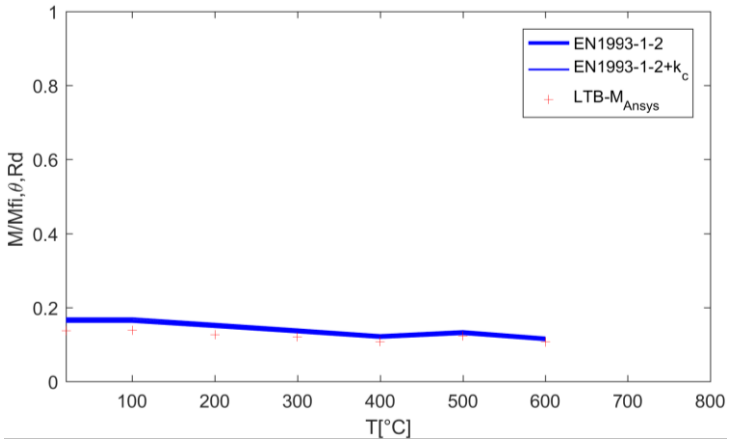


Case 1 section IPE 220

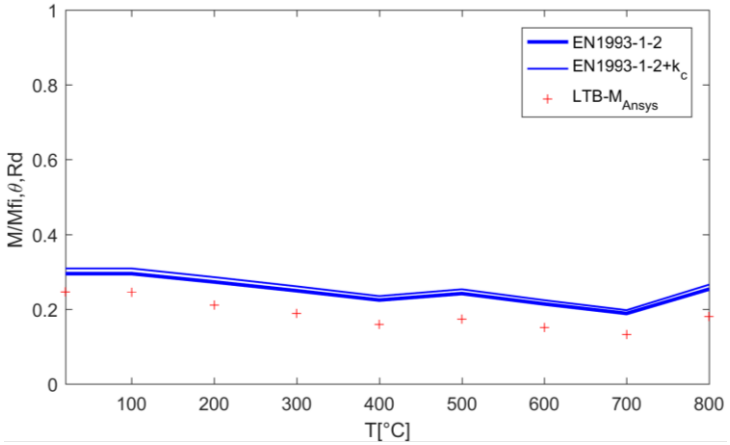


Case 2 section IPE 600

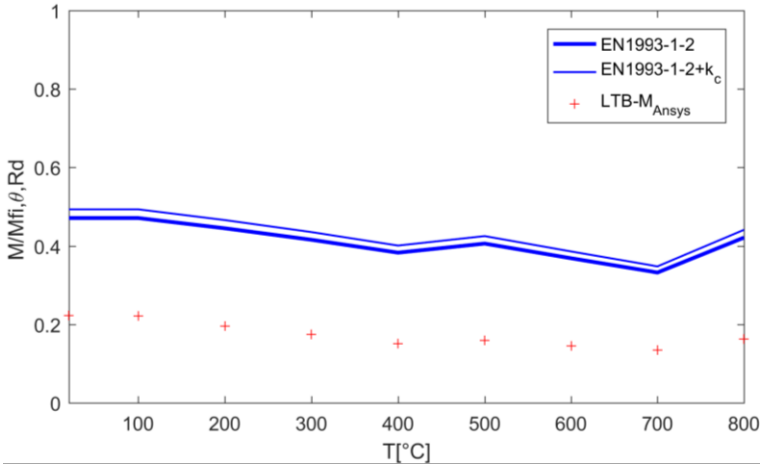


Case 4 section HE600A

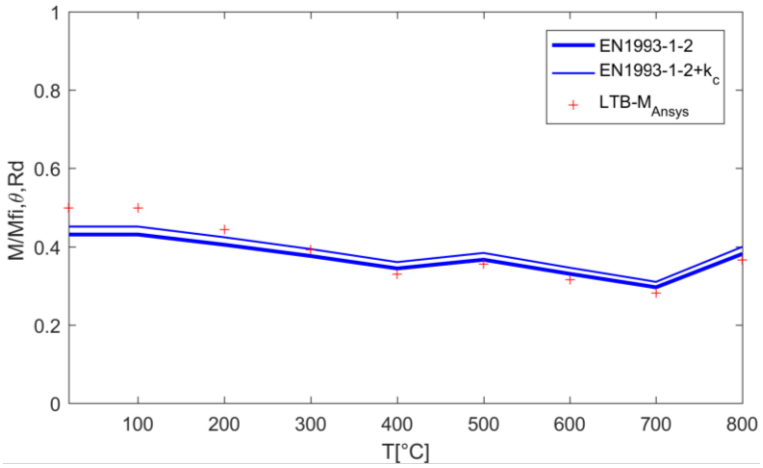


Case 6 HE600B section

Figure 78: Lateral buckling resistance for different cellular beams cross section in function of different temperatures.

For IPE 220 cross section the numerical results of LTB resistance is almost in the same line with Eurocode LTB resistance. For IPE600 all numerical results are below about 5% to Eurocode curves. For HE600A the numerical results below about 25% to Eurocode curves. The HE600B cross section the LTB resistance for temperature from 20°C up to 200[°C], are higher than Eurocode curves and for temperatures from 300[°C] to 800[°C] the numerical results following Eurocode curves.

# CHAPTER.5 CONCLUSION AND FUTURE WORK

## 5.1 Main conclusions

The thesis investigates the thermal and structural behaviour of steel solid and open cross-section beams under fires condition using finite elements simulations.

The study presents the influence of temperature and the shape factor for different cross section according to Eurocode simplified method.

Under elevated temperatures, the finite element thermal analysis shows that web post temperature is higher than in the solid beam and that it gets extra heat from the holes edge.

The simulations with ANSYS thermal finite element models have produced good predictions for temperature evolution with small discrepancies acceptable for comparison with tests.

The thermo-mechanical behaviour of solid beam were investigated using FE model takes into account both geometric and material non linearity to simulate large displacement and material behaviour with Uniform distributed load applied on nodes, varying with time ($q = 100t$) with constant temperature distribution in all elements.

The effect of initial geometry imperfection and residual stress are include on LTB stability, were the resistance is more influence by geometric imperfection than the residual stress, where the effect of residual stress disappear in height temperature

The increase of the temperature and the length of beam strongly affect the lateral torsional buckling (LTB) stability. The analysis shows that the deflection increases rapidly as the load carrying capacity decreases. For shorter spans, the resistance is low because of the shear force and with increasing the length, the effect of shear disappears and the resistance increases. Thermochemical analysis for cellular beam investigated locale failure modes due to bending and to shear for web post. Different cross section are analysed with increasing temperature and results show the influence on the resistance of cellular beam. Imperfections cause the steel members to have additional residual stress change patterns. This would contribute to the failure modes like lateral torsional buckling.

## 5.2 Future lines of investigation

Regarding the continuation of this work it will be interesting to continue this research about the thermomechanical behaviour of protected cellular beams, with new numerical methods and perform a set of experimental tests to calibrate the numerical model.

Study of different values, performing a parameter analysis, of web post widths and holes diameters.

Use the numerical models to perform different transient thermal analysis to determine the fire resistance time and collapse temperatures of cellular beams.

# REFRENCES


1. *The intelligent solution for long spans ArcelorMittal_ACB Cellular ACB* A.E.-L.P.S.a.M. Bars, Editor. 1996.
2. Krzysztof KUCHTA1, M.M., *Failure modes determining the resistance and the stability of steel cellular beams.* Journal of civil engineering, environment and architecturejournal of civil engineering, environment and architecture, 2015.
3. Chung, K.F., T.C.H. Liu, and A.C.H. Ko, *Investigation on Vierendeel mechanism in steel beams with circular web openings.* Journal of Constructional Steel Research, 2001. **57**(5): p. 467-490.
4. Nadjai, A., et al., *Performance of cellular composite floor beams at elevated temperatures.* Fire Safety Journal, 2007. **42**(6–7): p. 489-497.
5. Bihina, G., Zhao, B., & Bouchaïr, A. (2013). *Behaviour of composite steel–concrete cellular beams in fire*. *Engineering Structures*, *56*, 2217-2228.
6. Wang, P., X. Wang, and M. Liu, *Practical method for calculating the buckling temperature of the web-post in a cellular steel beam in fire.* Thin-Walled Structures, 2014. **85**: p. 441-455.
7. WANG, Peijun, MA, Ning, et WANG, Xudong. *Numerical studies on large deflection behaviors of restrained castellated steel beams in a fire*. *Journal of Constructional Steel Research*, 2014, vol. 100, p. 136-145.
8. Nadjai, A., et al., *Performance of unprotected and protected cellular beams in fire conditions.* Construction and Building Materials, 2016. **105**: p. 579-588.
9. Jean Marc Franssen, V.K., Raul Zaharia, *Designing Steel Structures for Fire Safety*, ed. C. Press. May 6, 2009. 160.
10. BAILEY, Colin G., NEWMAN, Gerald M., et SIMMS, W. Ian. *Design of steel framed buildings without applied fire protection*. Ascot, UK Steel Construction Institute, 1999.
11. CEN - EN 1993-1-2; "Eurocode 3: Design of steel structures - Part 1-2: General rules - Structural fire design", *European standards*; Brussels, April 2005.
12. *CEN - EN 1991-1-2; "Eurocode 1: Actions on structures - Part 1-2: General actions on structures exposed to fire"*. 2009.
13. CEN - EN 1993-1-1; "Eurocode 3: Design of steel structures - Part 1-1: General rules Rules for buildings. European standards; Brussels, 2005.

14. LAWSON, R. M. et HICKS, S. J. *Design of composite beams with large web openings: In accordance with Eurocodes and the UK National Annexes*. Steel Construction Institute, 2011.
15. Vila Real, P.M.M., P.A.G. Piloto, and J.M. Franssen, *A new proposal of a simple model for the lateral-torsional buckling of unrestrained steel I-beams in case of fire: experimental and numerical validation.* Journal of Constructional Steel Research, 2003. **59**(2): p. 179-199.
16. Brahim Lamri, Fire resistance of protected and unprotected cellular beams, Mestrado em Engenharia da Construção, Instituto Politécnico de Bragança, 19 de Julho 2016. Orientação: Luis Mesquita, Abdelhak KADA. http://hdl.handle.net/10198/13596.
17. *Test methods for determining the contribution to the fire resistance of structural members — Part 9: Applied fire protection systems to steel beams with web openings. (EN 13381-9:2012).* 2012.
18. A. KADA, B.L., N. BENLAKEHAL, L.M.R. MESQUITA, A. BOUCHAIR. *Finite element investigation on the behaviour of structural steel beams subjected to standard & parametric fire*. Revue « Nature & Technologie ». C- Sciences de l'Environnement, n° 13/ Juin 2015. Pages 28à 33 14 Mai 2015.
19. A. Kada1, B.L., L. Mesquita M.R.and A. Bouchair, *finite element analysis of steel beams with web apertures under fire condition.* asian journal of civil engineering (BHRC) VOL. 17, NO. 8(2016) PAGES 1035-1054, 27 May 2016.
20. Vila Real, P.M.M., et al., *The effect of residual stresses in the lateral-torsional buckling of steel I-beams at elevated temperature.* Journal of Constructional Steel Research, 2004. **60**(3–5): p. 783-793.
21. Panedpojaman, P., W. Sae-Long, and T. Chub-uppakarn, *Cellular beam design for resistance to inelastic lateral-torsional buckling.* Thin-Walled Structures, 2016. **99**: p. 182-194.

# ANNEX

## A1. Elastic Lateral torsional buckling modes

| Temp [°C] | Mode1 | Mode2 | Mode3 |
|---|---|---|---|
| 20 | 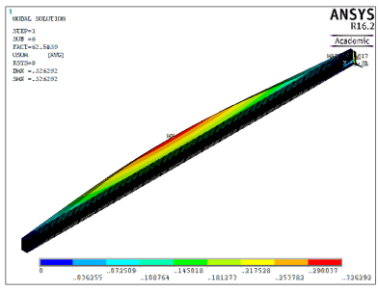 $Q_{cr}$= 62.584 | 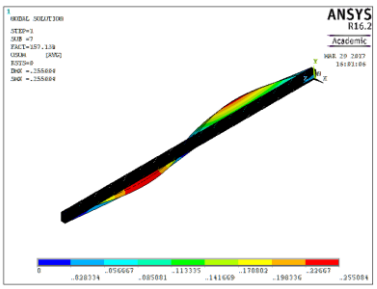 $Q_{cr}$=157.14 | 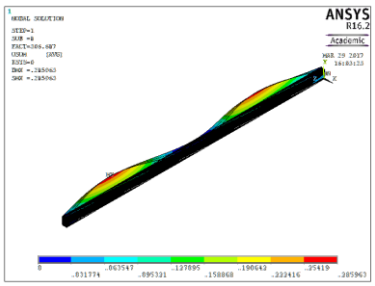 $Q_{cr}$=306.69 |
| 100 | 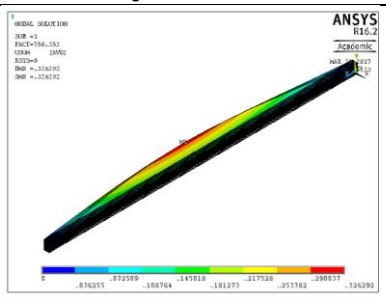 $Q_{cr}$=62.584 | 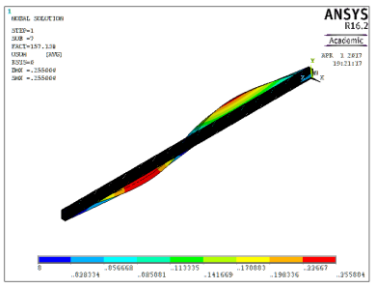 $Q_{cr}$=157.14 | 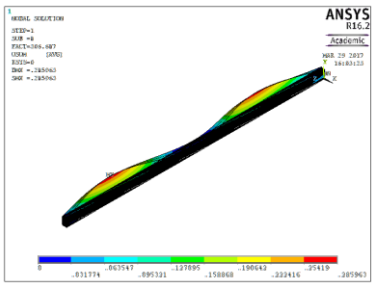 $Q_{cr}$=306.69 |
| 200 | 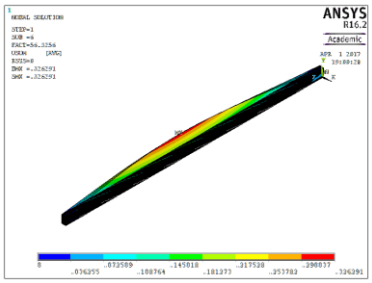 $Q_{cr}$=56.326 | 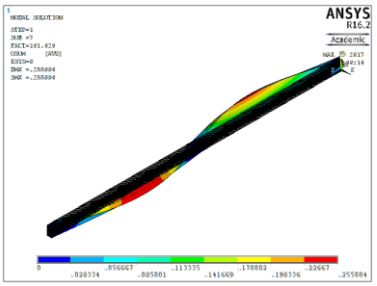 $Q_{cr}$=141.42 | 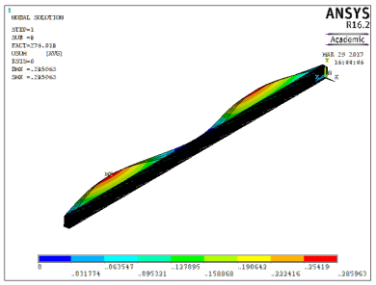 $Q_{cr}$=276.02 |
| 300 | 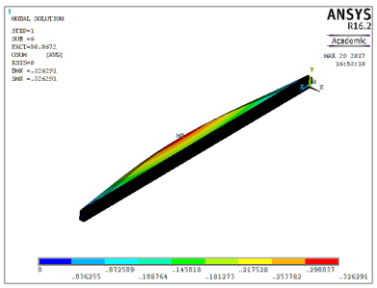 $Q_{cr}$=50.067 | 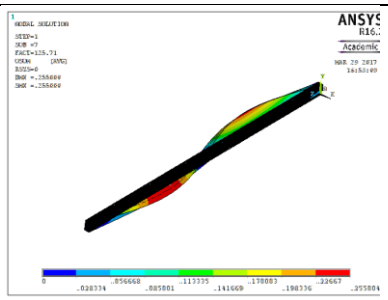 $Q_{cr}$=125.71 | 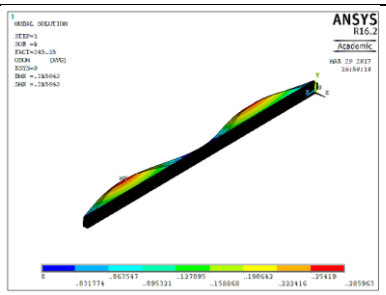 $Q_{cr}$=245.35 |

| | | | |
|---|---|---|---|
| 400 | 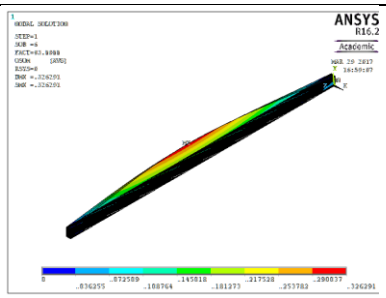 | 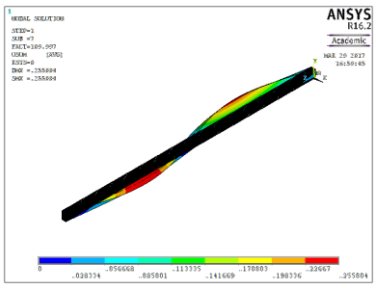 | 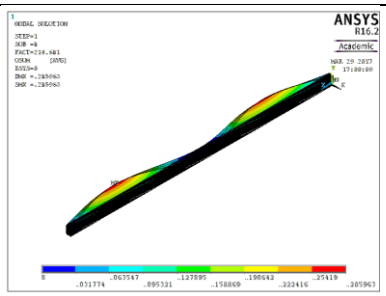 |
| | $Q_{cr}$=43.809 | $Q_{cr}$=110 | $Q_{cr}$=214.68 |
| 500 | 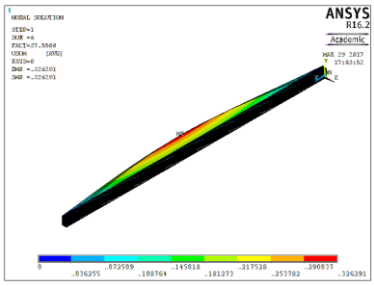 | 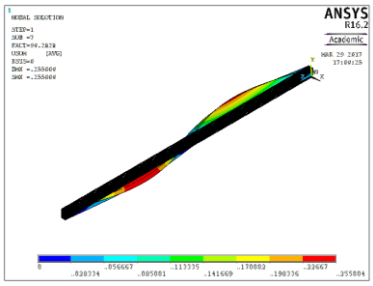 | 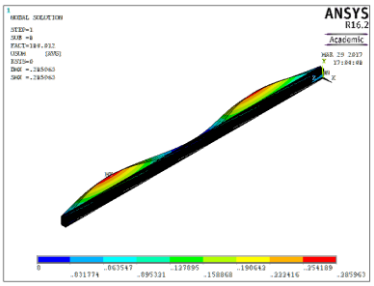 |
| | $Q_{cr}$=37.55 | $Q_{cr}$=94.283 | $Q_{cr}$=184.01 |
| 600 | 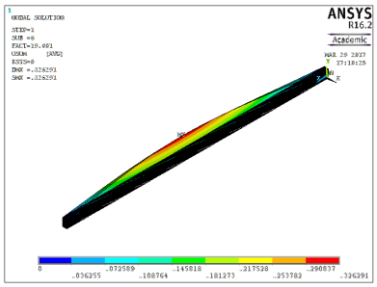 | 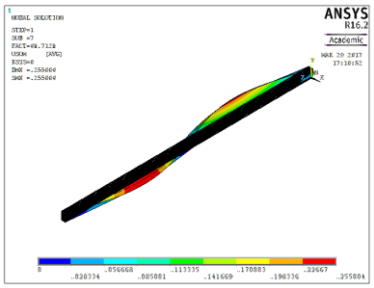 | 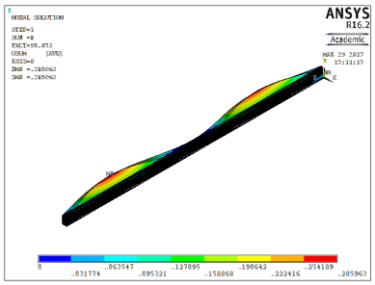 |
| | $Q_{cr}$=19.401 | $Q_{cr}$=48.713 | $Q_{cr}$=95.073 |
| 700 | 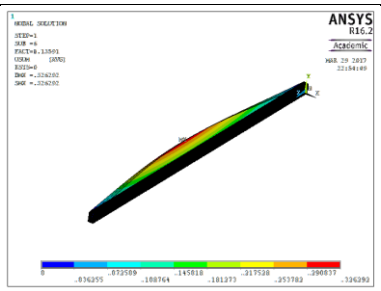 | 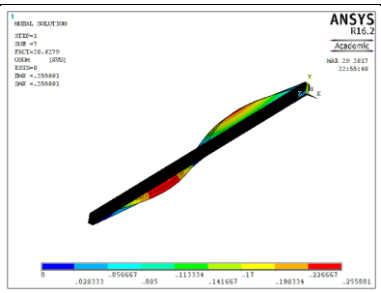 | 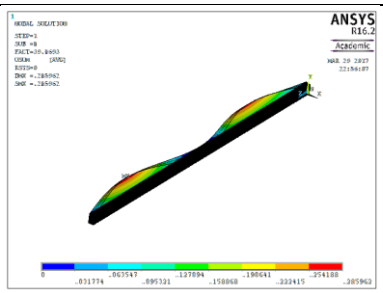 |
| | $Q_{cr}$=8.1359 | $Q_{cr}$=20.428 | $Q_{cr}$=39.869 |
| 800 | 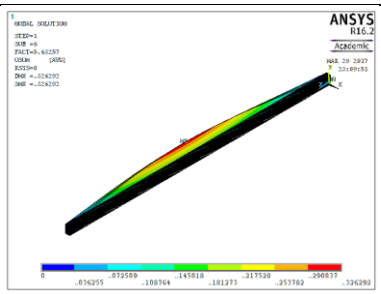 | 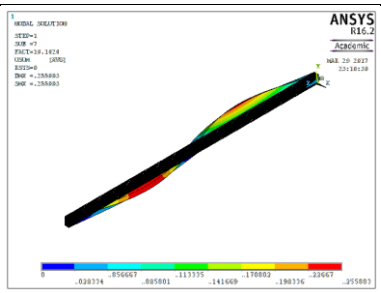 | 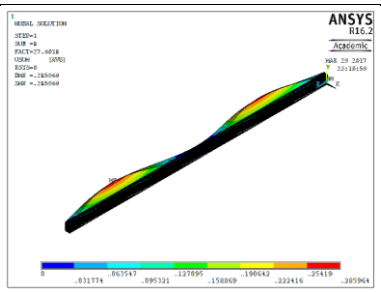 |
| | $Q_{cr}$=5.6326 | $Q_{cr}$=14.142 | $Q_{cr}$=27.602 |

## A2. Von misses stress distribution of different section of cellular beams.

T20

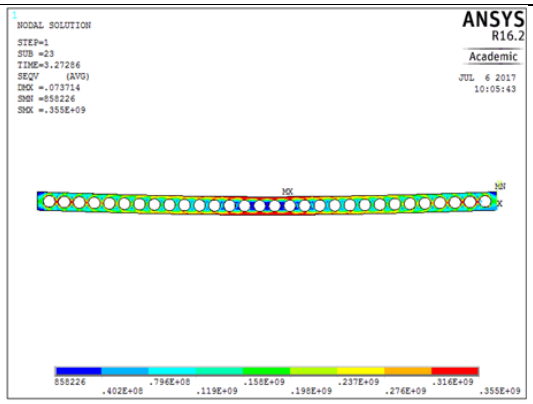


Case1

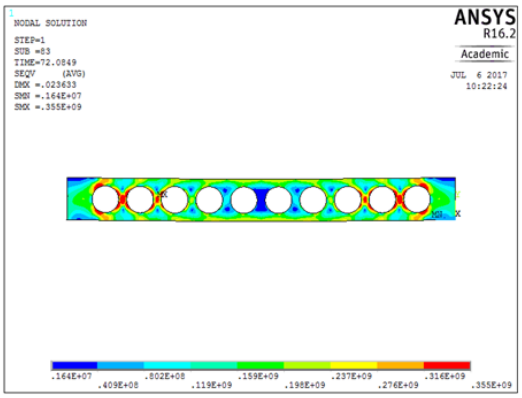


Case2

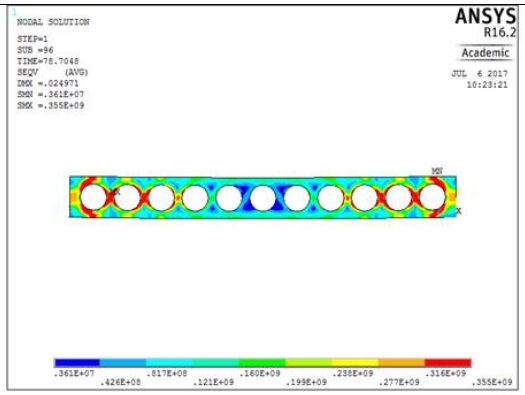


Case4

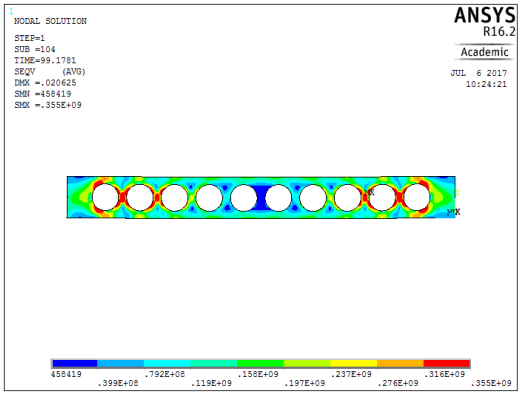


Case6

T100°C

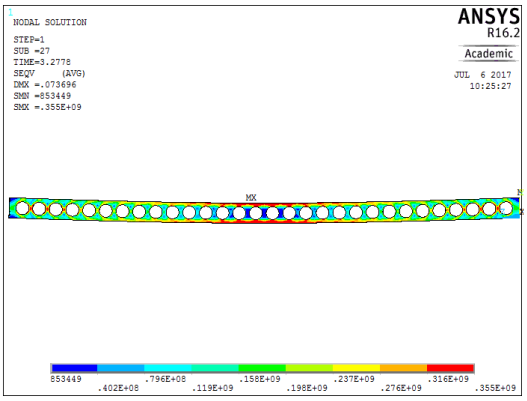


Case1

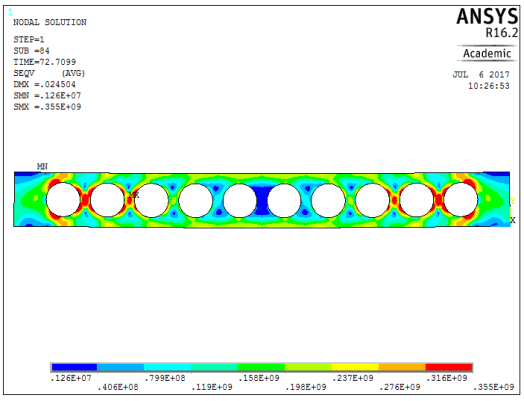


Case2

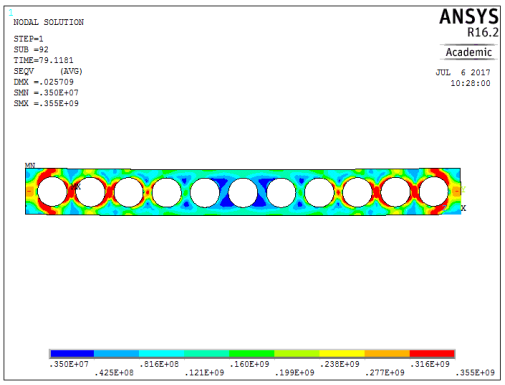


Case4

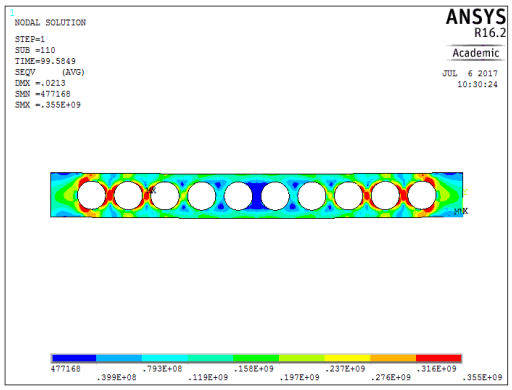


Case6

T200

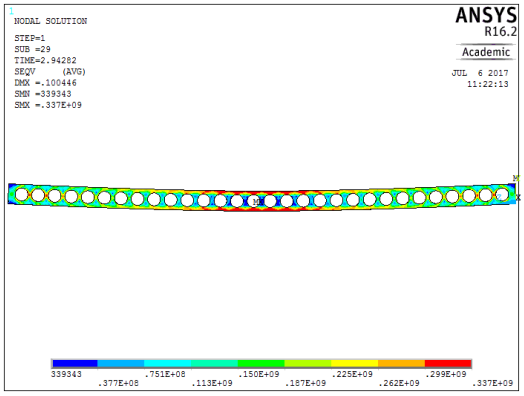


Case1

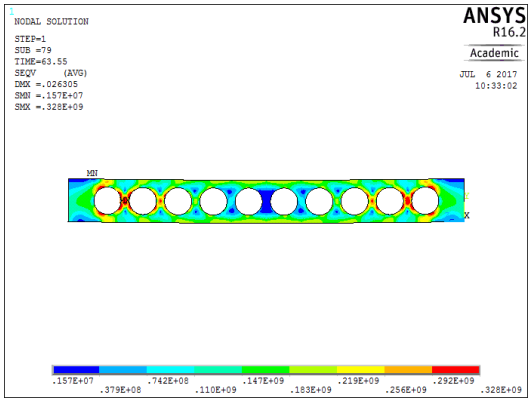


Case2

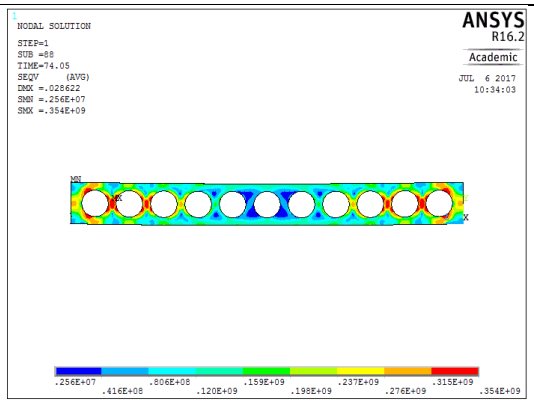


Case4

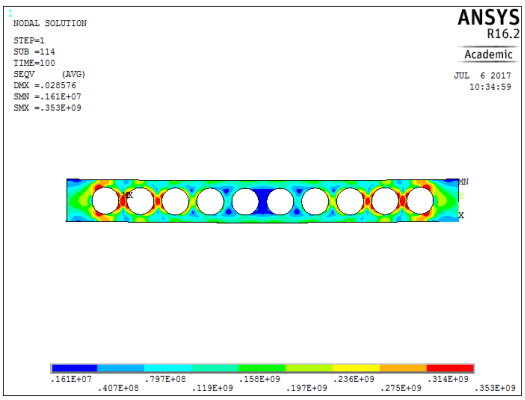


Case6

T300

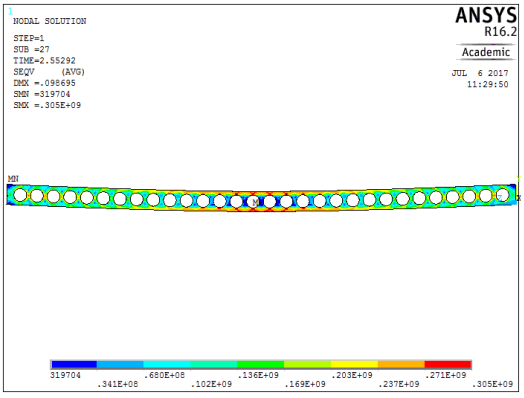


Case1

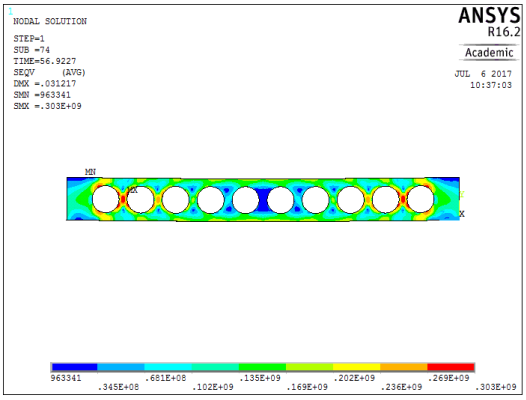


Case2

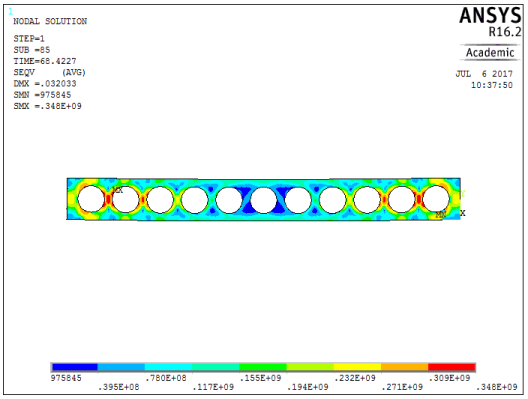


Case4

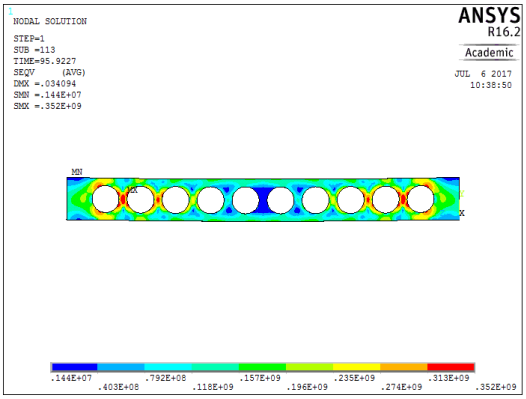


Case6

T400

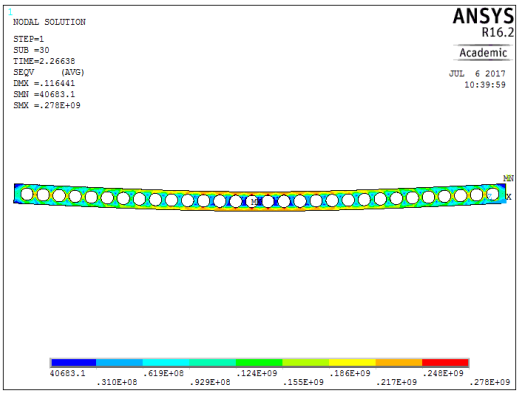


Case1

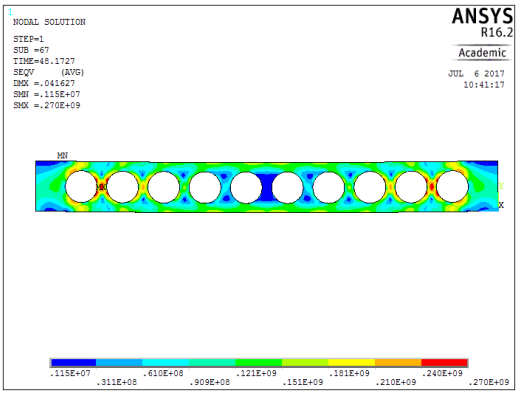


Case2

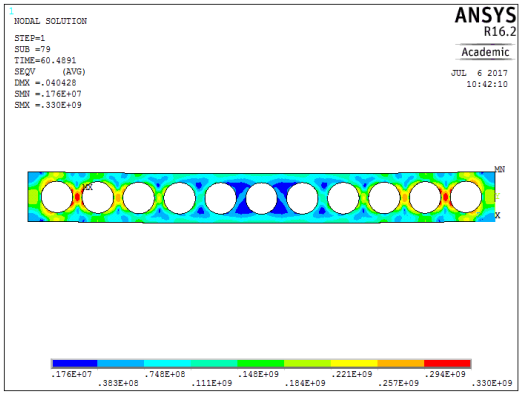


Case4

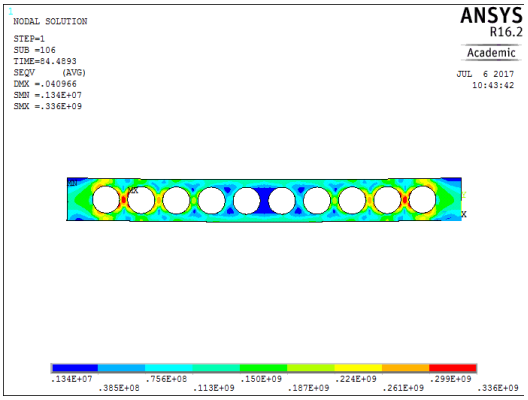


Case6

T500°C

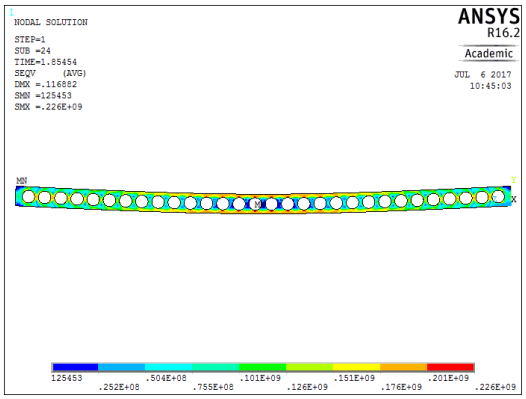


Case1

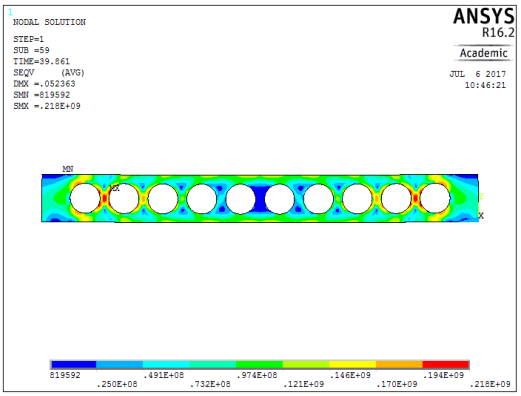


Case2

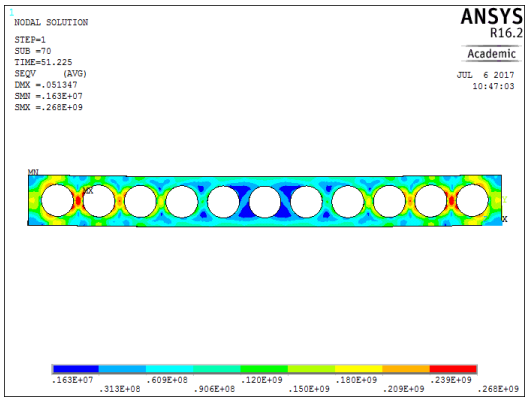


Case4

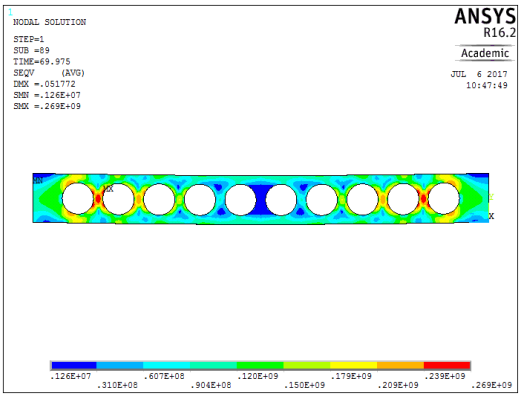


Case6

T600

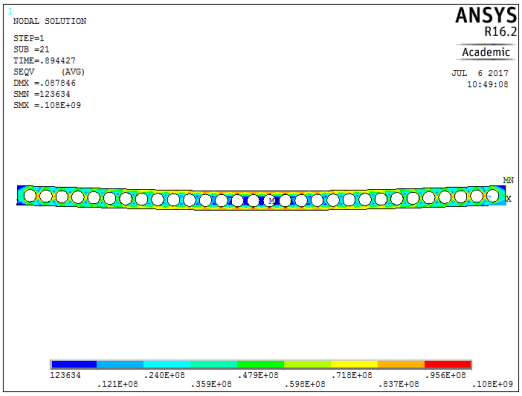


Case1

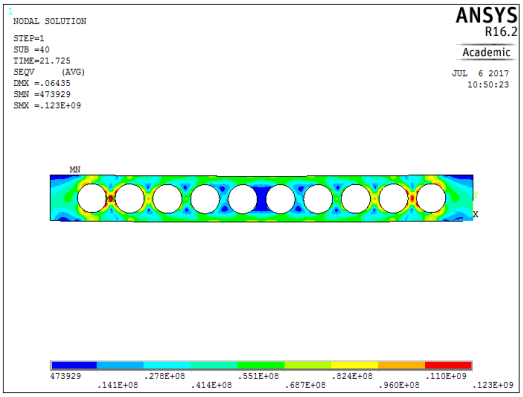


Case2

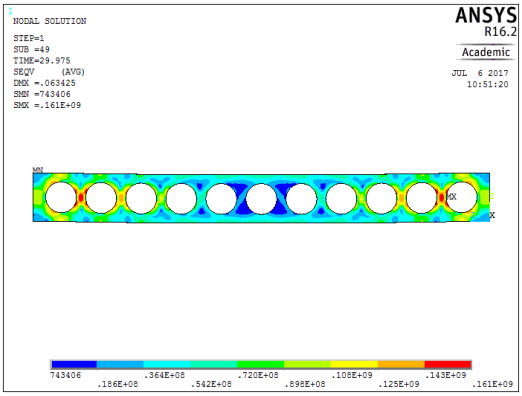


Case4

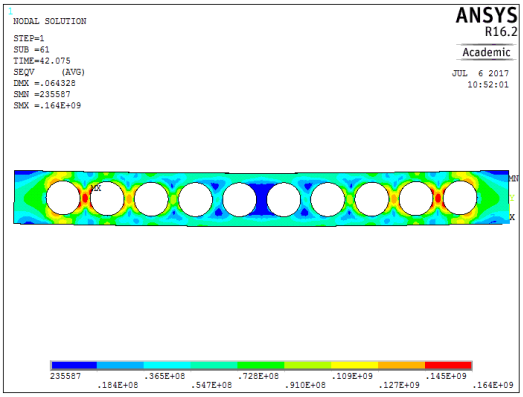


Case6

T700

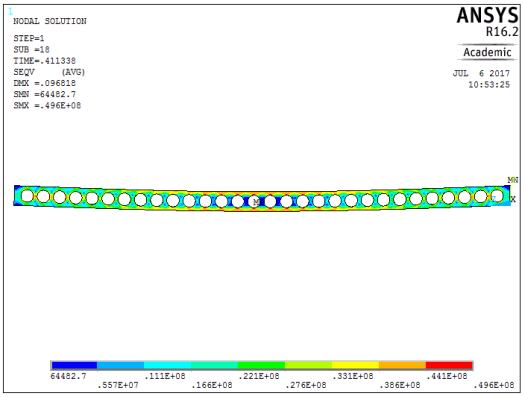


Case1

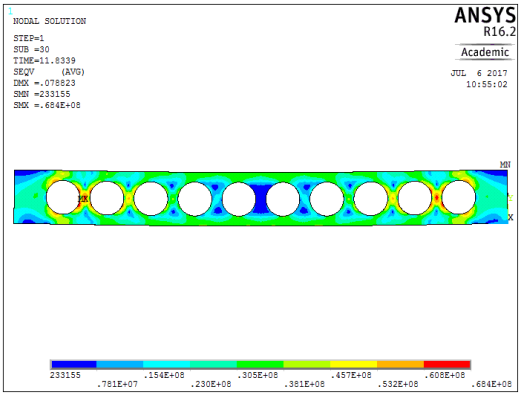


Case2

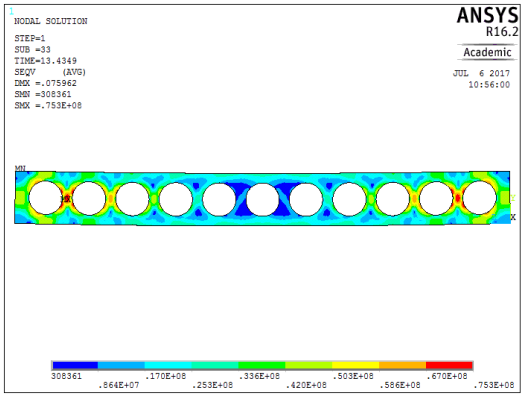


Case4

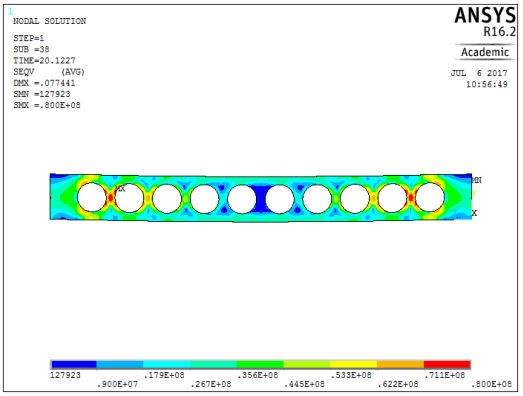


Case6

T800

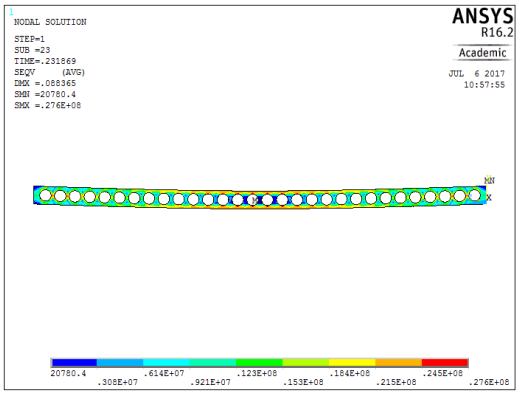


Case1

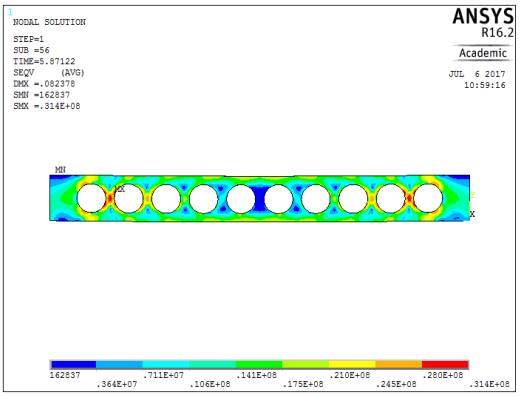


Case2

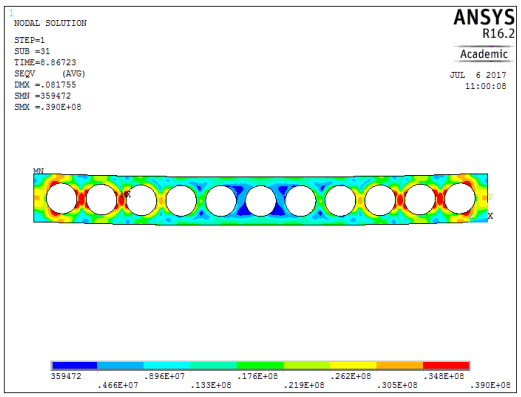


Case4

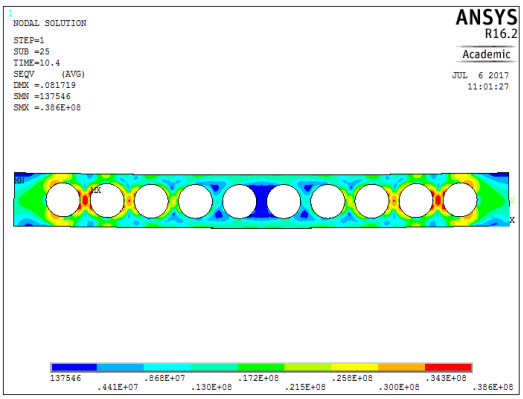


Case6

## A3. Elastic Lateral torsional buckling modes for cellular beam.

| Temp [°C] | Mode1 | Mode2 | Mode3 |
|---|---|---|---|
| Case1secion IPE220 | | | |
| T20°C | 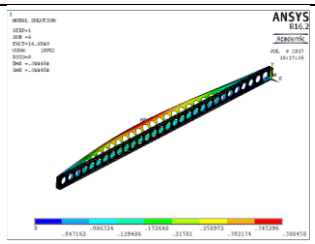 | 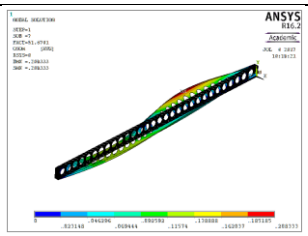 | 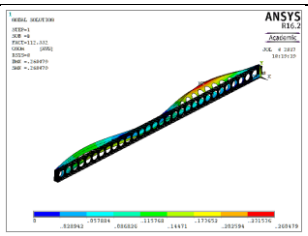 |
| T400°C | 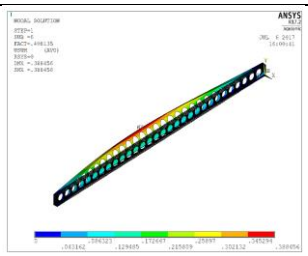 | 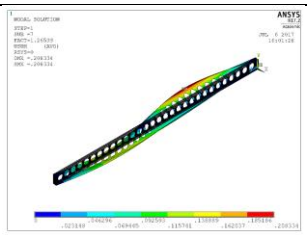 | 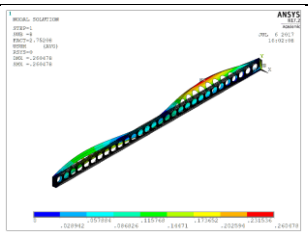 |
| T500°C | 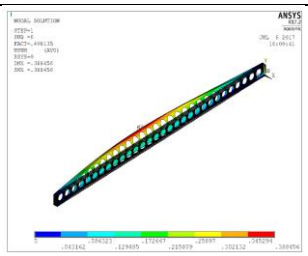 | 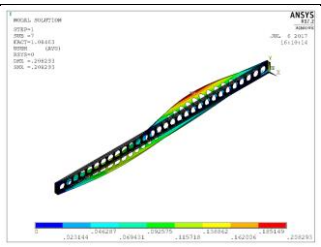 | 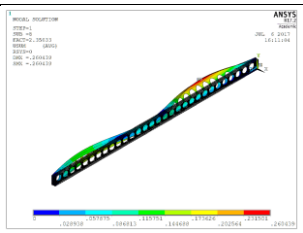 |
| Case 2 section IPE600 | | | |
| T20°C | 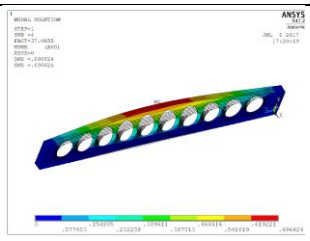 | 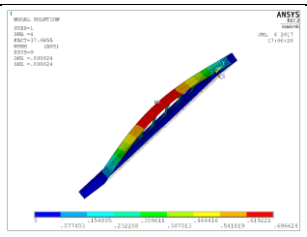 | 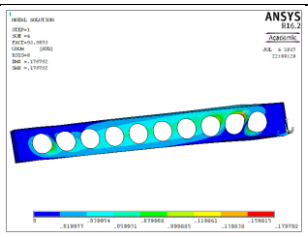 |
| T400°C | 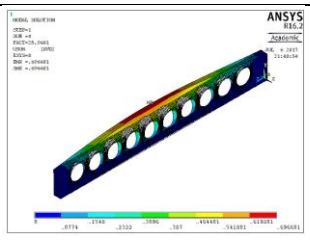 | 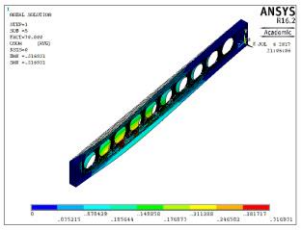 | 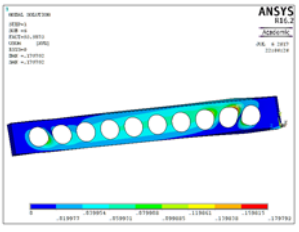 |
| T500°C | 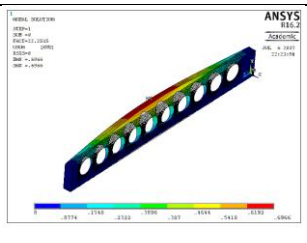 | 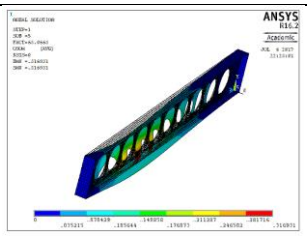 | 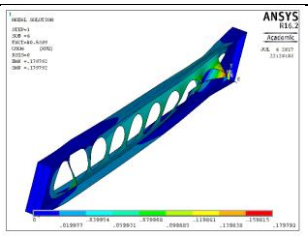 |

Case4 section HE600A

T20°C

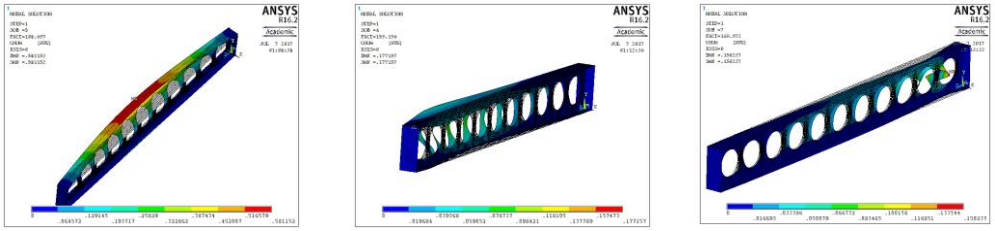

T400°C

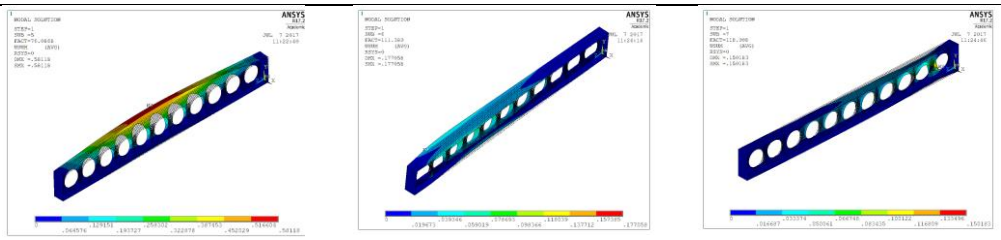

T500°C

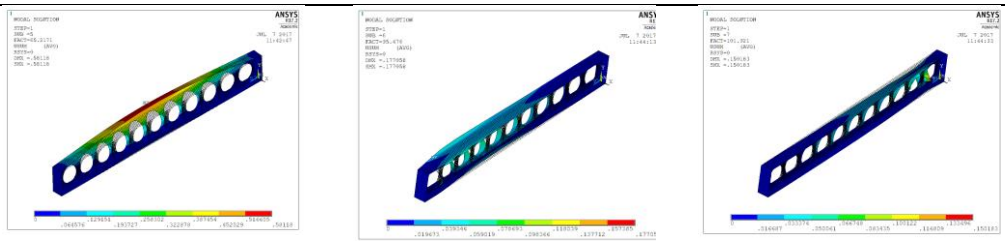

Case 6 section HE600B

T20°C

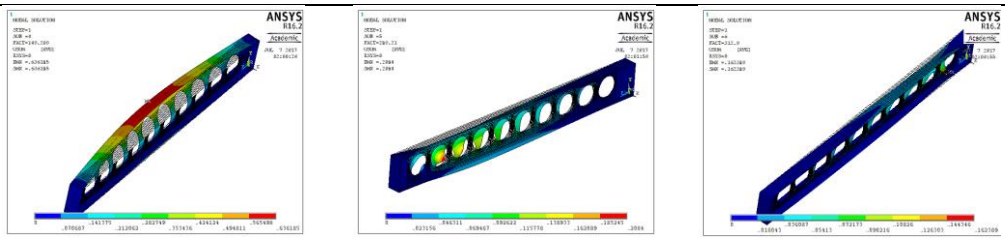

T400°C

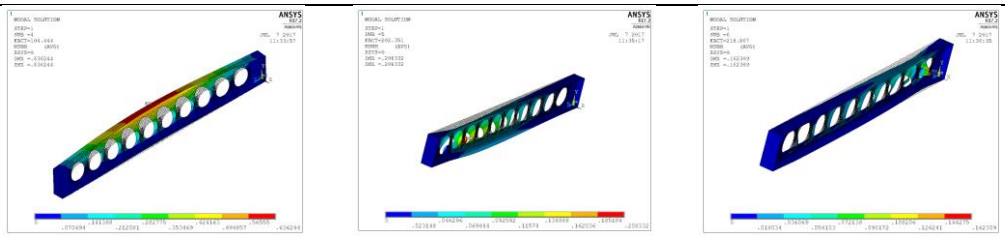

T500°C

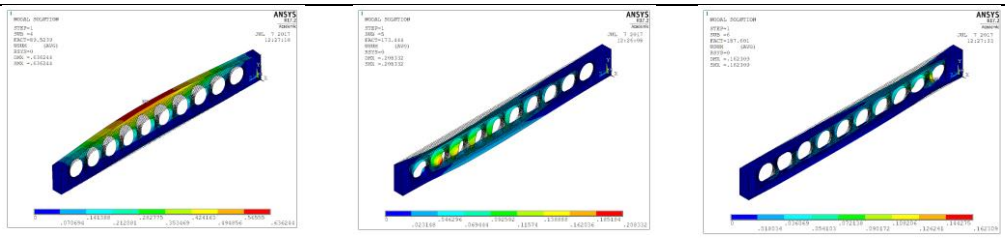

## A4. Publications

Luís Mesquitaa, Dahmane Manal, Kada Abdelhak, NUMERICAL ANALYSIS OF INSTABILITY FAILURE MODES OF CELLULAR STEEL BEAMS IN FIRE CONDITIONS, XI Conference on Steel and Composite Construction, Coimbra in November 2017. (submitted)